https://lib.uliege.be https://matheo.uliege.be

Master thesis and internship[BR]- Master's thesis : Preliminary Design and Analysis of a Deployable Space Structure for Nulling Interferometry[BR]- Integration Internship : TU Delft

Auteur : Iannello, Sacha
Promoteur(s) : Loicq, Jerôme
Faculté : Faculté des Sciences appliquées
Diplôme : Master en ingénieur civil en aérospatiale, à finalité spécialisée en "aerospace engineering"
Année académique : 2022-2023
URI/URL : http://hdl.handle.net/2268.2/18101

Avertissement à l'attention des usagers :

Tous les documents placés en accès ouvert sur le site le site MatheO sont protégés par le droit d'auteur. Conformément aux principes énoncés par la "Budapest Open Access Initiative"(BOAI, 2002), l'utilisateur du site peut lire, télécharger, copier, transmettre, imprimer, chercher ou faire un lien vers le texte intégral de ces documents, les disséquer pour les indexer, s'en servir de données pour un logiciel, ou s'en servir à toute autre fin légale (ou prévue par la réglementation relative au droit d'auteur). Toute utilisation du document à des fins commerciales est strictement interdite.

Par ailleurs, l'utilisateur s'engage à respecter les droits moraux de l'auteur, principalement le droit à l'intégrité de l'oeuvre et le droit de paternité et ce dans toute utilisation que l'utilisateur entreprend. Ainsi, à titre d'exemple, lorsqu'il reproduira un document par extrait ou dans son intégralité, l'utilisateur citera de manière complète les sources telles que mentionnées ci-dessus. Toute utilisation non explicitement autorisée ci-avant (telle que par exemple, la modification du document ou son résumé) nécessite l'autorisation préalable et expresse des auteurs ou de leurs ayants droit.

Thesis

Preliminary Design and Analysis of a Deployable Space Structure for Nulling Interferometry

Master's thesis completed in order to obtain the degree of Master of Science in Aerospace Engineering by

Sacha Iannello

Promotor:	J. Loicq
Jury members:	O. Brüls, J. Jovanova and J. Loicq
Project Duration:	Academic year 2022-2023
University:	University of Liège - School of Engineering and Computer Science

Abstract

In its quest to unravel the mysteries of the universe, this study embarks on an expedition at the forefront of celestial exploration and observational science. It focuses on the advancement of exoplanetary observation methods, and delves deep into the construction of an ingeniously designed deployable satellite. Strategically positioned within the gravitational grasp of the Lagrange point L2, this satellite harnesses the potential of nulling interferometry to provide unparalleled insights into remote exoplanetary systems. The ensuing narrative not only tackles the novel complexities associated with spatial interferometry, but also introduces inventive solutions through meticulous mechanical engineering, structural analysis and dynamic deployment studies.

The cosmos is rich with uncharted planetary bodies beyond the confines of our own solar system, beckoning us to explore their cryptic domains. In this context, this work is part of a larger effort that aims to revolutionise the field of exoplanetary observation. The deployment of the satellite within the Lagrange point L2 establishes an optimal stage for unobstructed observations, providing an advantageous platform for interferometric exploration.

At the heart of this research is the transformative technique known as nulling interferometry. Driven by the quest to unravel the intricate tapestry of cosmic signals, this technique has the potential to effectively separate the faint emissions of exoplanets from the overwhelming luminosity of their host stars. By skilfully manipulating light waves, the spatial interferometer on board the satellite will achieve the elusive ”zero” state, revealing the nuanced characteristics of exoplanetary atmospheres and surfaces. The idea of peering into these hitherto dark worlds inspires a deep sense of curiosity and wonder.

This thesis is the beginning of the complex undertaking of conceptualising a deployable satellite with unwavering precision in the face of celestial challenges. Through meticulous mechanical design, the research reveals an ingenious mechanism that orchestrates the deployment of the satellite’s interferometric instruments. A static analysis, taking into account the gravitational forces, was used to validate that the design of the selected structure was sufficiently rigid and to identify the essential dimensional requirements to minimise deformation and thereby mitigate misalignments between the telescope elements.

Research focuses on the viability of a conceptual idea in practical implementation. This involves a careful examination of the complex forces, tensions and dynamics involved in setting mechanisms in motion. This research paints a vivid picture of the physical possibilities inherent in these mechanical actions.

The study carried out in this thesis therefore results in the preliminary design of an innovative deployable structure used for space nulling interferometer. The preliminary design is presented with a 3D drawing and is accompanied by a 3D finite element model for material strength and deformation analysis, estimation of its optimum size to maximise telescope alignment, and a 3D simulation for deployment kinematics analysis.

Key words: *Deployable structure, Mechanical design, Nulling interferometry, Origami structure, Origami flasher, Static analysis, Kinematics analysis*

Acknowledgments

First of all, I would like to express my sincere thanks to my supervisors, starting with Mr Jérôme Loicq, for giving me the unique opportunity to work on such a fascinating topic in the fantastic environment of TU Delft. Your energy and passion for what you do every day has been a great inspiration to me. I would also like to thank Mr Olivier Brüls, whose wise advice and helpful tips have undoubtedly enabled me to successfully complete this research. I would also like to thank Ms Jovana Jovanova, whose creativity and boundless energy enabled me to push myself further and try to go beyond my comfort zone.

I would also like to thank my family, especially my parents and my older sister, without whom none of this would have been possible. Thank you again for the support you gave me during this period.

Thank you very much to my friends for their support, not only during this thesis, but also throughout my studies. A special thanks to Julien, my regular sports coach, for all the sports sessions and the laughs we often share. Thanks also to my friend Duncan who, despite the distance, has always encouraged me not to give up. Finally, thanks to Laura, Basil, Martin, Florian, Thomas, Sarah, Jean-Charles, Anton, Maxime, Simon, Bruno, Juliette, Emmy, Rogier, Henri, Pierre, Sandra and all the other friends who have supported me during this challenging year.

Sacha Iannello
Liège, August 2023

Contents

List of Figures

List of Tables

Nomenclature

In the following tables, all abbreviations/symbols used in this work are tabulated by order of appearance, with a definition and/or units

Abbreviations

Abbreviation	Definition
JWST	James Webb Space Telescope
HST	Hubble Space Telescope
ESA	European Space Agency
NASA	National Aeronautics and Space Administration
CSA	Canadian Space Agency
LIFE	Large Interferometer For Exoplanets
L2	Lagrange 2 orbit
CTE	Coefficient of Thermal Expansion
CME	Coefficient of Moisture Expansion
CFA	Carbon Fiber Adhesive
GAIA	Global Astrometric Interferometer for Astrophysics
IDS	Inflatable Deployable Structure
CAD	Computer Aided Design
CFRE	Carbon Fiber Reinforced Epoxy
SiC	Silicon Carbide
RB	Rigid Body

Symbols

Symbol	Definition	Unit
b	Baseline	[m]
θ	Angular resolution	[arcsec]
λ	Wavelength of the observed radiation	[m]
δ_{max}	Maximum misalignment	[arcmin]
R	Representation of the rigidity of one kind of structure	[-]
B	Representation of the baseline length reachable of one kind of structure	[-]
S	Representation of the simplicity of the set up of one kind of structure	[-]

Symbol	Definition	Unit
E	Young modulus	[GPa]
μ	Poisson's coefficient	[-]
c	Deployment coefficient	[-]
$L_{\text{tot folded}}$	Length of one side of the folded structure	[m]
l_{base}	Length of one side of the square base of the structure	[m]
e_{pan}	Thickness of a single panel	[m]
l_{tel}	Height of one telescope	[m]
L_{tot}	Length of one side of the deployed structure	[m]
l_{pan}	Length of one side of one panel	[m]
a	Acceleration constant on L2 orbit	$[\frac{\text{m}}{\text{s}^2}]$
G	Universal gravitational constant	$\left[\frac{m^3}{kg\ s^2}\right]$
M	Celestial body weight	[kg]
$D_{\text{Cel.body } - \text{ sat}}$	Distance between celestial body and the satellite on orbit	[m]
ρ	Density	$[\frac{\text{kg}}{\text{m}^3}]$
$\mathbf{V_i}$	Resulting directional vector of the arrow i	[-]
$V_{x,\ i}$	**x**-axis component of $\mathbf{V_i}$	[-]
$V_{y,\ i}$	**y**-axis component of $\mathbf{V_i}$	[-]
$V_{z,\ i}$	**z**-axis component of $\mathbf{V_i}$	[-]
δ	Misalignment angle	[rad]
σ_y	Tensile yield strength	[MPa]
σ_{VM}	Maximum Von Mises stress	[MPa]
$disp_{\text{max}}$	Maximum magnitude displacement	[mm]
h_{arm}	Height of the mechanical arm's cross-section	[mm]
w_{arm}	Width of the mechanical arm's cross-section	[mm]
e_{arm}	Thickness of the mechanical arm's cross-section	[mm]
L_1	Length of the mechanical arm's first component	[mm]
L_2	Length of the mechanical arm's second component	[mm]
L_3	Length of the mechanical arm's third component	[mm]
α_1	Angle between the mechanical arm's base and first component	[rad]
α_2	Angle between the mechanical arm's first and second component	[rad]
α_3	Angle between the mechanical arm's second and third component	[rad]
t	Deployment time	[s]
r_{engine}	Radius of the rotational engine	[mm]
$l_{\text{base, arm}}$	Length of one side of the arm base	[mm]

1

Introduction

Observing the universe is something that has fascinated mankind for as long as we can remember. The search for life other than that which we know is one of the most important topics in space exploration.

Searching life beyond Earth is not an easy task, given the immensity of the Universe. It necessarily involves observing at huge distance outside our solar system. The search for life is based on what we know: life needs water, an atmosphere and a miracle to appear [1]. Observing Earth-like exoplanets therefore makes perfect sense. However, such observations can only be made using extremely high-performance instruments. The James Webb Space Telescopes (JWST) [2] and the Hubble Space Telescope (HST) [3] are just some of the famous missions that have provided us with unprecedented images of deep space. The European Space Agency (ESA) and all the other space agencies (National Aeronautics and Space Administration (NASA), Canadian Space Agency (CSA), etc.) have set themselves the goal of finding a way to see further and further into space. This is why the Large Interferometer For Exoplanets (LIFE) mission was created. The aim of this space mission is to send a nulling interferometer into space by basing the structure supporting the various telescopes on a formation flying vehicles. Flying in formation will give a longer baseline between the telescopes, as the different vehicles will be able to move away from each other. This will result in better resolution of the observations [1].

As formation spaceflight is still a complex solution to implement, ESA has requested a proposal for a unique vehicule that would allow this nulling interferometry technology to be used [4][5].

The aim of this thesis is to provide a preliminary design for a potentially deployable space structure that maximises the baseline and hence the resolution of the images observed by nulling interferometry, while maintaining the most accurate alignment possible of the various telescopes considered on this structure.

Several stages will therefore be carried out in this research, starting with a literature review of the different types of deployable structure that can be considered, presented in chapter 3. The second stage consists of creating a design from a blank page that can respond to the problematic; this is done in the chapter 4.

Next, an initial static analysis will be carried out on a simplified model of the design in order to check that the proposed design is enough rigid and to define the main dimensions of the structure, and thus obtain the length of the maximum baseline achievable with this design. A second static analysis, this time on a more complete model, will follow to obtain an estimation of the alignment of the telescopes with the selected design once exposed to the gravitational acceleration of its orbit. These two static analysis will be carried out using **COMSOL Multiphysics** software and their results will be presented in chapter 5.

In Chapter 6, a simple kinematic analysis will be presented to check that the deployment is safe and collision-free.

Finally, as this research is about a preliminary design proposal for the structure, a list of future studies and further details to be explored will be provided in chapter 7 with a view to a possible follow-up to this work.

2

Context and Project Description

2.1. Space missions

For a considerable length of time, the concept of space remained elusive to scientists who could only observe the movements of celestial bodies from the Earth's surface.

However, technological advances have enabled the launch of numerous space missions aimed at expanding the understanding of the universe beyond Earth's boundaries. The scientific community endeavors to send satellites deeper into space, as doing so allows to travel further back in time. Recent breakthroughs have greatly facilitated their pursuit of knowledge in this field.

One of the primary objectives of space research is to determine the possibility of extraterrestrial life beyond Earth. The scientific community has been actively pursuing the discovery of planets that possess the necessary conditions for life as it is known. Various techniques, such as transit observation, gravitational microlensing, etc., have been employed to identify these terrestrial exoplanets or simply exoplanets. Most of these detection methods are indirect, relying on the observation of changes in the behaviour of stars due to the presence of exoplanets passing in front of them.

However, recent research aims to introduce an alternative exoplanet detection method based on direct observation known as nulling interferometry. The Large Interferometer For Exoplanets, also called LIFE mission, is an example of a future space mission designed to use this technique. The LIFE mission is intended to characterise the atmospheres of terrestrial exoplanets and search for signs of life outside our solar system by utilising structures that fly in formation [1].

Nevertheless, using flying formation structures presents significant risks, and thus it is still in its early stages of development. Indeed, a flying formation of telescopes is a very complex system to set up. The remote control of the almost perfect alignment of the rays (at the nm-range) is difficult to achieve for a system made up of several completely separate structures. As a result, the concept of sending a first structure in one single piece using nulling interferometry has been proposed as a starting point [6]. It is in this context that this work is presented.

2.2. Nulling interferometry

Nulling interferometry is a method that can be employed to detect exoplanets. The fundamental principles of the method are briefly outlined in this section.

2.2.1. Fundamental principles

Using a single telescope structure to observe exoplanets and more precisely terrestrial exoplanet, that are the ones that could potentially contain life, is really difficult. Undoubtedly, measuring the infrared spectrum of rocky exoplanets poses immense challenges due to the tight separation and high contrast between these planets and their host stars. For instance, at 10 μm, the Sun outshines Earth by a factor of 107, yet their angular distance at 10 parsecs is only 0.1 arcsec [6]. Given the atmospheric thermal background, observing terrestrial exoplanets necessitates space-based telescopes. Unless launching giant primary mirrors (>30m diameter) into space becomes feasible, overcoming this observational hurdle mandates the use of interferometric techniques. By combining light from distant telescopes, interferometry enables direct observations within the diffraction limit of individual single-dish telescopes, thus addressing this challenge effectively [6].

In Fig. 2.1b, the basic principles of a two-aperture nulling interferometer are depicted. In this setup, light emanating from a distant star is captured by two separated apertures/telescopes, positioned at a certain distance b from each other, known as the baseline. Delay lines can be added to one of the telescope beams to ensure that the light traverses the exact same distance. By introducing a π-shift, i.e. a delay imposed in the light wave by one half of the wavelength, in one of the beams, destructive interference of the incoming light can be achieved. By partially cancelling out the light emanating from the star, which is located precisely on the optical axis, it becomes possible to observe the light originating from potential exoplanets orbiting around this star.

For a slightly off-axis source, such as an exoplanet orbiting around a host star, the additional phase due to its differential external path will be slightly longer. This results in a phase difference from this source, allowing its light to be transmitted instead of destructed. In Fig. 2.1a, a transmission map is depicted, which shows the sources that are observable (light fringes) and those that are not (dark fringes).

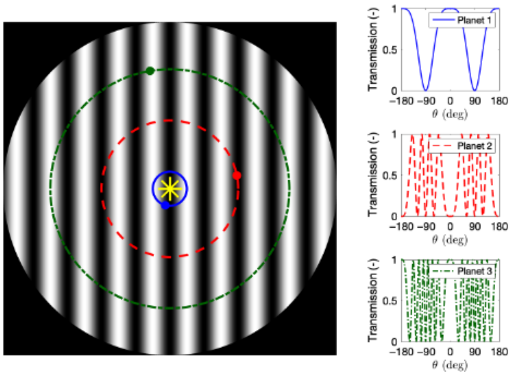

(a) Transmission map for 3 exoplanets separated by different distances from the same star. Planet 1 is located closer to the star than planets 2 and 3. And planet 3 is furthest away from the star [7].

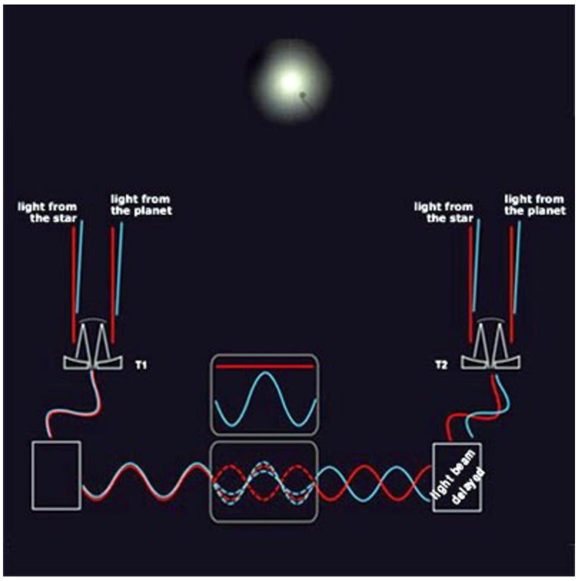

(b) Basic principles of nulling interferometry. T1 and T2 represent two separated telescopes which capt the light from the same target and transmit it to a combiner. [8].

In some cases, the desired source may still be located on a dark fringe, rendering it undetectable using the traditional nulling interferometry method. To address this issue, Bracewell [7] proposed a solution in 1978 that involves rotating the interferometer to ensure the exoplanet can always be detected, even if it is located on a dark fringe. Fig. 2.2 illustrates this technique. By rotating the interferometer, the dark fringe moves across the aperture, allowing the exoplanet to be detected at different points in time.

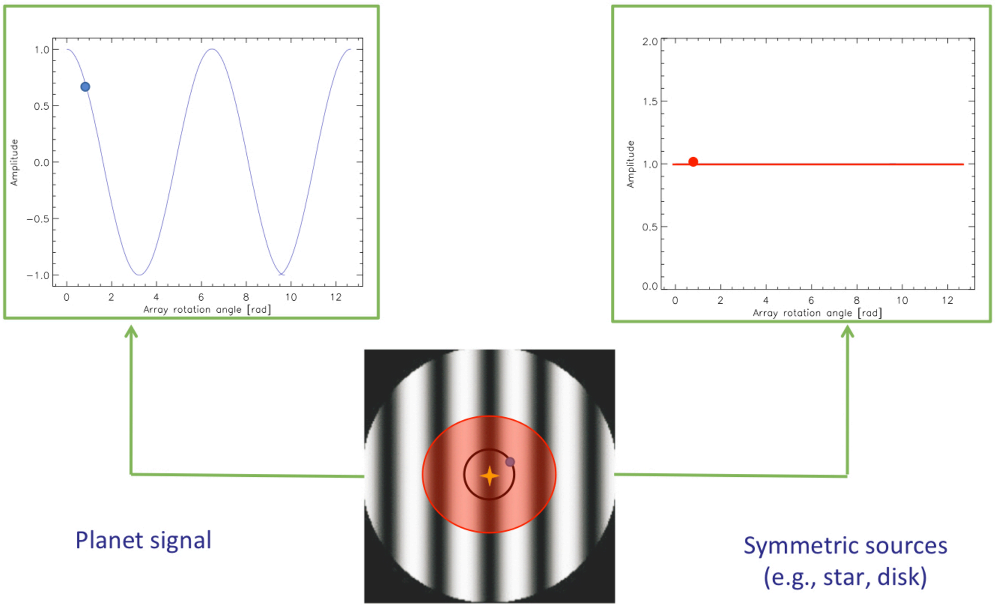

Figure 2.2: A transmission map shows with dark and light fringes representing the non-observable sources and the observable ones respectively. The centre of the transmission map represents the target of the nulling interferometer. The symmetric sources that have to be cancelled, such as a star, are located at this centre and provide thus an almost constant amplitude signal. The planet signal appears to vary with time since it is located off-axis [9].

2.2.2. Important parameters for nulling interferometry

The nulling interferometry was introduced earlier to provide a clear understanding of the main parameters that need to be considered when designing a structure in order to obtain a perfect alignment for detecting exoplanets.

The primary goal of nulling interferometry is to align an observed star precisely with the line of sight in order to null the amount of light coming from the star. To understand the mechanics, the key is to exploit the wave nature of light. The telescopes receive light waves from the target star, and by deliberately creating a controlled difference in the path each light wave follows, i.e. the Optical Path Difference (OPD), these waves are made to collide in the interferometer. This collision triggers a process known as interference, where the waves either amplify or cancel each other out, depending on their phase relationship. Moreover, the Optical Delay Line (ODL) is a critical component in this setup. It introduces a precisely controlled delay into one of the light waves, effectively synchronising their arrival times at the interferometer. This step ensures that the waves are in phase, making it easier for them to interact. At this point, one of the light waves is π-phase shifted. This means that its phase is π-shifted, essentially putting it in phase opposition to the other wave. When these π-phase shifted waves merge, their amplitudes combine to produce destructive interference, that leads to a cancellation effect. Starlight, being a coherent source, is inherently in phase with itself.

By introducing this π-phase shift, the phase of the starlight is altered so that when it converges with the other light wave, they interfere destructively. This orchestrated interference targets the starlight, effectively suppressing its intensity in the resulting combined beam. The precise alignment of the telescopes provides the opportunity to detect exoplanets whose emitted light is greater than the residual light from the star [7]. It is important for the structure to be stable and stiff enough to maintain alignment between the different telescopes even in the noisy space environment. Therefore, the first important parameter to consider is the resistance to space environment application on the structure once it is deployed in space.

The second parameter to consider is the size of the baseline. The baseline of an interferometer is a crucial factor that directly influences its resolution. The baseline refers to the separation distance between the two telescopes in an interferometric array. The resolution of an interferometer, often referred to as its angular resolution, is the ability of the instrument to distinguish between two closely separated objects in space. In other words, it determines how finely the interferometer can discern details or features in a celestial object. The link between the baseline and resolution stems from the fundamental principles of interference and wave propagation. When an interferometer combines the light waves collected by its telescopes, the waves interfere with each other. The constructive and destructive interference patterns that result are influenced by the phase difference between the waves when they combine. For an interferometer, a longer baseline translates to a greater OPD between the waves received by the telescopes. This OPD causes the waves to have a different phase when they meet at the point of interference. When the waves combine, the resulting interference pattern becomes more sensitive to smaller differences in phase, which in turn enables the interferometer to discern finer details in the observed object. Mathematically, the angular resolution θ of an interferometer is inversely proportional to the baseline b:

$$\theta = \frac{\lambda}{2b}, \tag{2.1}$$

where:

- θ is the angular resolution [arcsec],
- λ is the wavelength of the observed radiation (mainly mid-infrared here (3 - 20 μm) [6]) [m],
- b is the baseline separation between the telescopes [m] [10].

As the baseline increases, the denominator in the equation becomes larger, resulting in a smaller angular resolution for a same wavelength of the observed radiation. This means that the interferometer can resolve finer details and distinguish between objects that are closer together in space. Therefore, the size of the baseline must be maximised.

Finally, the telescopes' configuration needs also to be considered. Presently, research is underway to determine the best configuration for telescopes. In the initial stage of this research, only four configurations will be considered out of an infinite number of options. Eventually, only one configuration will be selected for simplicity. The four configurations are the following ones:

(a) Diamond configuration.

(b) Rectangle configuration.

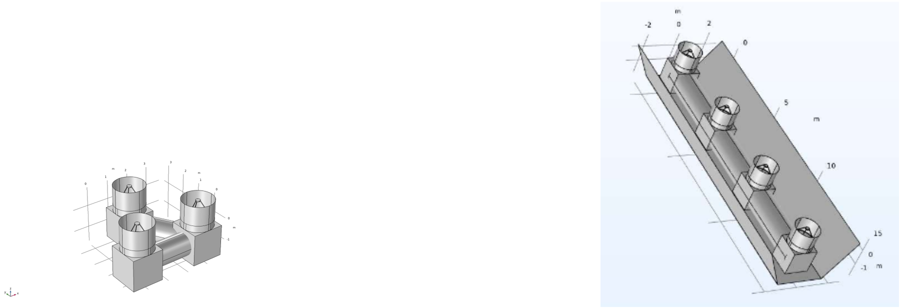

(c) Triangle configuration.

(d) Linear configuration.

Figure 2.3: All the configurations of the telescopes proposed in the beginning of this study [6].

It is important to note that for now, none of these configurations showed more promising results in terms of resolution than the other ones. So all of them can be seriously considered.

2.3. Research objectives of the thesis

As mentioned before, formation flying space mission, as proposed by the LIFE mission, is too complex to be implemented at the moment. Therefore, a single structure must be investigated to test a large space nulling interferometer. However, certain geometric constraints must be considered since this structure must fit within the fairing of the European expendable launch system Ariane 6, which has roughly dimensions of 5 meters wide and 15 meters high [11].

To maximise the baseline and thus the structure's size in space, a deployable structure design should be used due to geometrical dimensions launch constraint. Various techniques can be employed to achieve this, which will be explained in detail later.

The stability of the structure once in space must be very high even without compensators that could help later on. Indeed here, it is a question of collecting the light from stars millions of kilometres away: a lack of stability, no matter how slight, would lead to what is known as telescopes misalignment, resulting in the different telescopes no longer pointing in the exact same direction. The results would be totally disrupted and would therefore be less inaccurate. The more stable the structure, the less misalignment between the satellites and the more accurate the results. The research objective thus comes directly:

Determine the ideal configuration for a deployable space nulling interferometer that maximises its size without compromising its stability.

This research objective can be divided in research questions that will be answered later in this report.

2.3.1. Requirements

The requirements for this thesis are the following ones:

- **Deployable system**: Although a rigid non-deployable system with a baseline at the height of the Ariane 6 fairing, i.e. 15 m, is a solution that must be considered in the context of this mission, this research will be based on a deployable structure with the aim of achieving a baseline greater than that proposed by a non-deployable structure, while complying with the requirement for misalignment. Finally, this deployable system will have to be compatible with one of the four telescopes configurations presented at Fig. 2.3.
- **Minimise misalignment**: The deformations of the structure once deployed have to lead to a maximum misalignment $\delta_{\max}$ between the telescopes pointing axis of **0.5 arcmin** or equivalently **30 arcsec**. This preliminary design will be made with this requirement as a minimum target to be achieved. In any case, a list of the parameters to optimise in order to decrease that value if the target evolves in a second stage of design will be detailed.
- **Maximise resolution**: Eq. 2.1 shows that the larger the baseline, the greater the resolution for the same wavelength range. The baseline should thus be as large as possible to improve the resolution. There is no minimum size required at this stage of the design. However, the reason to design a deployable structure is of course to get an advantage in terms of resolution. If it is considered that the maximum baseline with a non deployable is limited because of the dimension of the fairing of the launch vehicle, i.e. Ariane 6, to say 15m, then the baseline will need to be larger than **15 m**.

It is very important to understand that all these three requirements are related. There will be some optimisation to be made in order to achieve the final design. For example, the maximum length for the baseline will be also associated with a higher misalignment or with oversized structure and extra weight.

In this thesis, the only focus will be on the geometric design of the deployable structure and a validation that it makes, based on a first estimation of the dimensions, the stability of the structure and the collision free deployment will be done.

If this study evolves into a second phase, detailed requirements would have to be defined and optimised.

2.3.2. Research questions

The principal research questions that can resume this thesis is simply the following one:

What could be a deployable space nulling interferometer design that meets the requirements, i.e. $b \geq 15$ m and $\delta_{\max} \leq 30$ arcsec?

The first step of this research is thus to determine which design is best suited to this mission. This main question leads to sub-questions such as:

- What kind of deployable structure is suitable for space application and respects the physical constraints imposed by the Ariane 6 fairing geometry?

- How to optimise the size of the baseline of the deployed structure taking into account all the requirements?
- Is it possible with a deployable structure, and thus a larger baseline than for a non-deployable structure, to achieve the minimum misalignment target?
- What are the values of misalignment that the structure can reach once deployed and submitted to a static load corresponding to the acceleration that the structure will feel once on orbit (Lagrange L2)?
- How can the rigidity of the whole structure be optimised in order to reduce the misalignment as much as possible while keeping a large baseline?

This research aims to answer all these questions.

3

Literature Review

In this chapter, a theoretical approach will be made in order to introduce the deployable technologies that could be used for this research.

Section 3.1 will present the most common types of deployable mechanisms that have to be considered with the aim of selecting a design that best meets the requirements. A multi-criteria evaluation will conclude this section. Section 3.2 will describe the different steps of a stability analysis. A brief introduction of the different software used during this research will also appear at the end of this section.

3.1. Different types of structures

3.1.1. Smart components

In mechanical engineering, a smart component or smart structure is a system that is able to sense and adapt itself to its environment, process the acquired data, and respond by adapting its mechanical characteristics to changing conditions. This is achieved by embedding sensors, actuators, and control systems within the material of the structure. Sensors are essential components that collect data from the environment and provide input for decision-making processes within a smart structure. For instance, strain gauges are widely used sensors that measure deformation in materials [12]. Actuators are mechanisms responsible for executing actions in response to input from sensors or control systems. Shape-memory alloys are a class of actuators that change shape upon the application of heat or current [13]. Finally, control systems manage the decision-making and operational aspects of a smart structure. They interpret sensor data and activate actuators accordingly. A proportional-integral-derivative controller is a commonly used control system [14].

Smart components have a wide range of applications as they offer improved performance, durability, and safety to traditional structures [15]. Smart components are not structures in the strict sense of the term, but rather complements used by structures to improve their performance. In space engineering, all structures are equipped with smart components, whether to improve stability, maintain an acceptable temperature, or whatever.

Smart characteristics

A smart structure in mechanical engineering typically has the following characteristics [16]:

- **Ability to sense changes in the environment**: Smart structures are designed to sense changes in their surrounding environment such as temperature, pressure, and stress [17].

- **Ability to respond to changes**: Smart structures can respond to changes in the environment by changing their shape, stiffness, or damping characteristics [18].
- **Self-monitoring and self-diagnosis**: Smart structures have built-in sensors and diagnostic systems that can detect any defects or damages in the structure and take corrective actions [19].
- **Self-repairing**: Some smart structures have the ability to repair themselves in case of damage, which can increase their longevity and reliability [19].
- **Lightweight and compact design**: Smart structures are often designed to be lightweight and compact, making them ideal for use in applications where space and weight are limited, such as in aerospace and automotive industries [19].

State of the art

- **Vibration control systems for aerospace structures**: The system uses embedded sensors and actuators to detect and actively dampen vibrations that can lead to fatigue and failure in the structure over time. The smart structure is able to sense the vibrations and then activate the actuators to produce an equal and opposite force to dampen the vibration, thereby reducing the likelihood of failure. This gives the information that smart structures are not sufficient by themselves. They need to be used with deployable techniques, such as reconfigurable structure [20].
- **Design of aircraft wings**: Smart materials, such as shape memory alloys and piezoelectric materials, are used. They can be embedded in the structure of the wing to enable it to change shape in response to different flight conditions. This can help to improve aerodynamic performance and reduce drag, leading to greater fuel efficiency and longer range for the aircraft. The embedded sensors in the smart structure can also provide real-time data on the wing's condition, allowing for proactive maintenance and avoiding potential failures [21].
- **Aircraft wings monitoring**: Smart structures can be used in the aerospace domain to monitor their condition in real-time, detecting any damage or changes in structural integrity. This can be achieved by embedding sensors and actuators in the wing structure, which can measure parameters such as strain, temperature, and vibration. The data collected by these sensors can then be analysed to identify any potential issues, allowing for early detection and prevention of damage. This can improve safety, reduce maintenance costs, and extend the lifespan of the aircraft [22].

3.1.2. Ultra-stable structures

An ultra-stable structure in the aerospace domain is a structure that has an extremely high level of stiffness and stability. Such structures are designed to maintain their shape and dimensions with minimal deformation, even when subjected to extreme environmental conditions, such as temperature variations, vibration, or mechanical stresses. For interferometry, the system's ultra-stability is essential. For this reason, the systems studied in this thesis will necessarily be combined with ultra-stability characteristics [23].

Achieving ultra-stability depends on a carefully orchestrated interplay of factors involving complex design considerations, meticulous material selection, sophisticated manufacturing methods and rigorous quality control protocols. At a more granular level, the foundation of this achievement lies in the deliberate design of components to minimise susceptibility to environmental and mechanical stresses. Careful material selection further enhances this stability, with a focus on materials characterised by minimal thermal expansion, excellent mechanical strength and intrinsic resistance to vibration interference. Advanced manufacturing techniques, often involving precision machining or additive manufacturing processes, facilitate the realisation of intricate geometries that maintain the desired stability. These techniques, coupled with quality control processes that rigorously assess and validate every stage of production, ensure that any deviations or imperfections are meticulously identified and rectified. The result of these many measures is a system or structure that is a model of consistency, unaffected by external forces and primed to deliver consistent, reliable performance in a variety of demanding environments. [24]

Ultra-stable structures are used in a variety of aerospace applications, including satellites, space telescopes, and interplanetary probes. They are also used in ground-based applications, such as astronomical observatories, where the high stability is necessary to ensure the accuracy of measurements. In the context of this thesis, a deployable system is considered. Conventionally, ultra-stable systems are made in one piece in order to reduce any potential points of weakness that may reduce overall stability. The problem lies in the fact that a deployable system has many kinematic joints which drastically reduce the stability of the system. The aim will therefore be to use the qualities of ultra-stability, for example by taking the materials generally used for ultra-stable structures, and apply them to a deployable system [25].

Ultra-stable characteristics

The main characteristics of ultra-stable structures in the aerospace domain are their high level of stability, precision of the observation, and reliability. These structures are designed to maintain their shape and position in space over long periods of time, despite exposure to extreme temperatures, radiation, and other environmental factors. They are also designed to withstand mechanical stresses and vibrations that could affect their performance [24].

Ultra-stable structures often use advanced materials and design techniques, such as composite materials, active damping systems, and precision alignment mechanisms. They are typically designed to be lightweight. A material that is often used for such a structure is the carbon/carbon composite whose density is around 1800 $\frac{\text{kg}}{\text{m}^3}$ which means that it is pretty light material [26]. These structures are also designed to stay strong enough to resist deformation and maintain their shape and position. The Young modulus of the carbon/carbon composite is about 230 GPa which means that this ultra-stable material is rather resistant against external loads for instance [26]. Ultra-stable structures may be used in a variety of aerospace applications, such as satellite structures, space telescopes, and interplanetary spacecraft [25]. The Nancy Grace Roman Space Telescope NGRST is a NASA satellite currently under development and scheduled for launch in 2027. The primary goal of this space telescope is to study dark energy and observe exoplanets. To observe exoplanets, it will use the coronagraphic method, which involves placing a 'pellet' in front of the light coming from the star so that only the light from the planets orbiting it passes through [27]. The stability of such a system is crucial for obtaining good observations. It is therefore stabilised on 3 axes and uses reaction wheels to control its orientation, which must be accurate within 3 arc seconds [28]. The model of the Roman Space Telescope depicted in May 2020 is shown on Fig. 3.1.

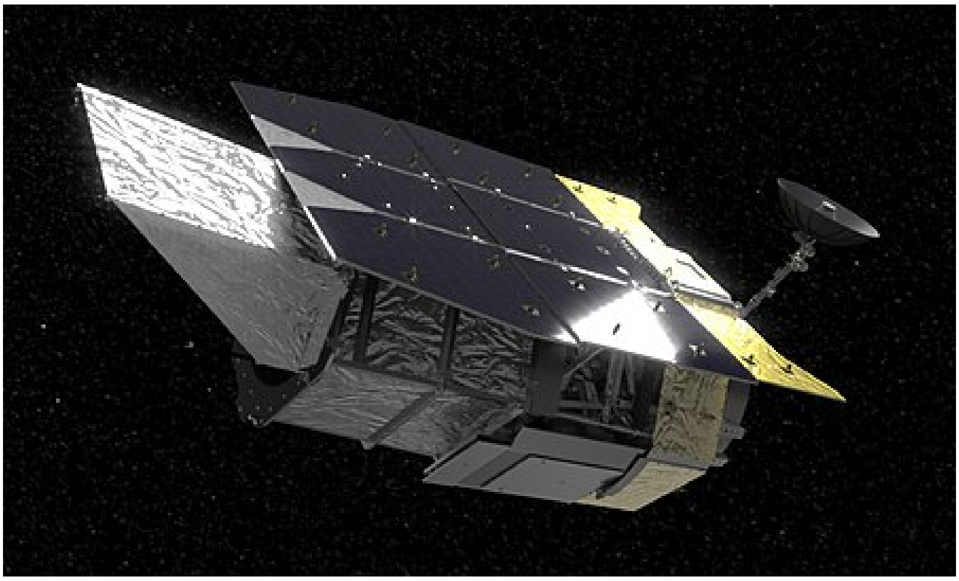

Figure 3.1: Model of the Roman Space Telescope depicted in May 2020 [28].

State of the art

A lot of existing ultra-stable structures are already existing in the aerospace's domain. Here is a small list of some of these existing ultra-stable structures.

- **Large ultra-stable telescope system**: The requirements for the optical stability have to be extremely strict since such a structure must be stable at an extremely high level of stability. As an example, the JWST is once again used to be compared to an ultra-stable structure. JWST is a passive stable structure which means that it maintains its own stability without requiring any external control or feedback mechanisms. Such structures are designed to have a natural resistance to disturbances or changes in the environment. In contrast, an active ultra-stable structure relies on active control systems that uses feedback from sensors to continuously adjust and maintain the stability of the structure. This typically involves using actuators to make precise adjustments in response to changing conditions, such as temperature, pressure, or vibration. While passive stable structures are simpler and more robust, active ultra-stable structures can achieve higher levels of stability (picometer level stability for ultra-stable structures and nanometer for passive stable structures) and precision, making them well-suited for applications where extreme stability is required, such as in space telescopes or other scientific instruments [29].
- **Carbon/carbon composites for ultra stable structures**: A structure requires specific material characteristics, such as a low thermal expansion coefficient (CTE), a low moisture expansion coefficient (CME), and excellent mechanical strength, to achieve the desired stiffness. Thermal expansion is the increase in size of a material due to temperature changes, and a low CTE is necessary to minimise the deformation of the structure under temperature variations. CME refers to the increase in size of a material due to the absorption of moisture, and a low CME is necessary to minimise the deformation of the structure due to moisture changes in the environment. Good mechanical strength is necessary to ensure that the structure can withstand loads and maintain its shape under external forces. Therefore, a structure with these specific characteristics is essential for maintaining stability and avoiding deformation, which can compromise the performance

and functionality of the structure. Promising material that can be used for ultra-stable structures: carbon/carbon composites. Indeed, carbon/carbon composites have a very high thermo-elastic stability, which results in an almost zero CTE. This material also has a low density and good mechanical properties, making it a good candidate. Finally, its CME is zero [25].

The production of enormous carbon/carbon composite panels is not currently feasible in the manufacturing process because it is possible to produce panels up to 2.5 m^2 only. Thus, a structure larger than 15 m can not be produced in on single piece. Therefore, it is necessary to produce multiple panels and connect them with joints. Specific joining materials are required for this purpose. The most suitable joining material is carbon fiber adhesive (CFA) with CTE filters to reduce the CTE value [25].

- **Ultra-stable polymer composites reinforced with carbon fibres**: The GAIA mission is described here. The structure of this mission is based on an umbrella principle where everything is deployed once launched as shown on Fig. 3.2. The toroidal structure of the optical bench, essential for achieving the scientific objectives of the Gaia mission, is made of silicon carbide material due to its desirable optical, mechanical, and thermal properties. Specifically, to ensure a thermally stable mounting platform, which is critical for the mission, silicon carbide is used because it has a negligible coefficient of thermal expansion, which means it does not experience significant expansion or contraction as the temperature changes [30].

Figure 3.2: Deployment of GAIA [30].

3.1.3. Origami structures

Origami are a very old creation coming from Japan to develop artistic structures. The word *Origami* comes from the Japanese words *oru*, meaning *to fold*, and *kami*, meaning *paper* [31].

The practical application of origami engineering spans a range of scales, from examples such as a large-scale architectural front that can reshape itself to control shading [32], to the manipulation of DNA to construct nanoscale mechanisms [33]. Moreover, some existing space missions have components inspired by origami, such as the GAIA mission, whose deployment sequence is shown in Fig. 3.3.

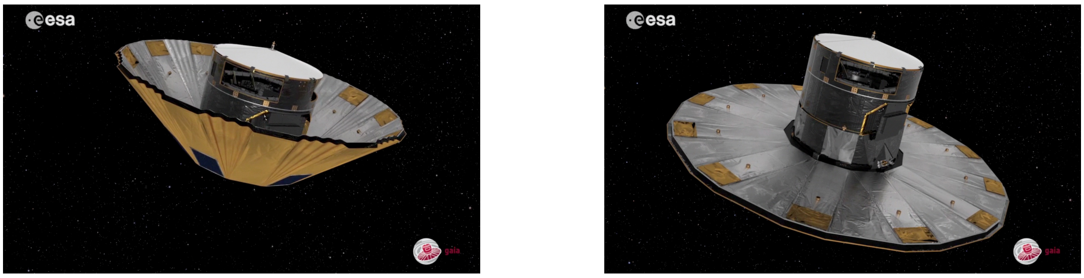

Figure 3.3: Left side shows GAIA's sunshield during its deployment, right side shows GAIA's sunshield fully deployed [34].

Origami characteristics

The main advantage of an origami structure is definitively its ability to deploy itself from a compact state to a large deployed structure, becoming a large deployed structure. Its compactness is thus a very good point regarding the requirements for this mission. Some spatial missions already use origami in some parts of their structure such as for example GAIA shown at Fig. 3.3 and the solar shield of the famous James Webb Space Telescope - JWST [35]. Fig. 3.4 shows this sunshield that has been folded following an origami pattern to fit into the spacecraft that took it into space.

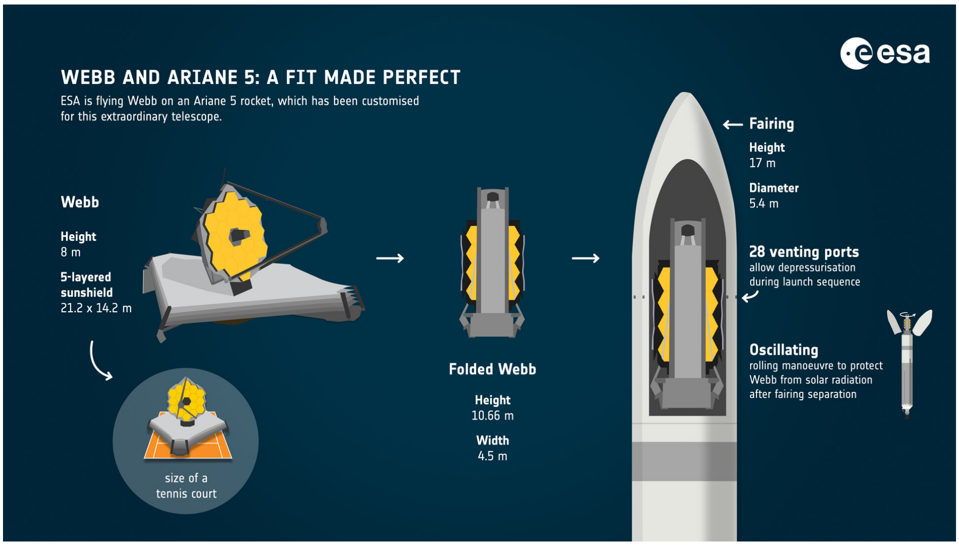

Figure 3.4: JWST sunshield folded to fit perfectly into Ariane 5 [36].

To increase the stability of origami structures as much as possible, the easiest way to proceed is to use thick panels. The main disadvantage is therefore the weight of such a structure. But there are solutions to counteract this disadvantage such as using hollow panels or adding compensators to thinner panels [37].

State of the art

As said previously, many applications of origami for deployable structure exist. Here is a short listing of some of these applications and what they can provide in terms of information.

- **JWST**: The sunshield of the JWST is an enormous solar protection the size of a tennis court that is deployed using an origami basis. This solar shield deployment does not give information about the stability of origami structures since it is not designed to reach a good stability. However, the proof that it can be used to obtain the largest structure possible is there [35].
- **Triangulated Cylinder Patterns**: Two different patterns for triangulated cylinder are shown in Fig. 3.5 to highlight the importance of panel's dimensions. Indeed, depending on the angles and dimensions of each panel, the triangulated cylinder can be either very rigid and stable but undeployable or very compact and deployable but without any rigidity when completely deployed [38].

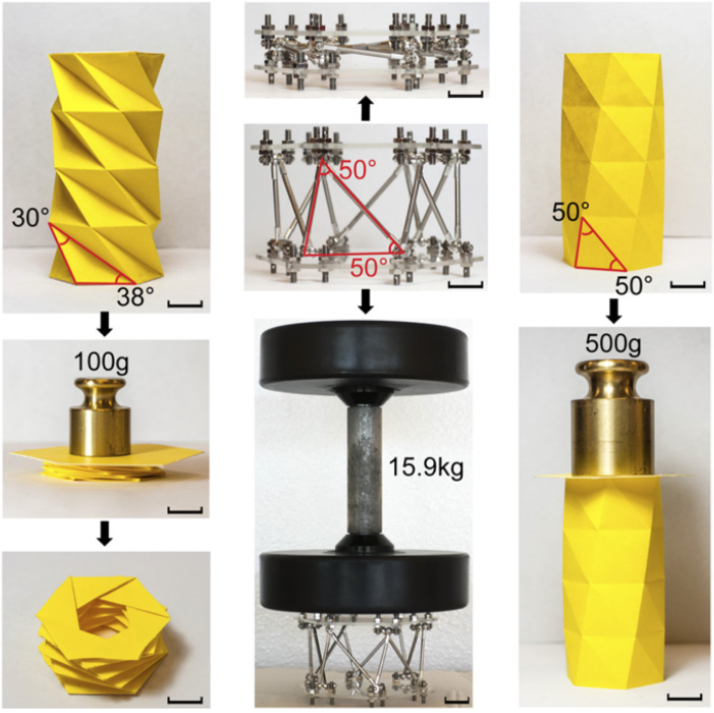

Figure 3.5: On the left side, the triangulated cylinder pattern is composed of triangles having small angles at the base. This pattern leads to a very deployable structure but absolutely not resistant when submitted to external forces. On the right side, the triangles composing the triangulated cylinder pattern have larger angles which leads to a very resistant and stable structure but unable to be undeployed [38].

- **Origami Flasher**: This is a certain kind of origami pattern called *Origami Flasher*. These pattern are composed of a polygonal basis (it could be square as it could be octagon) which is surrounded by spiral-inspired origami arms as shown on Fig. 3.6. Additionally, one application of this origami flasher is linked to NASA, which has called on origami experts and engineers to design a solar array based on origami [39]. This structure allows a very large surface when deployed which can lead to several possibilities of telescopes configurations as explained in section 2.2.2 [40].

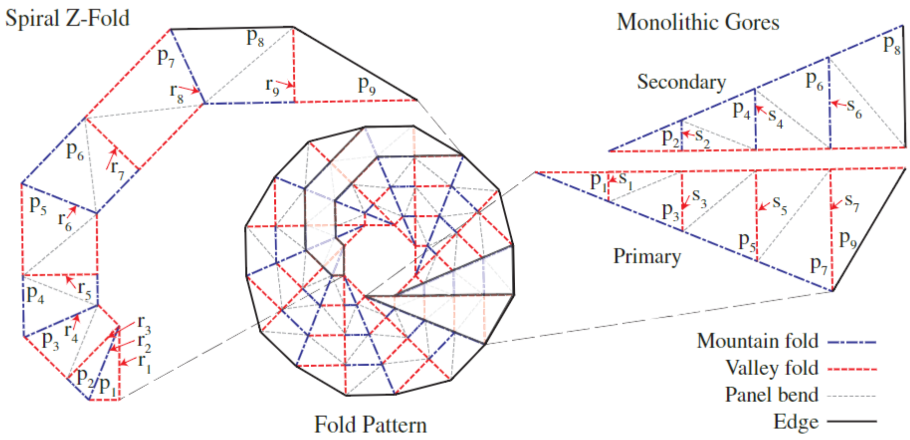

Figure 3.6: Octagonal origami flasher pattern. Left side represents the spiral-inspired arms, right side represents another division of the whole structure. The difference in colour of each of the lines on this scheme represents a folding direction (red line for valley fold, blue line for mount fold) [40].

- **Yoshimura origami**: It is one of the most famous and simple origami known. Two different thicknesses of panels are tested (Fig. 3.7) to determine the importance of this parameter.

Figure 3.7: Left side shows the model with thin panels, right side shows the one with thick panels [37].

Thicker panels give way better stiffness. Indeed, even if origami is basically designed for very thin panels (paper originally), once submitted to load bearing or once completely deployed an origami-inspired structure with thin panels becomes ductile [37].

- **Compliant mechanism for Origami-inspired structure**: An origami-inspired structure using compliant mechanisms as revolute joints allows to *lock* the structure in certain positions. In this case there are two different positions: completely folded or completely deployed Fig. 3.8 [41].

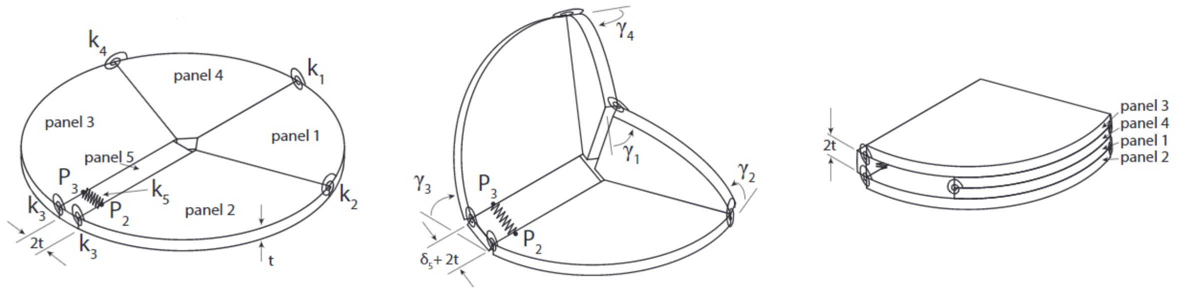

Figure 3.8: From left to right, these figures show the folding of this structure. Between panel 1 and panel 3, there is a compliant mechanism acting like a spring [41].

3.1.4. Reconfigurable structures

A reconfigurable structure in mechanical engineering refers to a structure that is designed to change its shape or configuration according to specific requirements [42]. For example, the potential of microelectronic devices lies in their reconfigurable three-dimensional microarchitecture, allowing repeated transitions between various geometrical and operational states. While these structures hold promise across multiple domains, conventional methods primarily depend on using external electric or magnetic fields to induce material deformations, which could bring unwanted side effects and reduce overall device performances [43].

Thus, reconfigurable structures can be adjusted or modified in some ways to suit different needs, such as changes in load conditions, environmental factors like electromagnetic field, or operational requirements. In essence, a reconfigurable structure offers flexibility and adaptability, which can be useful in various applications where changing conditions or requirements need to be addressed [44].

Reconfigurable characteristics

The main advantages of reconfigurable structures are their compactness capability and their very light weight. Indeed, impressive differences of size between deployed and undeployed configuration of a reconfigurable structure can be observed. Due to the need of less material, the weight is directly reduced compared to other types of deployable structures. The main disadvantage appears when the stability is analysed since such a structure is not known for its good stability. Indeed, without a *lock* system allowing every joint to stop moving at a certain position, the stability is not present at all and external load could move the entire structure easily in most cases. It is therefore necessary to use lockers, or smart mechanisms to obtain a deployed position that is stable enough in the case of this research (30 arcsec of misalignment of the telescopes maximum) [45].

State of the art

A short listing of some applications where reconfigurable structures are used and what they can give as information is provided here.

- **Self-lockable deployable structure**: There is only a single locked position for this structure obtained by playing on the joint nodes and the relative positions of the other members. Examples of this application are shown in Fig. 3.9 [45].

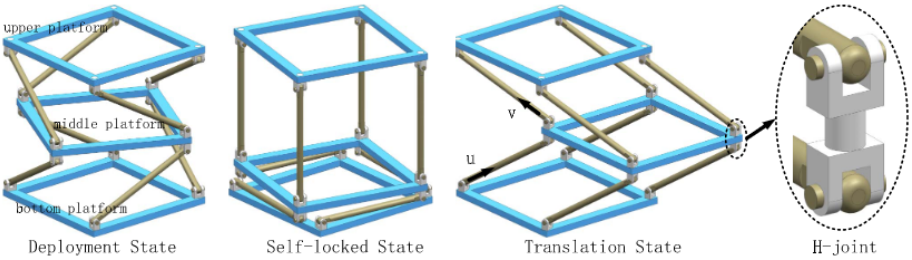

Figure 3.9: The second image starting from the left shows a certain configuration where the upper part of the structure is completely locked with the help of its joints [45].

- **Bricard-like mechanisms**: The large flexibility in terms of different positions taken by a reconfigurable structure is illustrated here. It is possible to consider a lot of different positions that could maybe lead to different configurations for the telescopes with a single structure. It is shown also that a very large compactness can be reached with reconfigurable structures. Example of this application is shown in Fig. 3.10 [44].

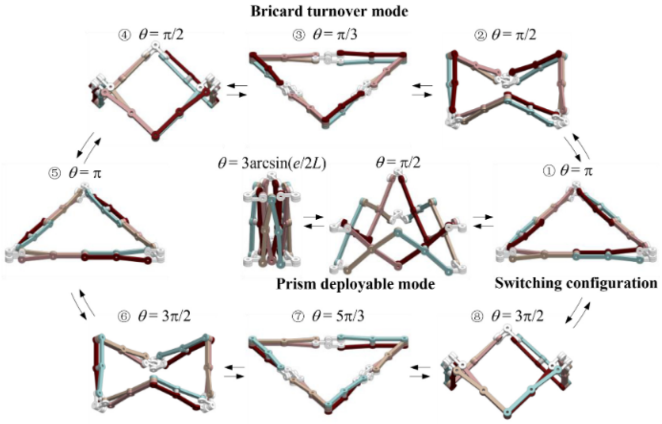

Figure 3.10: Bricard-like mechanisms. All the different possible positions with the same basis structure are shown [44].

3.1.5. Multi-stable structures

In mechanical engineering, a multi-stable structure is a structure that has multiple stable equilibrium positions or configurations. This means that the structure is able to maintain its stability and equilibrium in multiple distinct positions without external input or control [46].

Multi-stable structures are typically designed to be able to switch between these stable configurations with the application of a small amount of energy or force, allowing them to be used for a variety of applications, such as in sensors, actuators, and energy harvesting devices [46].

Multi-stable characteristics

As explained, a multi-stable structure is a mechanical structure that has multiple stable equilibrium positions, meaning that it can exist in different shapes or configurations without external forces being applied. This property is typically achieved through the use of shape memory alloys, bi-stable composites, or other materials with similar properties. The main characteristics of a multi-stable structure are its ability to store energy in the different stable states, its potential for self-actuation and self-reconfiguration, and its resistance to external disturbances [46].

Multi-stable structures can be suitable for deployable mechanical designs in some cases, particularly when compactness, lightweight, and adaptability are important. However, they can also present challenges related to their control, actuation, and reliability, which need to be carefully addressed. Overall, the suitability of a multi-stable structure for a particular deployable mechanical design depends on a variety of factors, including the specific application requirements, the environmental conditions, and the available resources [46].

State of the art

Some example of studies done on multi-stable structures are proposed in the following list:

- **Multi-stable mechanical meta-structures**: Fig. 3.11 shows a proposition of a type of meta-structure that exhibits multiple stable configurations, including level and tilted configurations [46].

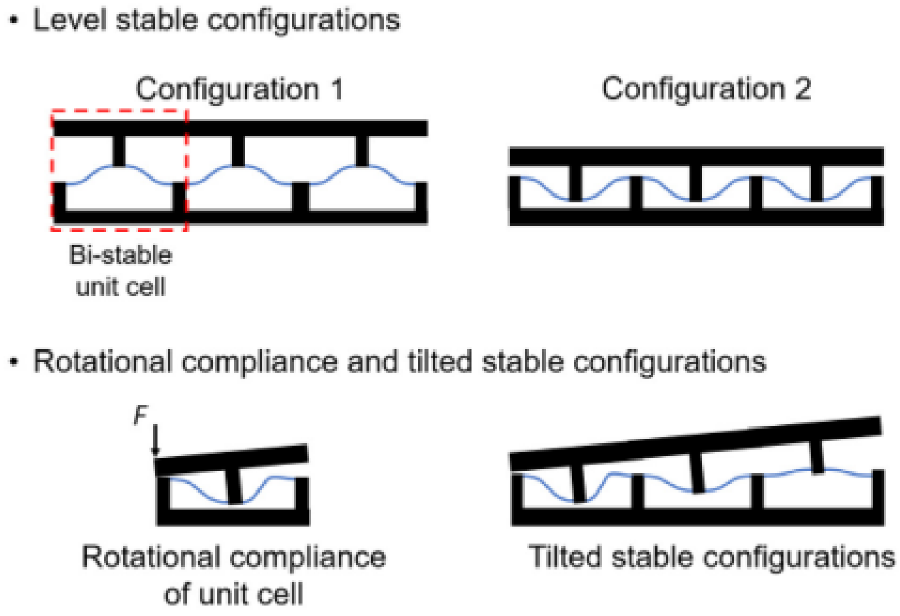

Figure 3.11: Meta-structure [46].

The meta-structure is based on the 2D and 3D arrangement of bi-stable elements, shown on Fig. 3.12, and utilises rotational compliance, bi-stability, and spatial arrangement of unit cells [46].

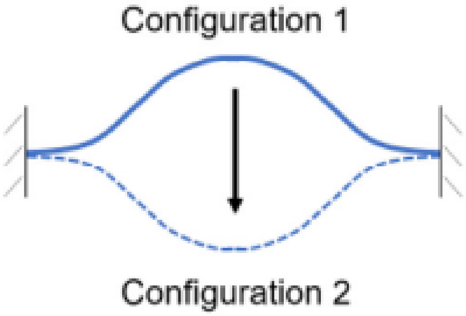

Figure 3.12: Bi-stable element [46].

The bi-stability of the unit cells and multi-stability of the meta-structure are characterised through experiments and finite element analysis. The transitions between level stable configurations are symmetric in terms of load-deflection response, while switching to the tilted stable configurations leads to asymmetric mechanical responses. The tilted stable configurations are less stable than the level configurations. Furthermore, the level and tilted stable configurations depend on the parallel and serial arrangements of the unit cells [46].

- **Transition elements**: Fig. 3.13 illustrates a new approach for designing multi-stable structures, based on the basic principle of bi-stable structures and the design of continuous multi-stable composite surfaces [47].

Figure 3.13: The multi-stable lattice structure [47].

This method divides the multi-stable plate into deformation and transition elements, with appropriately tailored stiffness. This reduces the geometric compatibility problem of multi-stable composite structures. The new multi-stable structures have different sizes, layers, one-direction splicing, and two-direction splicing. Experimental results show that these structures not only reduce geometric compatibility but also have better designability of layers and sizes, and enhanced deformability. The maximum number of shapes reached ten in the experiment, and the shapes of the new multi-stable structure can theoretically be any value [47].

3.1.6. Inflatable deployable structure

An inflatable deployable structure is a mechanical structure that is designed to be deployed by inflating it with gas or liquid. In mechanical engineering, these structures are used in a variety of applications, including space exploration, aerospace, civil engineering, and military applications [48].

Inflatable structures can be made of various materials, including polymers, fabrics, and metals. They can be designed to be rigid or flexible, depending on the application. The main advantage of inflatable structures is that they are lightweight and compact, making them ideal for transportation and deployment in remote or hard-to-reach locations [48].

In aerospace applications, inflatable deployable structures are used for a variety of purposes, such as solar sails, antennas, and habitats. In civil engineering, they can be used for temporary structures, such as shelters or bridges. In military applications, inflatable structures can be used for rapid deployment of field hospitals, command centres, and other facilities [48].

Inflatable characteristics

Inflatable deployable structures, IDS, are lightweight, compact and have the ability to expand to a larger size [48].

One of the main advantages of IDS is their ability to be packed into a small volume, which is crucial for launch and deployment in space. They are also relatively lightweight compared to rigid structures, which reduces launch costs. Additionally, IDS can provide a larger area for certain applications, such as solar arrays or antennae, while minimising the storage space needed during launch. However, IDS are typically less structurally stable than rigid structures and require active control mechanisms to maintain stability. They may also be subject to material degradation from exposure to radiation and extreme temperature variations in space [48].

Overall, IDS are a promising technology for space applications, but their stability and durability must be carefully considered in the design process for any space mission [48].

State of the art

Here is a list of existing missions using the inflatable method for deployable structures.

- **Inflatable deployable antenna**: To achieve different goals in space, there is a need of big antennas that can be deployed. But, they need to be lightweight, low-cost, and reliable. A new type of deployable structures called *inflatable space structures*: These structures are lightweight and easy to deploy. NASA recognised the potential of this new concept and selected it for a flight experiment (Fig. 3.14) [49].

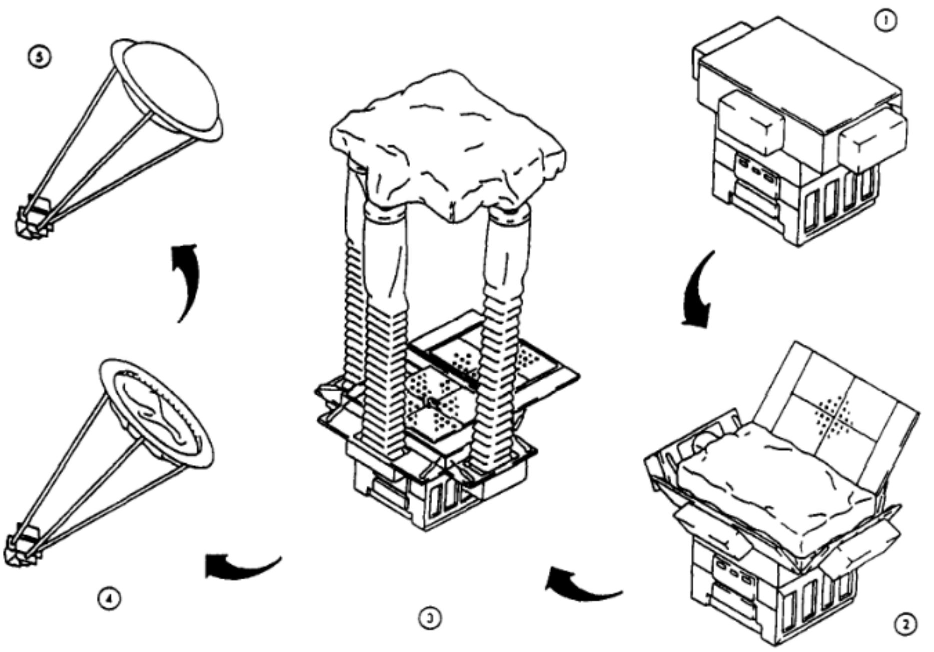

Figure 3.14: Inflatable antenna deployment sequence starting from the top right and following the arrows [49].

The experiment aimed to create a large, low-cost inflatable antenna structure and shows how well it works in space. To make sure that the antenna structure deploys properly, several things need to be considered. This includes: the starting position of the antenna after it's released from its container, how the structure changes during each deployment phase, how fast the different parts move, and how long it takes for each phase to inflate. The deployment process begins with the opening of the container doors, which ejects the folded structure using a spring-loaded floor plate. The struts start to deploy due to residual air and energy release, and after the structure has moved about 60 to 80 feet away from the container and the struts are partially extended, the deployment is finished by inflating the struts [49].

- **Project Echo**: Project Echo was a NASA project launched in 1960 with the goal of creating an inflatable, passive communication satellite. The satellite consisted of a 30-meter diameter aluminised Mylar balloon, which was inflated in space and used to reflect radio signals back to Earth. The balloon was stabilised by a spin mechanism that kept it oriented towards the Earth, and it was able to maintain its shape and position in orbit for several years due to the lack of atmospheric drag at its altitude. The project was considered a success and demonstrated the feasibility of using inflatable structures for space applications. Later, project Echo 2 came, Fig. 3.15. Bigger than the first version, it is also still considered as a success today [48].

This method allows a structure to become really large, which is very interesting in the case of this research. The main problem faced by this project is that, due to its huge size, it is subject to micrometeorites and orbital debris that could completely destroy the entire structure [48].

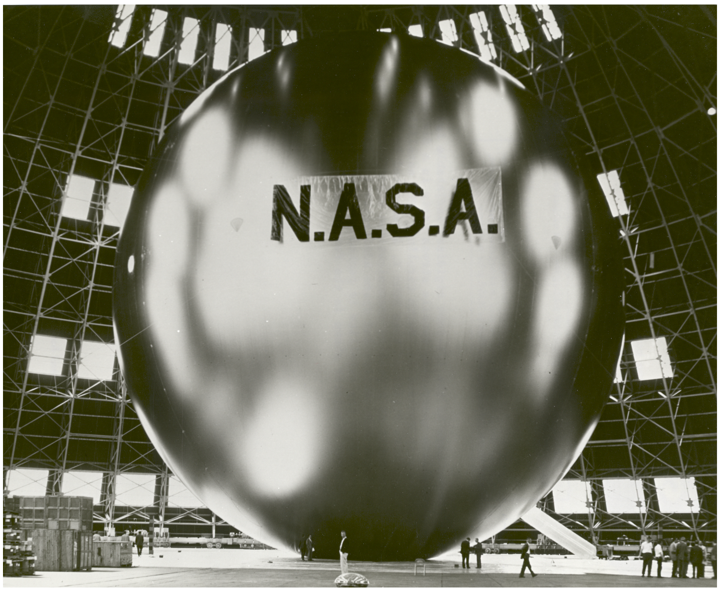

Figure 3.15: Picture of project Echo 2. Next to it, humans can be seen illustrating the huge size of the satellite [48].

3.1.7. Multi-criteria analysis

In order to select the structure to design, a multi-criteria analysis, also known as a multi-criteria decision analysis or multiple criteria decision-making, has been used. It is a systematic approach used to evaluate and compare alternatives based on multiple criteria or factors.

These factors are linked to the requirements defined at the start of the study, i.e.: maximising the baseline (for a given space required) and minimising misalignment between telescopes thanks to a sufficiently rigid structure.

A criterion related to design complexity has also been added. The simpler a design is, and the easier and more reliable it is to implement, the more it will influence the decision-making.

Other criteria such as weight or budget could also have been taken into account. However, these criteria were not asked in the requirements for this preliminary design. They were thus not taken into account.

In a multi-criteria analysis, the decision problem is typically complex, involving various criteria that may have different weights or priorities. The aim is to assess and rank the alternatives based on their performance across these criteria, taking into account the decision maker's preferences and priorities. Here is an explanation of the performance criteria that will be used for this analysis:

- **Rigidity R**: This has to be understood as the capability of the structure to resist to the external loads applied on it. Higher is the rigidity of the structure, lower is the deformation. A high rigidity will bring of course a lower misalignment. To give exact value for the structure is not the key. The score given in Tab. 3.1 is based on an overall evaluation of what emerges from the literature review.
- **Baseline B**: The baseline size must be the largest possible as explained in the requirements. If the structure allows a higher b, then it will get a better rating than a structure that does not allow to maximise the baseline. As it is a consequence of the geometry and the design of the structure, it is quite obvious to give the rating.

- **Simplicity S**: The simplicity of a structure is also a key factor. Higher is the simplicity and easier will be the design and the modelling of the structure with less features and thus, an easier set-up. So, higher is the simplicity , higher will be the rating. The evaluation has been made based on the literature review.

Tab. 3.1 shows the multi-criteria analysis performed during this research. The principle of this table is to allocate to a type of structure a number of points ranging from -1 to +1 for each criterion evaluated. These points are therefore a value given according to what emerges from the literary review, and it is important to understand that all these types of structures could very well be used for this research. The aim here is simply to help making a choice between these structures. Finally, each criterion will be weighted according to the importance attributed to it in this thesis, such that the maximum rigidity **R** is worth 10, the maximum baseline **B** is also worth 10 and the maximum simplicity **C** is worth 5.

Criteria	**R**	**B**	**S**	**Final score**	
Weight of criteria	10	10	5	With **B** (/25)	Without **B** (/15)
Ultra-stable	+1	-1	+1	+5	+15
Origami	+1	+1	0	+20	+10
Reconfigurable	0	+1	-1	+5	-5
Multi-stable	0	+1	0	+10	0
Inflatable	-1	+1	-1	-5	-15

Table 3.1: Multi-criteria analysis of different types of mechanical structures. **R** represents the stiffness of the structure, **B** represents the baseline length achievable and **S** represents the simplicity for modelling such a structure. Green colour (+1) means that it is an advantage, blue colour (**0**) means that it is neither an advantage nor a disadvantage and red colour (**-1**) means that it is a disadvantage for this research.

In the final score, two results are displayed in order to consider the structure with and without the optimisation of the baseline. It shows clearly that if the baseline requirements is not considered then an ultra stable structure should be chosen. However,when the baseline requirements is considered, a good option to explore is the origami structure which got the best score. That is what will be done in the following chapters.

It has to be clear also that the origami is not at all the only possible solution. It is just the choice made in this study based on the predefined requirements and this multi criteria first analysis.

However many other types of structure could be interesting at different levels and could even be much more interesting if some other requirements were added.

3.2. Material resistance

In the case of this research, a static deformation analysis needs to be done on the fully deployed structure in order to verify if the mission requirements are respected.

The purpose of a material strength analysis is to determine the deformations that a structure may undergo when exposed to external loads. In the context of this mission where the satellite is positioned in the Lagrange orbit L2, the fully deployed structure will be subject to a multitude of external constraints, but mainly to the gravitational acceleration caused by the attraction of the Earth, the Sun, and the Moon. Other factors also contribute to this acceleration, such as the

Coriolis forces, the effect of solar tides, solar wind pressure, space debris or micrometeorites collisions, etc., but these will not be taken into account in the preliminary study. For a final design, they will obviously have to be considered deeply.

The acceleration perceived by the satellite will be uniformly distributed over the entire structure, and what will cause deformation will come from the mass distribution. Indeed for most of the configurations of telescopes shown in Fig. 2.3, these telescopes are positioned at the extremity with a high mass compared to the rest of the structure. Deformation arrows can thus be calculated using a 3D finite element model. A deformation arrow will show misalignment of the telescopes with each other. Moreover, this misalignment will drastically reduce the nulling effect on the star and therefore the instrument's detection efficiency.

For the system to function optimally, it is thus necessary to have the least possible angle between the telescopes pointing axis alignments. Therefore, a parametric study must be carried out to identify the parameters that induce the least deformation and thus the least misalignment between the telescopes that is compatible with the deployment system. It was decided in the context of this work to respect a maximum misalignment requirement between the different telescopes of 30 arcsec.

The material resistance analysis starts by creating a 3D model of the deployable structure. It is done with the software **SolidWorks**. Once this is done, it is transferred to another software, **COMSOL Multiphysics**, where the maximal acceleration applied to the structure is added to study the deformations. Finally, with a more precise model of the deployable system produced on **SolidWorks** and transferred to **COMSOL Multiphysics**, the kinematic of the deployment can also be analysed.

A short description of the two cited softwares is given in the following sections.

3.2.1. Software used

SolidWorks

SolidWorks is a 3D CAD software widely used in industry and engineering for designing and modeling mechanical parts, assemblies, and systems. To illustrate how this software can actually be used, a simple model composed of two panels has been created. This model is considered representative because modelling a structure and making it work necessarily involves a system composed of several bodies in relation to each other.

To create a 3D model in **SolidWorks**, the user typically starts by sketching a 2D profile, which can then be extruded or revolved to create a 3D object. Alternatively, the user can directly create 3D objects using features like lofting, sweeping, and filleting.

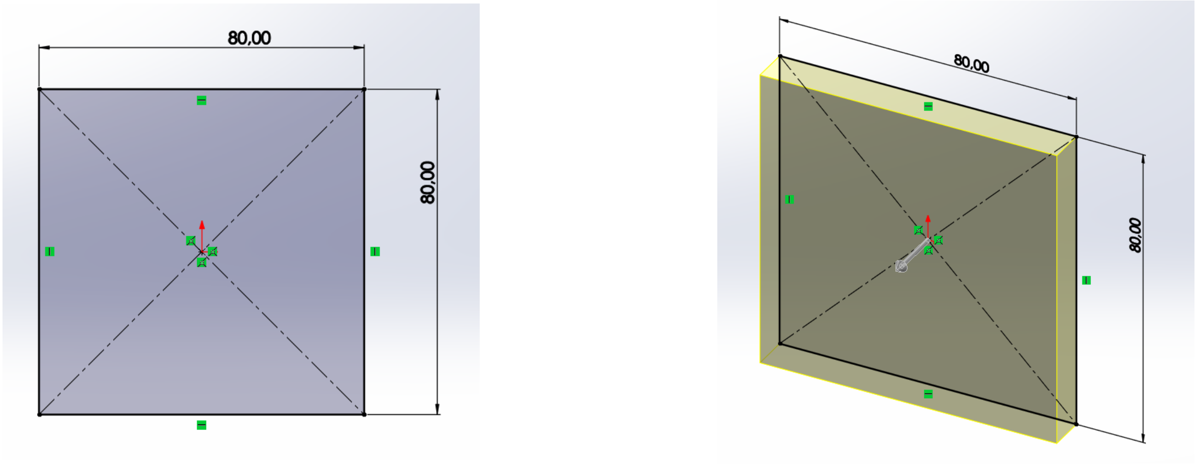

Figure 3.16: On the left side, the 2D profile of a single panel is shown. On the right side, a extruded function has been applied to the 2D profile to obtain a single 3D panel that will composed the example model.

Once the 3D model is complete, the user can use **SolidWorks**’ assembly tools to create a multi-body model. This is done by defining constraints to control the relations between the different part of the system.

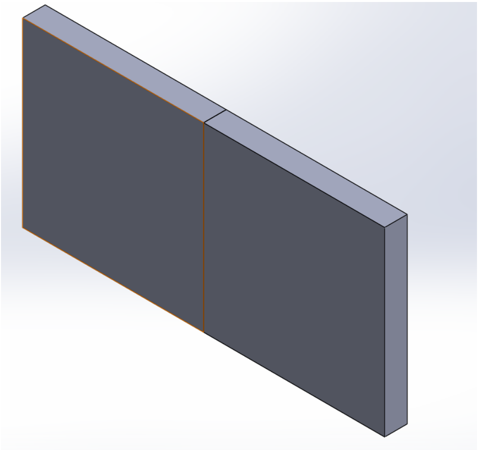

Figure 3.17: Two panels have been added in a single model. They are linked by a constraint imposing the panels to be connected at the two edges highlighted in orange in this figure, leaving only one rotational degree of freedom around the joint between the two panels.

The structure is first modelled in **SolidWorks** and its response to a uniformly distributed static load, representing the acceleration experienced by the structure in its orbit, is tested in another software: **COMSOL Multiphysics**. In addition, once the dimensions have been determined thanks to the **COMSOL Multiphysics** tests, the new dimensionned **SolidWorks** model is subjected to a kinematic analysis on **COMSOL Multiphysics** to see if a collision-free and physically feasible deployment is possible.

COMSOL Multiphysics

COMSOL Multiphysics is a powerful software package used for multi-physics simulations and analysis. It enables engineers and scientists to model and simulate a wide range of physical phenomena, such as structural mechanics, heat transfer, fluid flow, and electromagnetic, among others.

Static study The first step of this research consists to perform a static study where the structure's deformations due to a certain acceleration applied on it are analysed. **COMSOL Multiphysics** can be used to set up and solve a structural mechanics problem. The software allows users to define the geometry and material properties of the structure, apply boundary conditions, and specify the acceleration profile.

By using the structural mechanics module within **COMSOL Multiphysics**, users can simulate the dynamic response of the structure to the applied acceleration. The software employs finite element analysis techniques to calculate the deformation and stress distribution throughout the structure. Fig. 3.18 shows a example model that is used to illustrate the software [50].

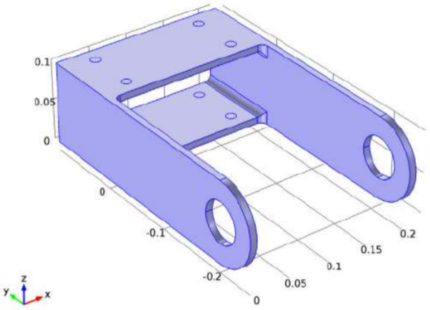

Figure 3.18: The model showcased consists of a bracket and the accompanying mounting bolts, all constructed from steel. It is assumed that the mounting bolts are fixed in place and securely bonded to the bracket. For this example, the load is pointing along the negative y-axis only [50].

After setting up the simulation, **COMSOL Multiphysics** provides visualisation tools to view the results. Users can observe the deformations in real-time or analyse the results post-simulation. The software offers various visualisation options, including contour plots, displacement vectors, and so on, allowing users to gain insights into the structural behavior and assess the stability and deformation caused by the applied acceleration. For the same example, the Von Mises stress distribution, the maximum total displacement and the principal stresses in the bracket are asked and shown on Fig. 3.19.

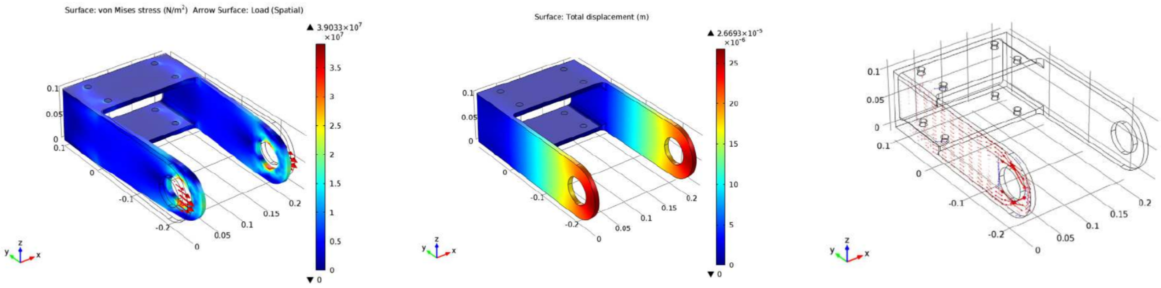

Figure 3.19: From left to right, the Von Mises stress distribution, the total displacement and the main stresses in the bracket.

Time dependant study With the static study, the main dimensions of the system are known. Then, a kinematic analysis needs to be done to check if the deployment appears to be physically feasable. To do so, a time dependant study must be considered to introduce the time parameter.

The users just need to add some prescribed time-depending motions at the level of the different bodies composing the system. After the study is performed, the **COMSOL Multi-**

physics’ built-in animation tool can be used to obtain an overview of the deployment. An example given by **COMSOL Multiphysics** [51] is shown at Fig. 3.20. It shows the motion of a double pendulum before and after the simulation and animation.

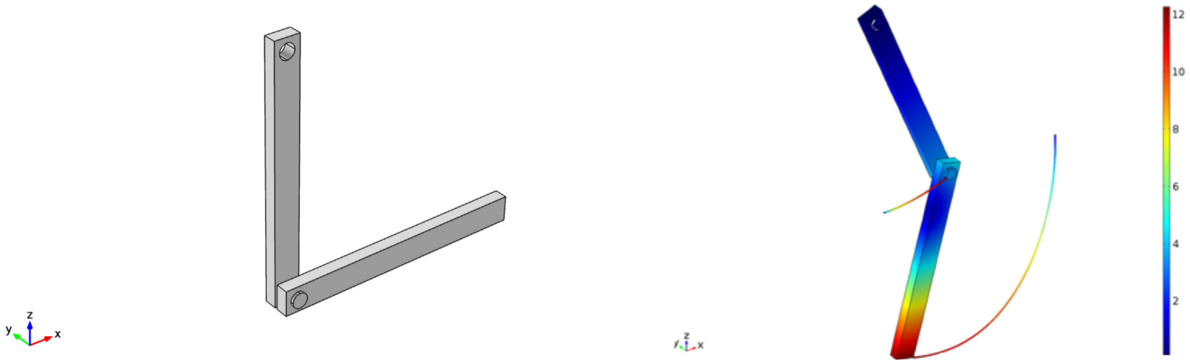

Figure 3.20: On the left, the CAD model of the double pendulum [51]. On the right, the double pendulum animation [51].

Summary Overall, **COMSOL Multiphysics** is a versatile software tool that enables engineers and researchers to accurately model, simulate, and analyse complex physical phenomena, including the deformation of structures subjected to acceleration. It provides a comprehensive platform for investigating and optimising designs to ensure structural stability and performance.

For this research, **COMSOL Multiphysics** will be firstly used at the level of testing the deformations. The model will be built on **SolidWorks** and then transferred to **COMSOL Multiphysics** via the *Livelink* option included in the **COMSOL Multiphysics** software. A static load is then applied uniformly over the entire model and the response of the structure, and in particular the response of the different telescopes, is analysed to see the extent of observable telescope misalignment. On the basis of these initial results, an iterative process will be carried out in which the dimensions of the elements making up the structure will be modified on **SolidWorks** and the new model will be sent back to **COMSOL Multiphysics** with the aim of reducing this misalignment of the telescopes as much as possible. The second aim of the use of **COMSOL Multiphysics** is to validate that the design of the structure is correctly modelled to achieve a collision-free and physically feasible deployment.

4

Conceptual Design

Based on the criteria at the end of chapter 3, the decision to focus mainly on the origami type of structures to design the structure studied in this thesis has been made.

In this chapter, different types of origami are going to be presented and the geometry of the selected origami structure will be described in more details.

This geometry definition will be used in chapters 5 and 6 to confirm that the selected structure is suitable to meet the defined requirements.

4.1. Preliminary design

This section presents a series of designs for deployable space origami structures.

These potential ideas take their inspiration partly from the literature review made in chapter 3 about the possibilities for the deployment.

4.1.1. Reinforced Square Origami Flasher

A square origami flasher is an intricate and visually captivating design that showcases the artistry and precision of origami folding techniques. This particular origami model starts with a square sheet of a certain material and transforms into a stunning geometric structure with flashing panels. The square flasher design is achieved through a series of intricate folds that create interlocking flaps and pockets, resulting in a dynamic and eye-catching pattern Fig. 4.1.

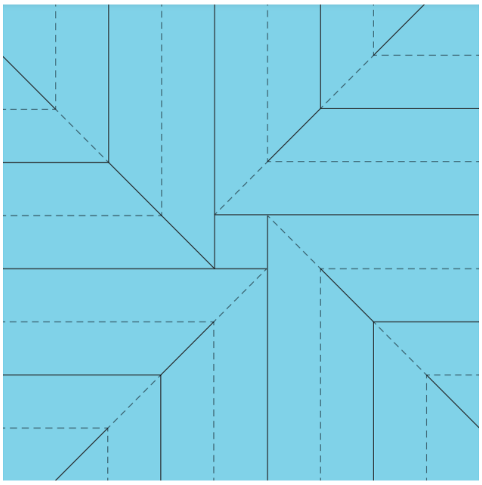

Figure 4.1: Square origami flasher pattern. Dot lines are valley folds and full lines are mount folds [52].

The advantage of a structure inspired by such a pattern lies, of course, in its large size after deployment. Fig. 4.2 demonstrates the deployment of a sheet following this pattern and illustrates how the structure can be compacted and subsequently deployed.

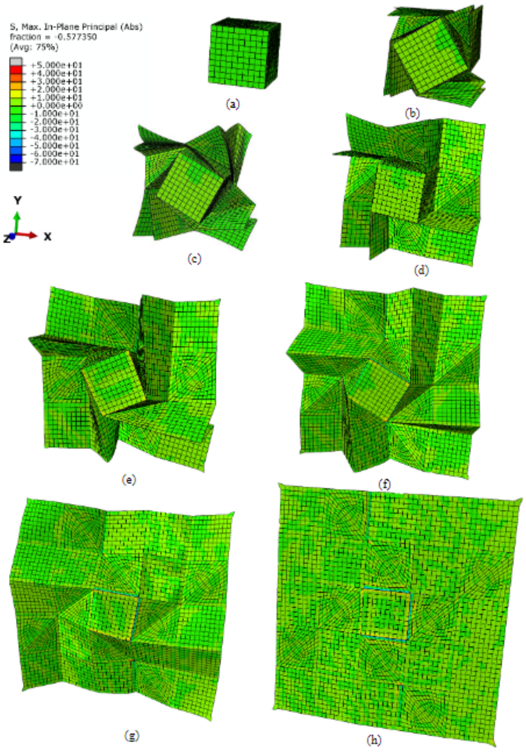

Figure 4.2: Square origami flasher deployment [52].

Such a structure naturally possesses some rigidity when deployed; however, it remains susceptible to bending within its plane. Therefore, it needs to be reinforced using another structure. This reinforcement structure takes the shape of a mechanism that is represented here by four mechanical arms, each consisting of three segments and three revolute joints. These arms will serve both as reinforcement for the overall structure, attaching to the origami, and as guides during deployment, ensuring consistent unfolding throughout.

This structure can achieve significant stability while having a large surface area upon deployment. Another major advantage would be the requirement of only a single rotary motor located at the centre of the structure, which would act on the robotic arms to fully deploy the structure. Fig. 4.3 depicts the three-dimensional representation of this concept considering the rectangle configuration of the telescopes shown at Fig. 2.3b.

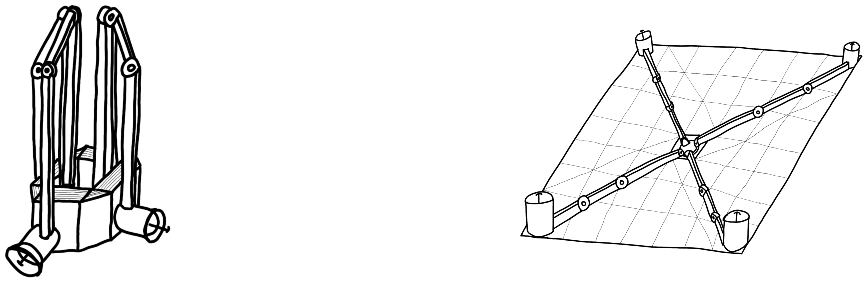

(a) Draw of the undeployed state of the reinforced square origami flasher.

(b) Draw of the deployed state of the reinforced square origami flasher.

Figure 4.3: These images are hand-drawn by Sacha Iannello and are not at scales.

4.1.2. Reinforced Octagon Origami Flasher

The flasher origami possesses the amusing characteristic of being able to work with any polygonal base. Whether it is a square as in the previous case or a polygon that approximates the shape of a circle, such as an octagon in this instance. The reason for wanting to approach a circle is as follows: there are many more possibilities for telescope configurations. In the square flasher origami, the rectangular/square configuration is the only one considered! Here, there are more possibilities: a triangular, diamond, rectangular, and even linear configuration is possible.

The advantages and disadvantages of this octagonal flasher origami are the same as for the square base, with the exception of an additional constraint here, considering a significantly higher number of panels and thus greater complexity. Fig. 4.4 showcases the three-dimensional design of the octagonal flasher origami, also considering four robotic arms to represent the rectangular configuration of the telescopes shown at Fig. 2.3b.

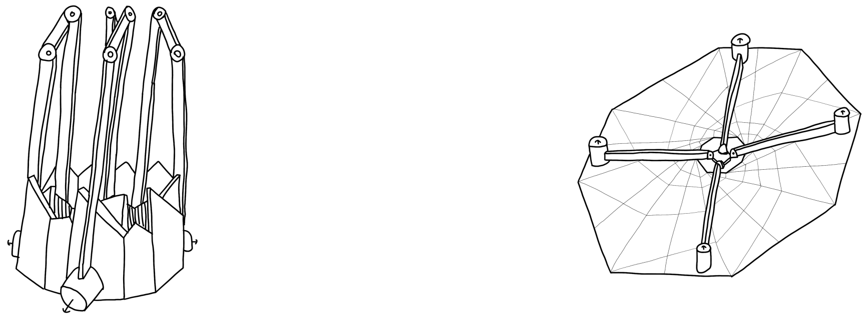

(a) Draw of the undeployed state of the reinforced square origami flasher.

(b) Draw of the deployed state of the reinforced square origami flasher.

Figure 4.4: These images are hand-drawn by Sacha Iannello and are not at scales.

4.1.3. Deployable Tubes

In section 3.1.3, a type of origami was mentioned to provide an example of origami deployment. Fig. 3.5 illustrates this deployment at two different angles. The following idea then emerged: why not use these tubes as connections between the different telescopes? For instance, considering the linear configuration of the telescopes, deployable tubes could be placed between each pair of telescopes, resulting in a structure that is much longer upon deployment than the height of Ariane 6.

By utilising these deployable tubes as linkages, the overall structure can achieve a greater extension, allowing for enhanced functionality and reach. This concept introduces the possibility of creating a telescope array that surpasses the limitations of individual telescope height, enabling a broader observation range and increased versatility. The deployable tubes would serve as flexible connectors, facilitating the expansion of the structure during deployment. These tubes could be designed to withstand the harsh conditions of space and thus possess the necessary stability to maintain the alignment of the telescopes. The resulting elongated structure would provide a larger aperture and improved resolution, enhancing the overall performance of the telescope system. This innovative approach of using deployable tubes as interconnections presents numerous advantages. It offers a scalable and adaptable solution, allowing for the addition or removal of telescopes as required. Moreover, the compact storage of the tubes during transportation minimises the payload volume, making it feasible for deployment using existing launch systems such as Ariane 6. Fig. 4.5 show the different configurations of this idea.

(a) Draw of the undeployed state of the reinforced square origami flasher.

(b) Draw of the deployed state of the reinforced square origami flasher.

Figure 4.5: These images are hand-drawn by Sacha Iannello and are not at scales.

While the idea of using deployable tubes as linkages between telescopes presents several advantages, it also carries some potential disadvantages that need to be considered. These disadvantages include for example:

- **Structural Integrity**: The integrity and stability of the entire structure rely heavily on the strength and reliability of the deployable tubes. Any failure or malfunction in the tubes could compromise the overall functionality and performance of the telescope array. Rigorous testing and quality control measures would be necessary to ensure the tubes can withstand the demanding conditions of space and maintain their structural integrity over extended periods.
- **Potential Points of Failure**: The presence of deployable tubes introduces potential points of failure within the system. Any mechanical issues, such as jamming, misalignment, or damage to the tubes, could disrupt the deployment process or hinder the proper functioning of the telescopes. Redundancy mechanisms and robust engineering practices would need to be implemented to mitigate these risks.
- **Cost and Development Time**: The development and implementation of a complex system using deployable tubes would likely require significant investment in research, development, and testing. The engineering challenges, coupled with the need for rigorous verification and validation, could extend the development timeline and increase overall project costs.

4.1.4. Selected solution

There are numerous other potential design ideas for this mission, aiming to create the largest and most stable deployable interferometer possible. These ideas can draw inspiration from various sources, including nature and beyond. By exploring alternative design concepts, a multitude of possibilities and innovative approaches can be exploited. But with all these ideas being feasible, a choice had to be made. To make this decision, the pros and cons were carefully considered, and the rest of this research will focus solely on the reinforced square origami flasher.

The decision to select the reinforced square origami flasher idea over the octagonal origami flasher reinforced, the deployable tubes between telescopes or the other potential idea is based on several factors. Indeed, the deployable tubes structure is not reinforced like the reinforced origami flashers ones, which makes it more subject to deformation when subjected to external loads. Moreover, compared to the deployable tubes between telescopes, the square flasher origami concept offers a simpler and more self-contained deployment mechanism. This simplicity in deployment reduces the risk of mechanical failures or alignment issues that may arise when utilising deployable tubes.

When it came to selecting between the square and octagonal reinforced origami flashers, it was the simplicity of modelling that counted in favour of the reinforced square origami flasher. Indeed, in the case of the reinforced octagonal origami flasher, more than eighty panels, forming eight spirals, would have had to be considered and only four mechanical arms would have been able to guide these panels in order to obtain correct deployment. The reinforced square origami flasher, on the other hand, will be made up of around sixty panels forming four spirals and also guided by four mechanical arms, which is much simpler.

The square flasher origami concept was thus chosen in the aim of this thesis in order to maximise the potential size of the deployable interferometer while maintaining stability and practicality. It is important to note that there may be other ideas that could be more efficient and effective. However, the decision to pursue the square flasher origami design was made to explore its advantages in terms of post-deployment size, ease of deployment, structural integrity, and feasibility. This choice aligns with the mission's overarching goals and specific requirements, while also recognising the need for experimentation and the possibility of discovering even more effective designs.

4.2. Square Origami Flasher optimisation

4.2.1. Spiral research

This origami has the particularity of being inspired by spirals. A study was conducted on **Matlab** to determine the type of spiral, the dimensions of each part of these spirals, and the angles to be used.

In the context of this project, a square origami has been chosen, as previously mentioned. However, this particular origami possesses a unique characteristic: it draws inspiration from spirals. To determine the specific type of spiral, the dimensions of each spiral section, and the angles to be used, a comprehensive study was conducted using **MatLab**. This exploration aimed to identify the most suitable spiral configuration for the origami design. Before delving into details, it is important to explore various types of spirals found in different fields such as mathematics, biology, physics, art, and more. Understanding these spirals will provide a broader context for the subsequent analysis and design choices.

- **Logarithmic Spiral**: A logarithmic spiral is a curve that wraps around a central point with a logarithmic progression as shown in Fig. 4.6. This means that the distance between the spiral's coils increases proportionally to a logarithm. Logarithmic spirals are often found in nature, for example, in the shells of certain molluscs, the arms of galaxies, or the growth patterns of certain plants [53].

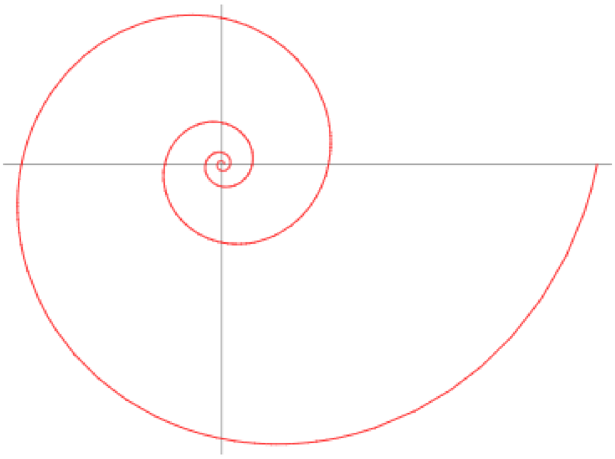

Figure 4.6: Logarithmic spiral [53].

- **Archimedean Spiral**: An Archimedean spiral is a curve that wraps around a central point with a constant distance between the coils as shown in Fig. 4.7. It is one of the most common types of spirals and is used in many applications, including the construction of certain stairs, springs, or the propellers of certain ships.

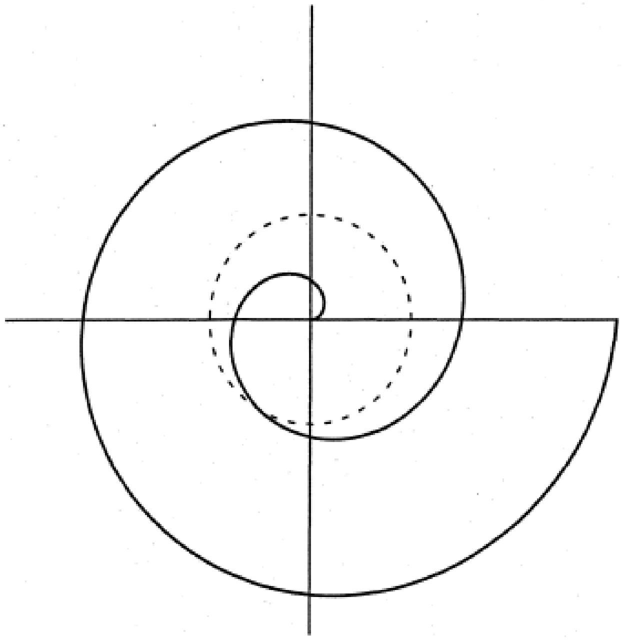

Figure 4.7: Archimedean spiral [54].

- **Fibonacci Spiral**: The Fibonacci spiral is a spiral that is based on the Fibonacci sequence, a mathematical sequence where each number is the sum of the two preceding numbers (1, 1, 2, 3, 5, 8, 13, 21, etc.) as shown in Fig. 4.8. This spiral is often used in art and design due to its aesthetically pleasing proportions and its frequent occurrence in nature, such as in the arrangements of leaves on certain plants.

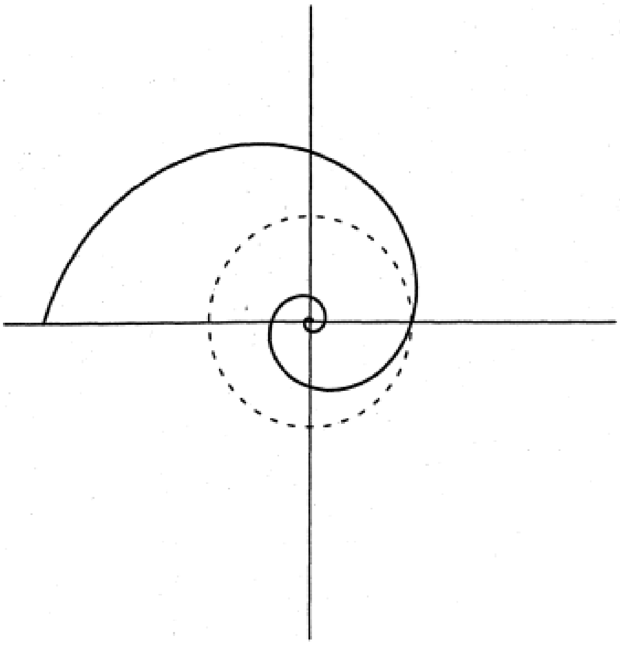

Figure 4.8: Fibonacci spiral [54].

- **Hyperbolic Spiral**: A hyperbolic spiral is a curve that wraps around a central point with a rapid increase in the distance between the coils as one moves away from the central point as shown in Fig. 4.9. It is used in certain types of springs, parabolic antennas, or in the design of certain architectural structures.

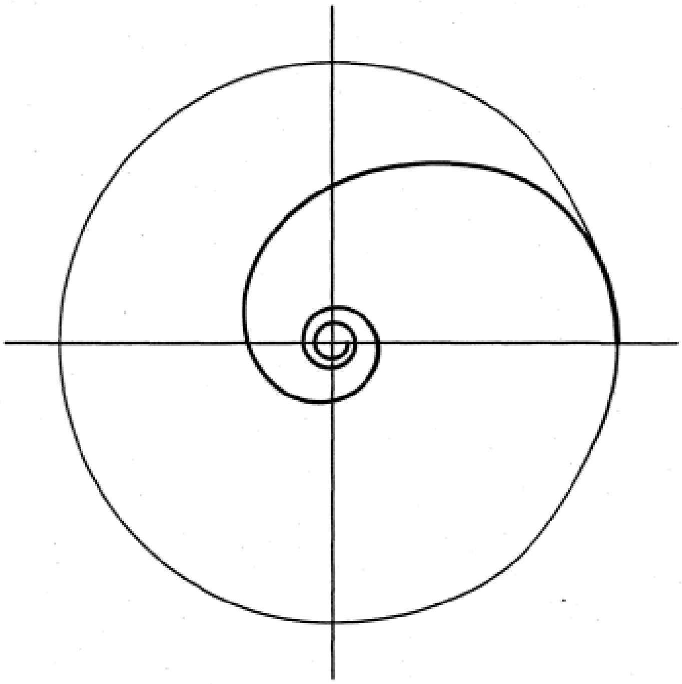

Figure 4.9: Hyperbolic spiral [54].

The logarithmic spiral has the best stiffness characteristics of the various spirals mentioned.

Indeed, the logarithmic spiral cuts all the spokes at the same constant angle, giving it a self-similar property. This means that the shape of the spiral does not change when it is expanded or reduced. The logarithmic spiral is therefore more resistant to static load than other spirals, which deform more easily [55]. The Archimedean spiral, for example, does not have this self-similar property. It is defined by a point moving uniformly along a straight line that is itself rotating uniformly around a point [56]. Its curvature increases in proportion to the angle covered [57], making it more sensitive to variations in load.

Obviously, there are many other types of spirals, each with its own characteristics and specific applications in various fields of science, art, architecture, etc. **MatLab** code Spitype.m (App. A.1) gives a comparison of four of these spirals; Logarithmic, Archimedean, Fibonacci and Hyperbolic, terms of the shape when considering few components only on Fig. 4.10.

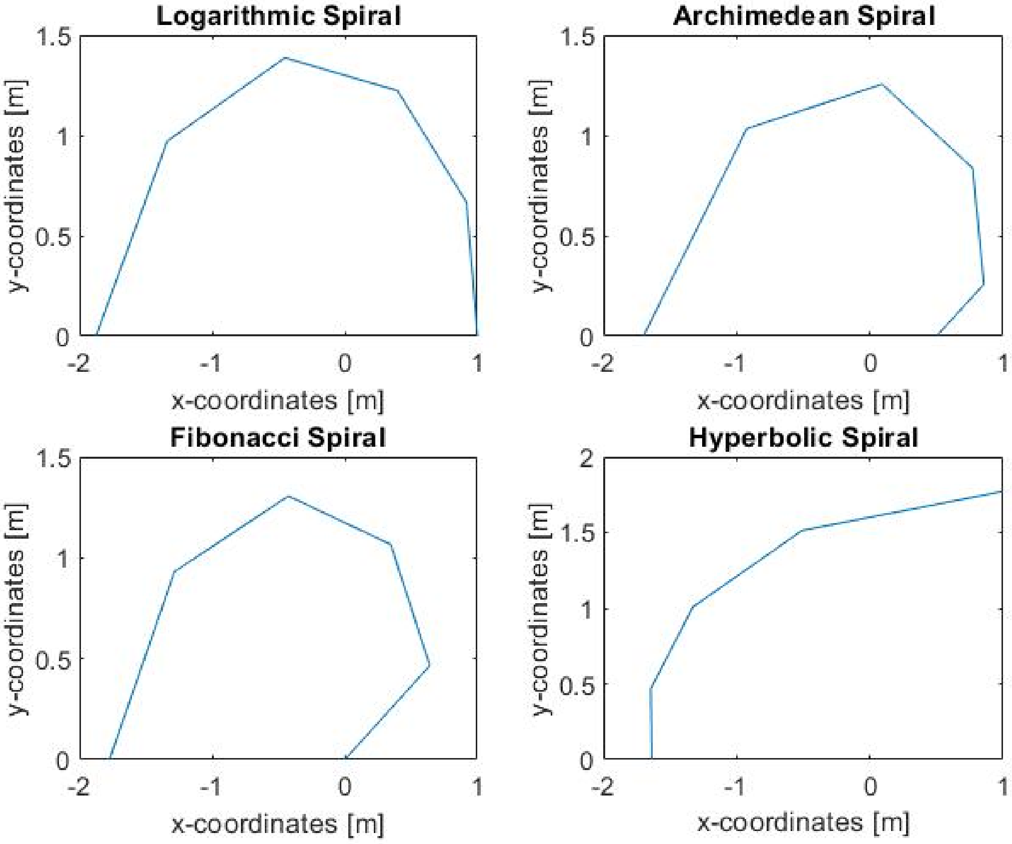

Figure 4.10: Comparison of four types of spiral: logarithmic, Archimedean, Fibonacci and hyperbolic.

In the case of the square origami flasher, it is evident that the spirals it draws inspiration from possess distinct characteristics. Specifically, the segments comprising one of the four spirals in the structure lengthen as they move away from the square base of the origami. Furthermore, the angles between each segment remain constant, at 90 degrees in this case, which is a unique feature of this square origami flasher (octagon one has 135 degrees between each of its segment). When approximating a spiral using a sequence of straight line segments of different lengths, all inclined at the same angle relative to the previous one, it generally corresponds to a *logarithmic spiral* or *equi-angular logarithmic spiral* which is a good thing due to its higher stiffness capability [55].

In summary, a sequence of straight line segments of different lengths, all inclined at the same angle relative to the previous one, generally corresponds to an approximation of the logarithmic spiral or the equi-angular logarithmic spiral. This means that the square origami flasher is composed of a specific type of logarithmic spiral where each segment increases by a different factor. In the case of the square shape, the second segment of one spiral will be 3 times the length of the first segment, the third segment will be $\frac{5}{3}$ times the length of the second segment, and the fourth segment will be $\frac{6}{5}$ times the length of the third segment as shown on Fig. 4.11.

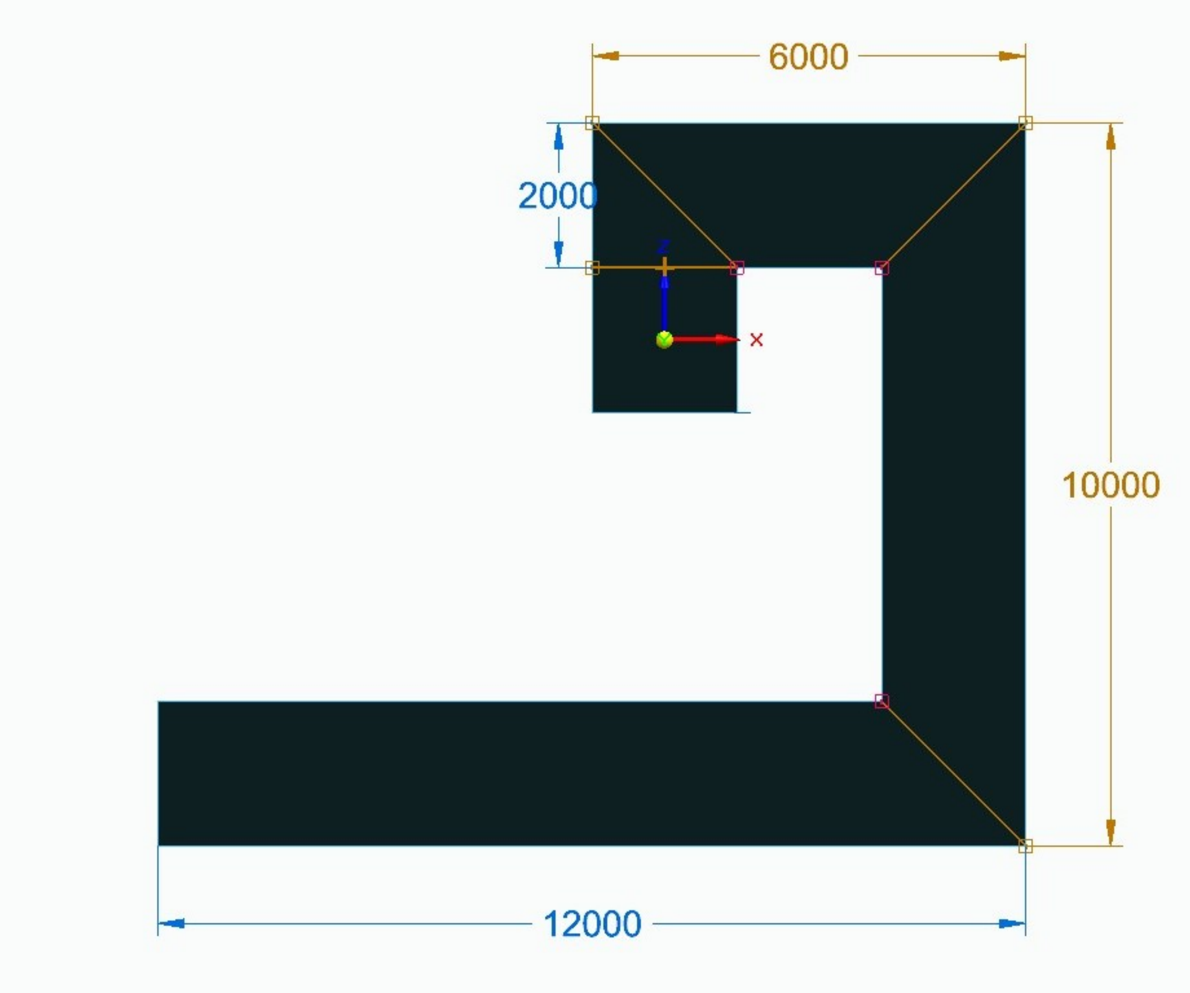

Figure 4.11: One of the spiral arms fully deployed is shown here. As an example, a first length of 2000 mm long for the first segment of one spiral arm is chosen. As explained, the second segment will be 6000 mm long, the third one will be 10000 mm long and the last one will be 12000 mm long. This scheme has been realised with the software **SolidWorks**.

4.3. Proof of concept

A small paper-made model has been realised in order to ensure the feasibility of this deployment. Fig. 4.12a, 4.12a, 4.12a and 4.12c show the successive phase of deployment of the origami flasher.

(a) Folded state of the origami flasher.

(b) Deployment phase of the origami flasher.

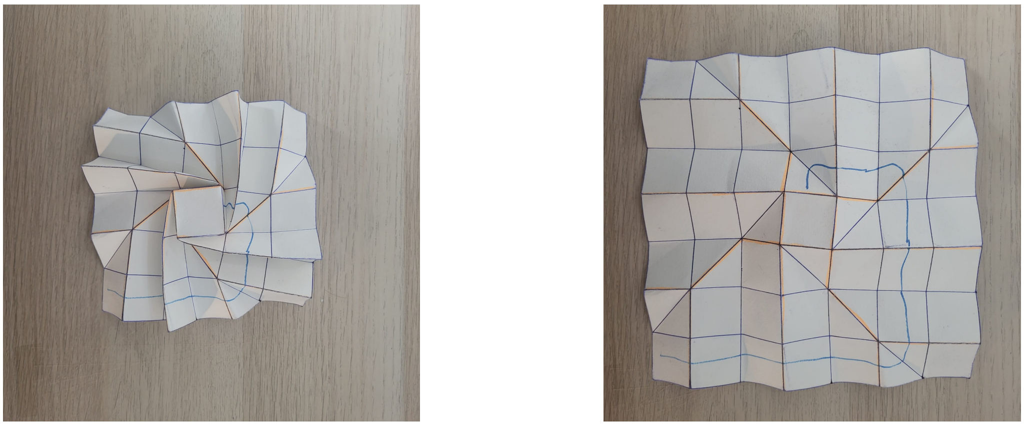

(c) Deployment phase of the origami flasher.

(d) Deployed state of the origami flasher.

Figure 4.12: This model has been made with a thick drawing paper by Sacha Iannello.

5

Static Analysis

This chapter covers the static analysis of the model. The first step is a review of some potential materials to be used for the structure. Based on the choice of the material, one will consider the useful characteristics of the material to input into the simulation model. With this model, the mass of the components of the structure will be calculated and then the forces applied to the structure in a very conservative way, as the maximum acceleration on L2 orbit is considered.

The simulation will be made using 3D finite elements analysis. There will be mainly three phases in the followed methodology. The first one will consider a simplified model to estimate the thickness of the panel and the dimensions of the platform. During the second one, one will check the deflection of the platform with the spirals deployed. However, still no mechanical arms will be considered. Finally, a presentation of the complete model with the arms deployed will be made. In the last model, the simulation for different section of the arms will also be performed.

Based on that, a first preliminary design with dimensions is proposed before checking the deployment free of collision in the chapter 6.

All simulations were made using **COMSOL Multiphysics** software and **Solidworks**.

5.1. Material analysis

In the context of a space mission, an important parameter to take into consideration is the material used for the structure. In this research, at this stage of the design, there is no specific requirement about the material such as weight requirement or budget requirement that could lead to select some materials instead of other ones. As the goal of this chapter is to give a overall confirmation of the choice made with the structure, it has been decided to consider some common material used in space application and then to select the ones used based on some of their material properties (Young's modulus, Poisson's ratio, coefficient of thermal expansion and density).

The material properties that are considered for this material analysis are the following ones:

- **E** [GPa] - Young modulus,
- μ [-] - Poisson's coefficient,
- ρ [$\frac{\text{kg}}{\text{m}^3}$] - Density,
- σ_y [MPa] - Tensile yield strength: Below the yield limit, a material deforms elastically and returns to its original shape when the applied stress is removed,

- α [1/C°] - Coefficient of Thermal Expansion: Help predict how much a material will expand or contract when exposed to temperature changes. Materials with low CTE values tend to be more stable and less prone to warping or cracking when exposed to temperature changes.

- **CFRE, epoxy matrix**: Carbon Fibre Reinforced Epoxy (CFRE) shows very good mechanical and thermal properties, It is also a composite used to save weight. All of that makes it an excellent candidate [58].
  - $E = 150$ GPa [58],
  - $\mu = 0.28$ [-] [58],
  - $\rho = 1600 \frac{\text{kg}}{\text{m}^3}$ [58],
  - σ_y = 1100 MPa [58],
  - $\alpha = 4^{-05}$ 1/C° [58].

- **Aluminium 7050-T7451**: Aluminium 7050-T7451 was used for the simulation [59] [60]. The material properties that will be used for simulation are the following ones:
  - $E = 71.7$ GPa [60],
  - $\mu = 0.33$ [-] [60],
  - $\rho = 2830 \frac{\text{kg}}{\text{m}^3}$ [60],
  - σ_y = 469 MPa [60],
  - $\alpha = 2.304^{-05}$ 1/C° [60]:

- **Titanium Ti-6Al-4V (Grade 5), Annealed**: Titanium alloy is also considered [61][62]. Its material properties are given as follow:
  - $E = 113.8$ GPa [61],
  - $\mu = 0.342$ [-] [61],
  - $\rho = 4430 \frac{\text{kg}}{\text{m}^3}$ [61],
  - σ_y = 880 MPa [61],
  - $\alpha = 8.6^{-05}$ 1/C° [61].

- **Technical ceramics Silicon carbide**: Typical values for silicon carbide are as follows:
  - $E = 450$ GPa [58],
  - $\mu = 0.14$ [-] [58],
  - $\rho = 3210 \frac{\text{kg}}{\text{m}^3}$ [58],
  - σ_y = 400 MPa [58],
  - $\alpha = 4E^{-05}$ 1/C° [58].

The following table provides a summary of the main parameters of the materials used for the simulations.

	E [GPa]	μ [-]	ρ [$\frac{\text{kg}}{\text{m}^3}$]	σ_y [MPa]	α [1/C°]
CFRE	150	0.28	1600	1100	4×10^{-05}
Aluminium	71.7	0.33	2830	469	2.304×10^{-05}
Titanium	113.8	0.342	4430	880	8.6×10^{-05}
Silicon Carbide	450	0.14	3210	400	4×10^{-05}

Table 5.1: Summary of the key parameter values for each material that will be used in the simulations, namely: Young's modulus **E** [GPa], Poisson's coefficient μ [-], density ρ [$\frac{\text{kg}}{\text{m}^3}$], Yield tensile strength σ_y and CTE α [1/C°].

It is important to note that, at a later stage, a more detailed selection of the material should be made, taking into account the additional requirements and criteria.

In section 5.2, these four materials will all be tested in a first resistance analysis to determine which of them will be selected for the simulation presented in the study.

5.2. First iteration on homogeneous structure

A static study on a homogeneous model of the structure, i.e. made up of a single large platform is used for the simplified simulation. This will enable choosing a material and making a first estimation of the thickness of the platform, and consequently the thickness of the sixty panels composing in reality this platform.

5.2.1. Context

Dimensions

In the sections before, it has been set that a significant limitation in this research project is the size requirement imposed by Ariane 6's fairing. To recap, the fairing has a width of 5 meters and a height of 17 meters. Due to these dimensions, a deployable system has been chosen in order to increase the maximal baseline b of the nulling interferometer and thus decrease the angular resolution θ which will allow the interferometer to resolve finer details and to distinguish between objects that are closer together in space. This choice was made to ensure that the equipment or payload being transported could fit within the fairing during the launch and then be deployed once the rocket is in space. The deployable system allows for efficient utilisation of the available space, enabling the successful execution of the mission.

The Fig. 5.1 depicts a cross-section of the studied system in its folded state. A specific colour is selected for each component of the system. The yellow rectangle represents the cross-section of the base of the structure, onto which the mechanical arms will attach, and it's also where the driving force will be applied. Its dimension is $l_{\textbf{base}} \times l_{\textbf{base}} \times e_{\text{base}}$ [mm]. The two turquoise squares represent two of the telescopes (in a rectangular configuration). Their dimensions have been set at $l_{\text{tel}} \times l_{\text{tel}} \times l_{\text{tel}}$ [mm]. The pink parts represent the mechanical arms, each having two rotational joints (one at the top and the other halfway down). Their dimensions are not known at this stage of the study but the maximum height that they can achieve in the folded state is about 15000 [mm]. Finally, the red portions depict the 15 layers of square panels, each overlapping the other, when the system is in its folded state. At this stage the dimensions of these panels are $l_{\textbf{base}} \times l_{\textbf{base}} \times e_{\text{pan}}$.

A simple equation then links the thickness of the panels to the width of the base:

$$L_{\text{tot folded}} = l_{\text{base}} + 30 \times e_{\text{pan}} + 2 \times l_{\text{tel}}, \tag{5.1}$$

where $L_{\text{tot folded}} = 5000$ mm and $l_{\text{tel}} = 1000$ mm.

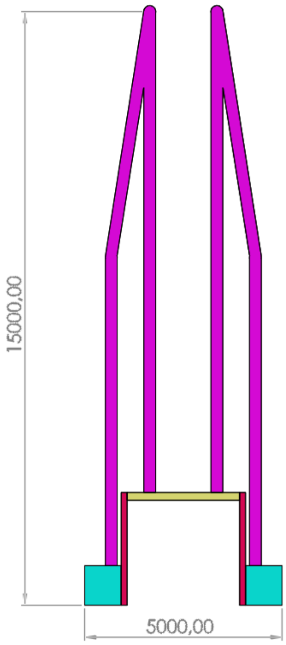

Figure 5.1: Cross-section of the structure in its folded state. yellow rectangle represents the cross-section of the base of the structure $l_{\mathbf{base}} \times l_{\mathbf{base}} \times e_{\text{base}}$ [mm], The two turquoise squares represent two of the telescopes $1000 \times 1000 \times 1000$ [mm], The pink parts represent the mechanical arms and red portions depict the 15 layers of square panels $l_{\mathbf{base}} \times l_{\mathbf{base}} \times e_{\text{pan}}$. This scheme has been realised with the software **SolidWorks**.

Fig. 5.2 illustrates the system's pattern (only the panels and the base are shown here) in its deployed state, as viewed from the top. The overall width of the system is directly proportional to the width of the base and, consequently, to the width of each panel.

$$L_{\text{tot}} = 7 \times l_{\text{pan}} = 7 \times l_{\text{base}} \tag{5.2}$$

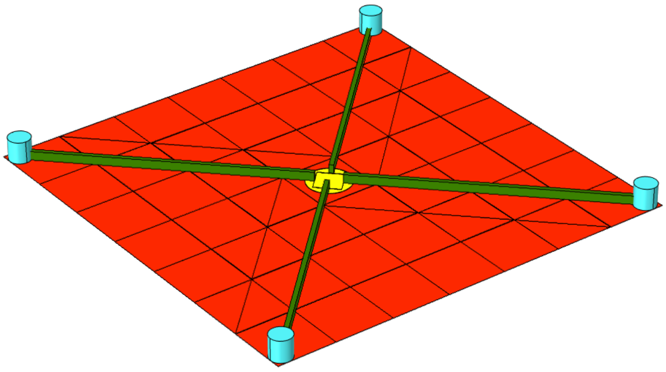

Figure 5.2: Realistic model: The turquoise cylinders represent the telescopes, the green beam represents the four mechanical arms, the yellow panel represents the base of the structure and the large homogeneous red panel represents all the panels in the ideal case where they would form a single perfectly homogeneous piece. The total length of on side of the structure L_{tot} is equal to seven times the length of the side of one panel or the square base, i.e. l_{base}. This scheme has been realised with the software **SolidWorks**.

Eq.5.2 represents the second equation that allows us to obtain the dimensions of the panels to start our study. Indeed, the first step of the study will be to analyse the behaviour of this system in a homogeneous form, meaning that there will not be 60 panels composing the structure as shown in Fig.5.2, but only a single one as depicted in Fig. 5.3. This homogeneous panel will initially have a thickness of 1 mm. Its deformation behaviour will then be observed when subjected to a uniformly distributed static load representing the acceleration that the entire system will experience once in orbit. The thickness of this homogeneous panel will increase to meet the precision criterion imposed in this project: achieving a maximum misalignment error of 30 arcsec.

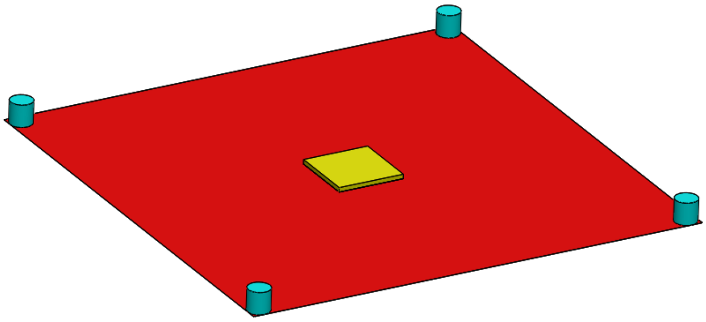

Figure 5.3: Simplified model: The turquoise cylinders represent the telescopes, the yellow panel represents the base of the structure and the large homogeneous red panel represents all the panels in the ideal case where they would form a single perfectly homogeneous piece. The total length of on side of the structure L_{tot} is equal to seven times the length of the side of one panel or the square base, i.e. l_{base}. This scheme has been realised with the software **SolidWorks**.

The initial dimensions are the following ones:

$$l_{\text{base}} = L_{\text{tot folded}} - 30 \times e_{\text{pan}} - 2 \times l_{\text{tel}} = 5 - 0.03 - 2 = 2.97 \text{ m} \tag{5.3}$$

$$L_{\text{tot}} = 7 \times l_{\text{base}} = 20.79 \text{ m} \tag{5.4}$$

These dimension leads to a maximum baseline between the centre of two telescopes described by Eq. 5.5.

$$b_{\text{max}} = \sqrt{2} \times (L_{\text{tot}} - 2 \times l_{\text{tel}}) = \sqrt{2} \times (20.79 - 1) = 27.99 \text{ m}. \tag{5.5}$$

For this preliminary design, the choice to limit the square to a 7×7 square panels has been made. Smaller origami flasher pattern could have been 3×3 or 5×5 square panels large. This is thus the third dimension reachable with this origami pattern.

With a 7×7 square panels large origami, the baseline achieved will length 27.99 m as stated in Eq. 5.5. This is already an improvement of 86.6% compared to the baseline minimum requirement, i.e. 15 m:

$$\frac{b_{\text{max}}}{b_{\textbf{requirement}}} = \frac{27.99}{15} = 1.866. \tag{5.6}$$

It is important to note that the chosen configuration could be extended to a 9×9 or even higher in a future design. This will depend on the future requirements, and if the baseline needs to be even more increased.

Static load

As explained just before, the system will undergo a uniformly distributed static load across the entire structure. This static load corresponds to the acceleration experienced by the structure once it is in orbit. The chosen orbit for this mission is the Lagrange Point 2 is one of the five Lagrange points in the Sun-Earth system, and it lies on the line connecting the centres of the Earth and the Sun, but beyond the Earth's orbit, Fig. 5.4.

On Lagrange L2 point, the gravitational attraction from the Sun and the Earth precisely equals the centripetal force required for a small object to move with them. Location on L2 is perfect for astronomy. Indeed, the communication with Earth is easy, the satellite is always oriented toward deep space which is an advantage for space application, and there is no large variation in temperature due to the L2 orbit characteristics [63].

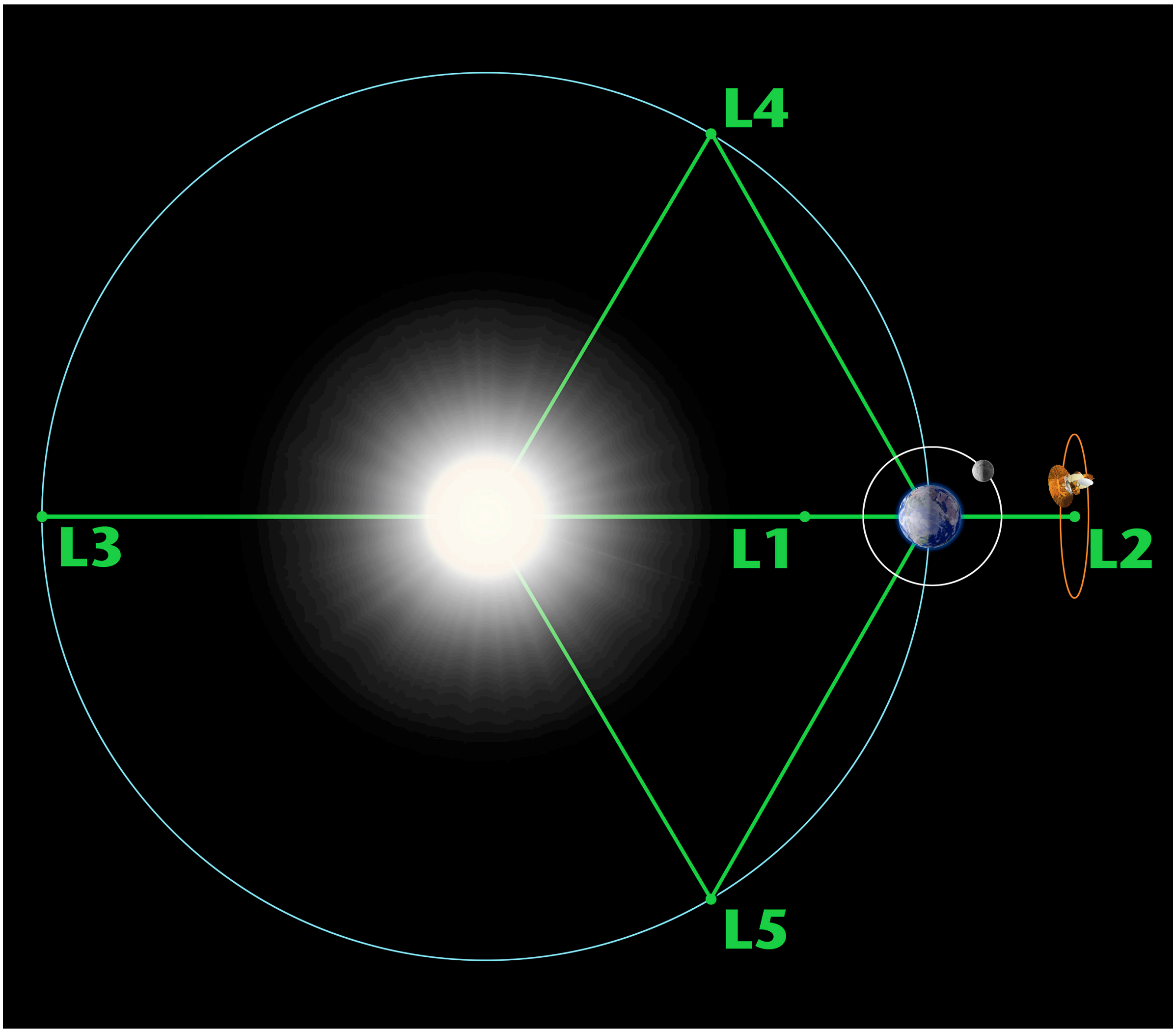

Figure 5.4: Lagrange point L2 [64].

L2 is particularly advantageous for observing exoplanets for several reasons:

- **Unobstructed View**: At the L2 point, telescopes and observatories have an unobstructed view of the deep space. This is crucial for detecting exoplanets as it allows for continuous and uninterrupted observations without interference from the Earth or the Moon [65].
- **Constant Sunlight**: Objects at the L2 point are in a continuous state of sunlight, providing a stable and well-lit environment for telescopes and instruments. Unlike satellites orbiting the Earth, which experience alternating periods of darkness and sunlight during their orbits, the L2 point offers a consistent source of light for observations [65].
- **Cooler Environment**: The L2 point is relatively cool compared to other locations closer to the Sun. This is important for infrared observations as cooler temperatures help reduce background noise and improve sensitivity in detecting faint signals from distant exoplanets [65].
- **Stability**: On L2, spacecraft or observatories placed there require minimal fuel for station-keeping. This allows for longer mission duration and more efficient use of resources [65].

The forces acting on a satellite in such an orbit depend on various external parameters, including potential collisions with debris/micrometeorites/..., the gravitational pull of certain celestial bodies, radiation, and so on. As a first step, it has been decided to only consider the maximum gravitational attraction from the Sun, the Moon, and the Earth which could be applied to the system. It is important to note that this is a significant simplification that will need further refinement, described in chapter 7.

The **MatLab** code, named acceleration.m (App. A.2), calculates the acceleration experienced by the satellite at the location in its L2 orbit, where it receives the strongest gravitational attraction from the three celestial bodies—namely, when the Sun, the Moon, and the Earth are closest to the satellite. At this specific point in the orbit, the satellite should be about 1.5×10^9 m from the Earth, $D_{\text{Earth}-\text{sat}} + D_{\text{Earth}-\text{Sun}} = 1.5 \times 10^9 + 147 \times 10^9 = 148.5 \times 10^9$ m from the Sun and about $D_{\text{Earth}-\text{sat}} - D_{\text{Earth}-\text{Moon}} = 1.5 \times 10^9 - 405696 \times 10^3 = 109.43 \times 10^9$ m from the Moon. Eq. 5.7 shows the gravitational field formulae that is used to obtain the gravitational acceleration.

$$a = G \times \frac{M}{D^2} \left[\frac{\mathrm{m}}{\mathrm{s}^2}\right], \tag{5.7}$$

where $G = 6.674 \times 10^{-11} \left[\frac{m^3}{kg\ s^2}\right]$ is the universal gravitational constant, M is the mass of the celestial body considered and D is the distance between the celestial body considered and the satellite. Eq 5.7 leads to a gravitational acceleration of a = 0.0062 $\frac{\mathrm{m}}{\mathrm{s}^2}$. It is a very small gravitational acceleration because of the large distance considered. This gravitational acceleration will be used as the main contributor to the static load, which will be uniformly distributed throughout the structure. However, in future works, additional external parameters will have to be added to the constraint applied on the structure.

Misalignment and deformation

The software **COMSOL Multiphysics** allows obtaining the deformation arrows of a structure subjected to a uniformly distributed static load, as shown in Fig. 5.5. These arrows can be used to visualise the deformation of the structure under this stress. It is then possible to export the magnitude values of these arrows along the x, y, and z axes. From there, it is possible to determine the normal vector coming from the new positioned surface of the telescopes and then to observe the misalignment achieved between the different telescopes. As a reminder, the objective here is to achieve a maximum misalignment of δ_{max} = 30 arcsec between the telescopes.

To do so, one has to take three deformation arrows starting from the initial top surface of one telescope. The deformation arrows allow to determine the new inclination of the telescope's top surface. The normal vector has just to be computed based on these three deformation arrows. Taking for instance, the normal vector coming from the new positioned telescope top surface $\mathbf{V_i}$, it comes:

$$\mathbf{V_i} \;=\; V_{x,\,i}\mathbf{x} + V_{y,\,i}\mathbf{y} + V_{z,\,i}\mathbf{z}, \tag{5.8}$$

where $\mathbf{V_i}$ represents the normal vector resulting from the telescope's top surface i, $V_{x,\,i}$, $V_{y,\,i}$ and $V_{z,\,i}$ represents the magnitudes respectively along the x, y and z axis and $\mathbf{x}$, $\mathbf{y}$ and $\mathbf{z}$ represent the reference frame.

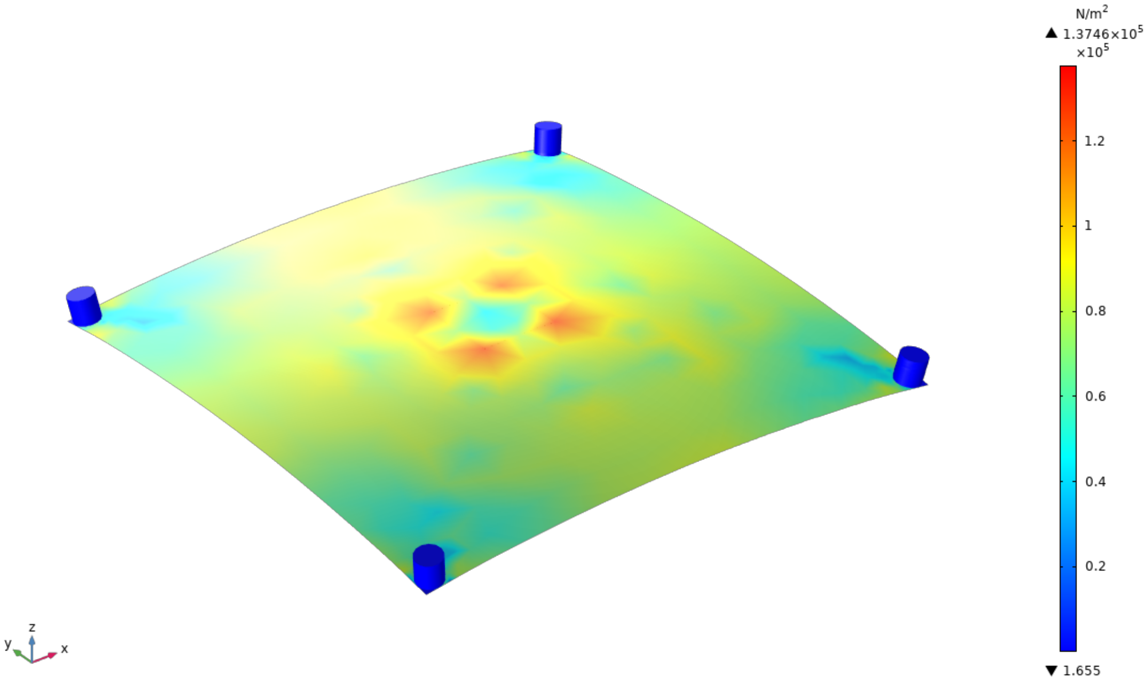

Figure 5.5: Von Mises constraints on the structure are illustrated with the colour pattern. The deformation arrows of the deployed system subjected to a uniformly distributed static load are also shown. This figure has been made with the software **COMSOL Multiphysics**.

On Fig. 5.5, one can observe that the arrows are pointing downwards. But the normal vector computed is pointing upward. Therefore, the misalignment will be calculated with respect to the **z**-vector $= \;(0,\;0,\;1)$.

Moreover, the angle between the two vectors can be determined using their dot product, which is given by:

$$\mathbf{V_i}.\mathbf{z} \;=\; |\mathbf{V_i}||\mathbf{z}|cos(\delta), \tag{5.9}$$

where $\mathbf{V_i}.\mathbf{z}$ is the scalar product of the two vectors, and $|\mathbf{V_i}||\mathbf{Z}| \;=\; \sqrt{V_{x,\,i}^2 + V_{y,\,i}^2 + V_{z,\,i}^2} \times$

$\sqrt{0^2+0^2+1^2} = \sqrt{V_{x,\,i}^2+V_{y,\,i}^2+V_{z,\,i}^2}$ is the product of the magnitudes of the two vectors and δ is the angle of inclination between them in radian.

The angle of misalignment is therefore first obtained in radians using the following equation:

$$\delta = acos\left(\frac{\mathbf{V_i}.\mathbf{Z}}{\sqrt{V_{x,\,i}^2+V_{y,\,i}^2+V_{z,\,i}^2}}\right) \tag{5.10}$$

Then multiply the result by $\frac{60\times60\times180}{\pi}$ to obtain the misalignment in seconds of arc. This misalignment is computed with report to the z-axis. Since the structure is perfectly symmetric, the maximum misalignment between the different telescopes will occur between two opposite telescopes. Thus δ_{max} is simply obtained by multiplying the previous results by a factor of 2.

All the arrows shown in Fig. 5.5 give an initial idea of the shape that the structure will take on its orbit at the moment when the attraction towards the Earth, Moon and Sun is the strongest. However, in the context of this project, the aim is to check whether the telescopes can all point in the same direction, despite potential deformations. It is therefore the arrows normal to the circular surfaces at the top of the cylinders (turquoise in Fig. 5.3) that need to be analysed. Fig. 5.6 shows the three deformation arrows that allow to obtain the normal vector of the new positioned telescope's top surface.

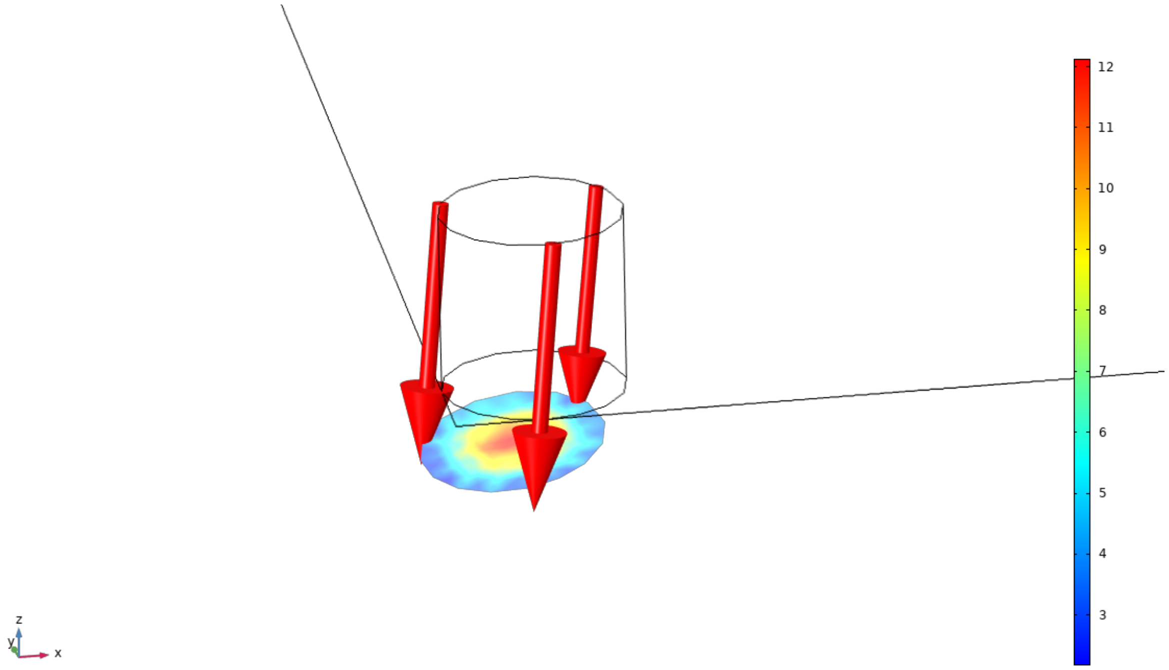

Figure 5.6: New orientation of the telescopes after being submitted to a uniformly distributed static load in **COMSOL Multiphysics**.

Additional assumptions

- **Mechanical arms**: As it can be seen in Fig. 5.3, the mechanical arms are not considered initially. Their impact on the stability will be taken into consideration later.

- **Square base**: The square base (yellow in Fig. 5.3) will have its foundation fixed to represent the fact that the satellite remains in orbit and cannot ”collapse” towards the Earth due to acceleration.
- **Telescopes**: The telescopes (turquoise cylinders in Fig. 5.3) must bear a certain load. Thus the material used to represent them is the fused silica ($\rho = 2200 \frac{\text{kg}}{\text{m}^3}$) which can be used to built mirror [66] [67]. It may not be the final material or density but it is still a good approximation. Moreover, the telescopes will be represented by a cylindrical volume with a height of 1 m and a diameter of 1 m.
- **Mesh definition**: The mesh used in **COMSOL Multiphysics** was in a first time set to the default one. The results of the simulations for this mesh were slightly distorted at the telescope level. In fact, the deformation arrows obtained at the telescopes all had completely different misalignments from the Z axis. This was due to the fact that **COMSOL Multiphysics**’s default mesh was not symmetrical and therefore the mesh on the cylinders was not the correct one. A more sophisticated mesh was therefore chosen, with 4 identical meshes on the telescopes and one large mesh on the homogeneous plate. The four meshes of the telescopes are much more refined than the large mesh of the homogeneous panel as it is shown in Fig. 5.7.

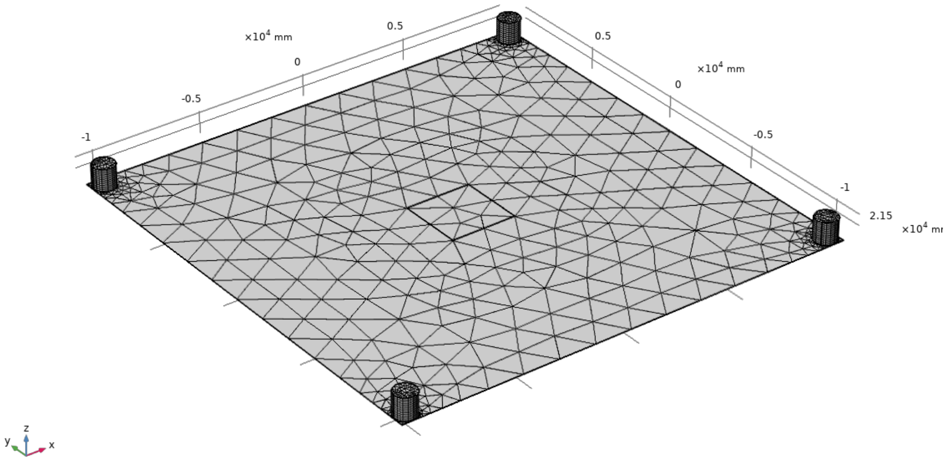

Figure 5.7: Mesh used in **COMSOL Multiphysics** for simulation under a static load.

5.2.2. Material selection

In section 5.1, four different materials were considered. To recap, the following materials and their corresponding properties will be tested:

	E [GPa]	μ [-]	ρ [$\frac{\text{kg}}{\text{m}^3}$]	σ_y [MPa]	α [1/C°]
CFRE	150	0.28	1600	1100	4×10^{-05}
Aluminium	71.7	0.33	2830	469	2.304×10^{-05}
Titanium	113.8	0.342	4430	880	8.6×10^{-05}
Silicon Carbide	450	0.14	3210	400	4×10^{-05}

Table 5.2: Summary of the key parameter values for each material that will be used in the simulations, namely: Young's modulus **E** [GPa], Poisson's coefficient μ [-], density ρ [$\frac{\text{kg}}{\text{m}^3}$], Yield tensile strength σ_y and CTE α [1/C°].

Results

The following figures illustrate the various deformations experienced by the system when subject to a uniformly distributed static load, representing the acceleration experienced on Lagrange L2 orbit.

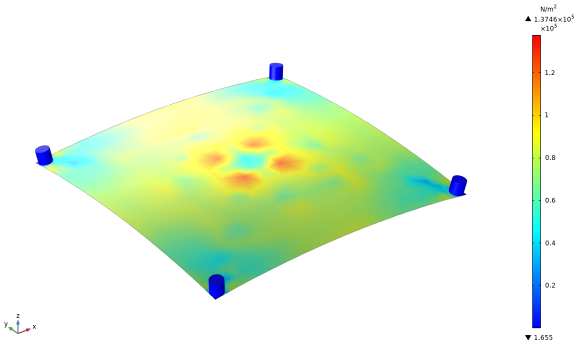

Figure 5.8: Carbon epoxy deformation. This scheme has been realised with the software **COMSOL Multiphysics**.

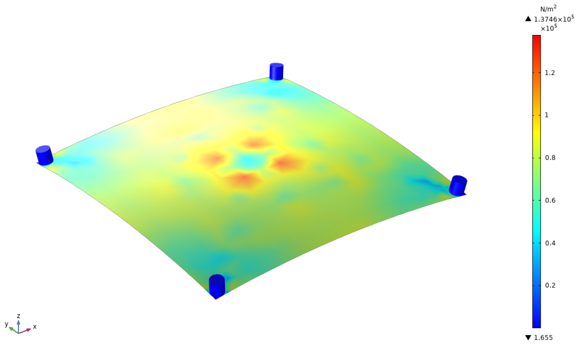

Figure 5.9: Aluminium deformation. This scheme has been realised with the software **COMSOL Multiphysics**.

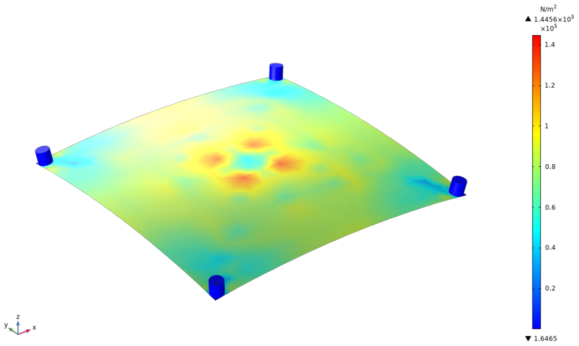

Figure 5.10: Titanium deformation. This scheme has been realised with the software **COMSOL Multiphysics**.

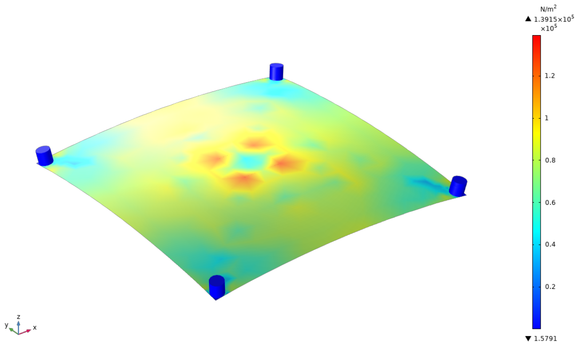

Figure 5.11: Silicon Carbide deformation. This scheme has been realised with the software **COMSOL Multiphysics**.

By simply looking at these figures, it is difficult to get a first impression on which material gives the least deformation to the structure. Indeed, all the figures appear to deform approximately in a same way when subjected to the same static force applied to the same model. Moreover, it is clearly shown that the maximum constraints are above the four edges of the square base of the structure. These locations will thus need to be reinforced.

The first step is to check if the yield tensile strength is not reached or exceeded for the various materials. The maximum values of the Von Mises constraints are thus compared to σ_y for all the material in Tab. 5.3.

	σ_{VM} [MPa]	σ_y [MPa]
CFRE	0.13201	1100
Aluminium	0.13746	469
Titanium	0.14456	880
Silicon Carbide	0.13915	400

Table 5.3: Maximum Von Mises stress σ_{VM} [MPa] compared to Yield tensile strength σ_y [MPa] for the different materials that are considered.

The results show clearly that with such a small acceleration and so such a very small force applied on the whole structure, the yield limit is really far to be reached.

A closer look at the magnitudes of the deformation arrows at the telescopes' top surfaces has to be taken to really determine which material will be least likely to provide misalignments between the telescopes. Indeed, what stands out most in these figures is the magnitude of the arrows along **z**, since those along **x** and **y** are weaker. However, it is these last two components that need to be most closely followed, since they are the ones that will cause telescopes to shift away from pointing in the direction of the **z**-vector.

By implementing the methods described in Eq. 5.8, 5.9, and 5.10 into the **MatLab** code named deformation_mat.m (App. A.3), it is possible to determine the maximum misalignment between the telescopes based on each material. The obtained results are provided in Tab. 5.4.

	$\delta_{\max}$ [arcsec]
CFRE	5.82
Aluminium	12.88
Titanium	8.38
Silicon Carbide	1.77

Table 5.4: Maximum misalignment $\delta_{\max}$ [arcsec] as a function of each material.

The values obtained are very small which is something predictable since the model considered is very simple and made almost in a single piece. Moreover, the gravitational acceleration felt in the L2 orbit is relatively low because of its long distance from the Earth, Sun and Moon.

All materials give way smaller misalignment between the telescopes than the requirement of 30 arcsec. Regarding Tab. 5.2, one can see that silicon carbide has the smallest misalignment among these four materials. However, it is well-known that in the context of a spatial mission the weight needs to be taken into consideration when choosing the material. It is for this reason that for the remainder of this study, carbon fiber reinforced epoxy, that has the smaller density combined with very good thermal and mechanical properties, will be used as the primary material for the structure.

5.2.3. Dimensional optimisation

As this model is very simplified, it only gives a first idea of the deformations. The values obtained for the misalignment in Tab. 5.4 are somewhat distorted. Indeed, they are way below reality. However, before starting the analysis of a more realistic model than this one, it is interesting to analyse the effect that the thickness of the large platform will have on the misalignment. Considering the use of CFRE (carbon fibre reinforced epoxy) as the main material composing the structure, it becomes thus feasible to mitigate the misalignment of the telescopes by adjusting the thickness of the large platform. This adjustment needs to be carried out in an iterative manner, gradually increasing the thickness until the minimum misalignment possible is achieved between all telescopes. The dimensions of the structure, as explained in Section 5.2, are taken into account in determining the varying dimensions. Indeed, increasing the thickness e_{pan} leads to decrease also the total length of the deployed structure L_{tot} and the length of the square base l_{base}.

Tables available at Fig. 5.12 display the key dimensions, namely e_{pan}, L_{tot} and l_{base}, measured in meters, that will be employed in this iterative process. Note that these values are all obtained from the **MatLab** code called dim_evo.m available at App. A.4. Each of these pairs of values corresponds to a thickness starting at 1 mm and increasing by 1 mm for each new pair of dimensions until the final thickness of 50 mm is reached.

$\mathbf{e}_{\text{pan}}$ [mm]	$\mathbf{L}_{\text{tot}}$ [m]	$\mathbf{l}_{\text{base}}$ [m]
1	20.79	2.97
2	20.58	2.94
3	20.37	2.91
4	20.16	2.88
5	19.95	2.85
6	19.74	2.82
7	19.53	2.79
8	19.32	2.76
9	19.11	2.73
10	18.90	2.70
11	18.69	2.67
12	18.48	2.64
13	18.27	2.61

$\mathbf{e}_{\text{pan}}$ [mm]	$\mathbf{L}_{\text{tot}}$ [m]	$\mathbf{l}_{\text{base}}$ [m]
14	18.06	2.58
15	17.85	2.55
16	17.64	2.52
17	17.43	2.49
18	17.22	2.46
19	17.01	2.43
20	16.80	2.40
21	16.59	2.37
22	16.38	2.34
23	16.17	2.31
24	15.96	2.28
25	15.75	2.25
26	15.54	2.22

$\mathbf{e}_{\text{pan}}$ [mm]	$\mathbf{L}_{\text{tot}}$ [m]	$\mathbf{l}_{\text{base}}$ [m]
27	15.33	2.19
28	15.12	2.16
29	14.91	2.13
30	14.70	2.10
31	14.49	2.07
32	14.28	2.04
33	14.07	2.01
34	13.86	1.98
35	13.65	1.95
36	13.44	1.92
37	13.23	1.89
38	13.02	1.86
39	12.81	1.83
40	12.60	1.80
41	12.39	1.77
42	12.18	1.74
43	11.97	1.71
44	11.76	1.68
45	11.55	1.65
46	11.34	1.62
47	11.13	1.59
48	10.92	1.56
49	10.71	1.53
50	10.50	1.50
-	-	-
-	-	-

Figure 5.12: 50 pairs of L_{tot} and l_{base} decreasing with increasing thickness e_{pan} provided in [m] with the **MatLab** code di_evo.m available in App. A.4.

The reason for stopping the increase of the thickness of the large platform at a certain value, i.e. L_{tot} = 10.50 m, l_{base} 1.50 m and e_{pan} = 50 mm, is that when taking the largest baseline between two telescopes one then looks at the length of the diagonal of the square structure, Fig. 5.13. This must not be less than 15 m - the height of the Ariane 6 fairing - otherwise there would be no point in using a deployable structure. Indeed, if the baseline is less than 15 m, it would be wiser to opt for an ultra-stable one-piece structure with a baseline equal to the height of the Ariane 6 fairing, and which would obviously provide greater stability than a deployable system and less risk of errors, damage, and so on. The minimal dimensions considered leads thus to a maximum baseline of approximately 14.89 m which is just below considerable available height of Ariane 6 fairing.

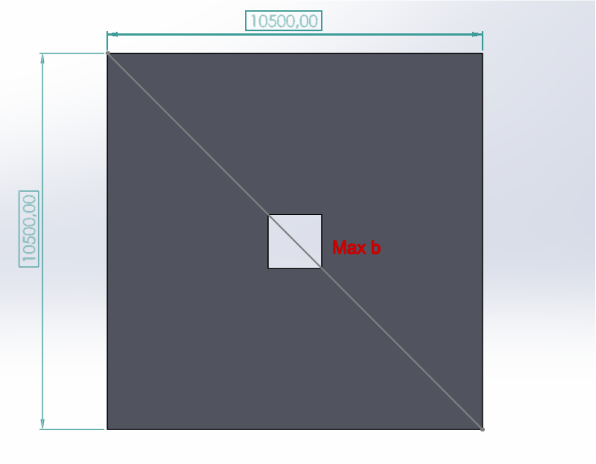

Figure 5.13: Dimension of the maximal baseline length for L_{tot} = 10500 mm, l_{base} 1500 mm and e_{pan} = 50 mm. Max b denotes the grey diagonal line in the figure. This scheme has been realised with the software **SolidWorks**.

As the thickness of the homogeneous large panel increases, the degree of misalignment decreases.

5.2.4. Iteration process

Fig. 5.14 shows the evolution of the maximum misalignment between the telescopes as a function of the progressive increase in the thickness of the large homogeneous panel for a simplified model with CFRE as material for the large platform and the square base and with fused silica for the telescopes.

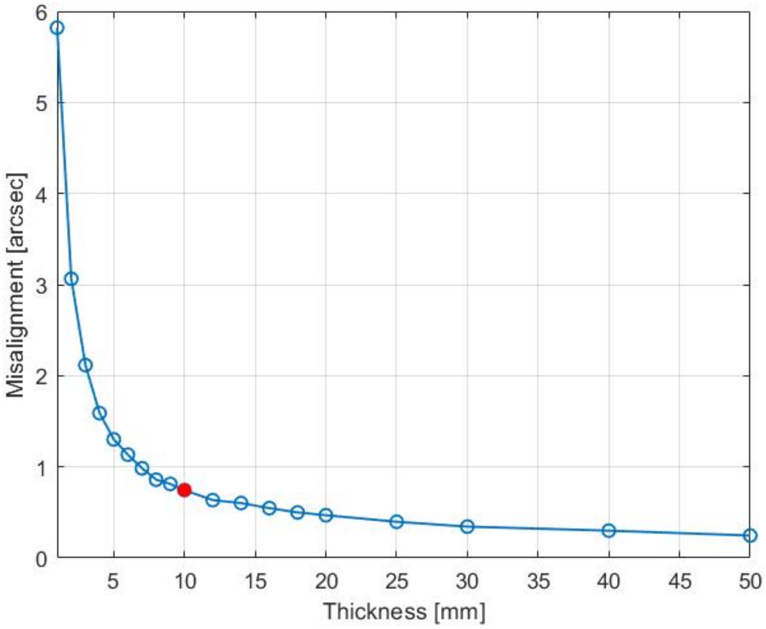

Figure 5.14: Evolution of the maximum misalignment between the telescopes as a function of the progressive increase in the thickness of the large homogeneous panel. This graph has been made with the**MatLab** code iterative.m available in App. A.5.

It clearly shows that from around 10 mm thickness (red dot in Fig. 5.14), telescope misalignment starts to decrease much less rapidly. This convergence corresponds to the following dimensions: L_{tot} = 18.27 m and l_{base} = 2.61 m. This means that at this point, the decrease of misalignment converges to the value of roughly 0.2 arcsec that is computed for the following structure dimensions: L_{tot} = 10.50 m, l_{base} = 1.50 m and e_{pan} = 50 mm. A zoom on Fig. 5.14 reveals this slope evolution in greater detail:

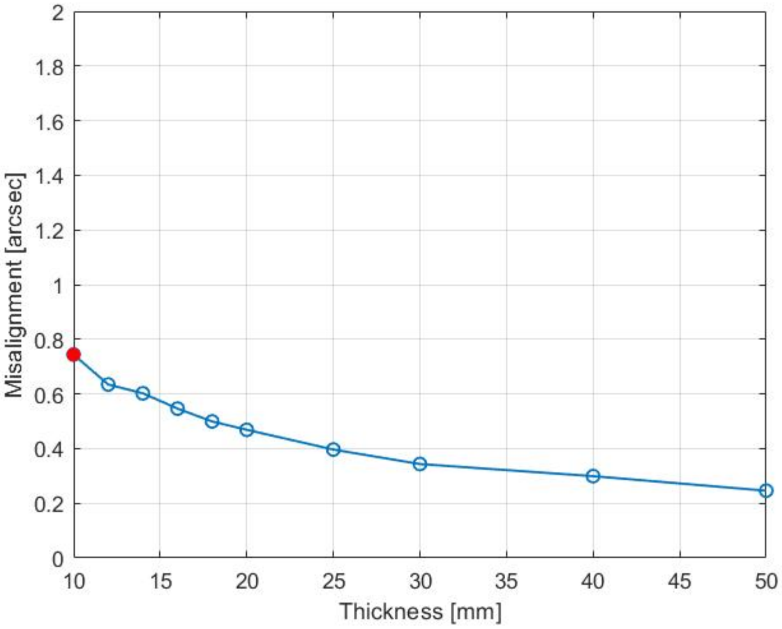

Figure 5.15: Zoom of the evolution of the maximum telescope misalignment values with respect to the axis **z** as a function of the progressive increase of the thickness of the large platform. This graph has been made with the **MatLab** code iterative.m available in App. A.5.

Since the value of the misalignment between the telescopes for the e_{pan} = 10 mm is way bellow the requirement of 30 arcsec, the decision to continue the study with the value of e_{pan} = 10 mm has been made. This should bring a good compromise taking into consideration the weight and the maximisation of the baseline length.

In the next section, a check of he consistency of this choice will be made. Tab. 5.5 shows the dimensions corresponding to this thickness and the misalignment obtained for it.

$\mathbf{L}_{\text{tot}}$ [m]	$\mathbf{l}_{\text{base}}$ [m]	$\mathbf{e}_{\text{pan}}$ [mm]	δ_{max} [arcsec]
18.90	2.70	10	0.7440

Table 5.5: Main dimensions of the structure and its misalignment obtained for an homogeneous panel model.

5.2.5. Dimensions results

A more realistic model must now be produced, taking into account the actual division of the large platform into 60 smaller panels and the mechanical arms that will add additional stiffness. The rest of this chapter will be focus on a structure with the dimensions given in Tab 5.5. Fig. 5.16 depicted the most realistic models that is used in this section.

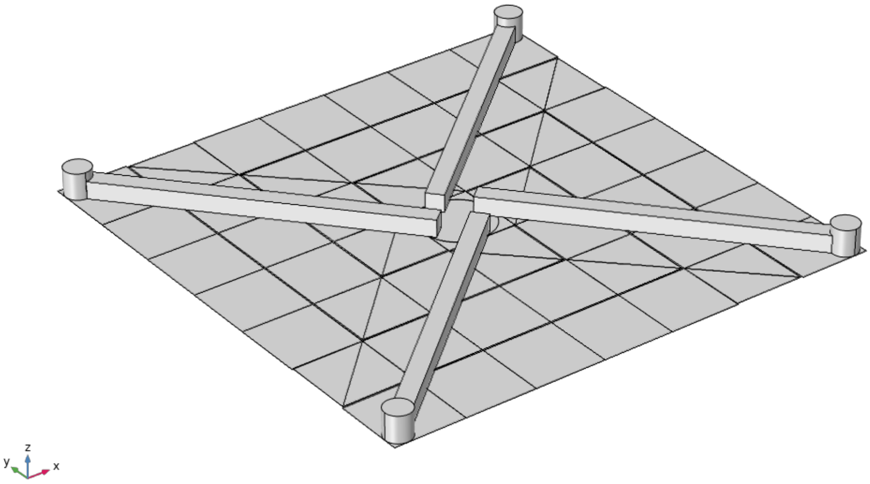

Figure 5.16: L_{tot} = 18.900 m, l_{base} = 2.70 m and e_{pan} = 10 mm.

5.3. Influence of platform division into panels

In this section, the large homogeneous platform is no more considered but instead, 60 panels constituting this platform in reality will be used. The 60 panels are organised in four spiral arms as the one depicted in Fig. 5.17.

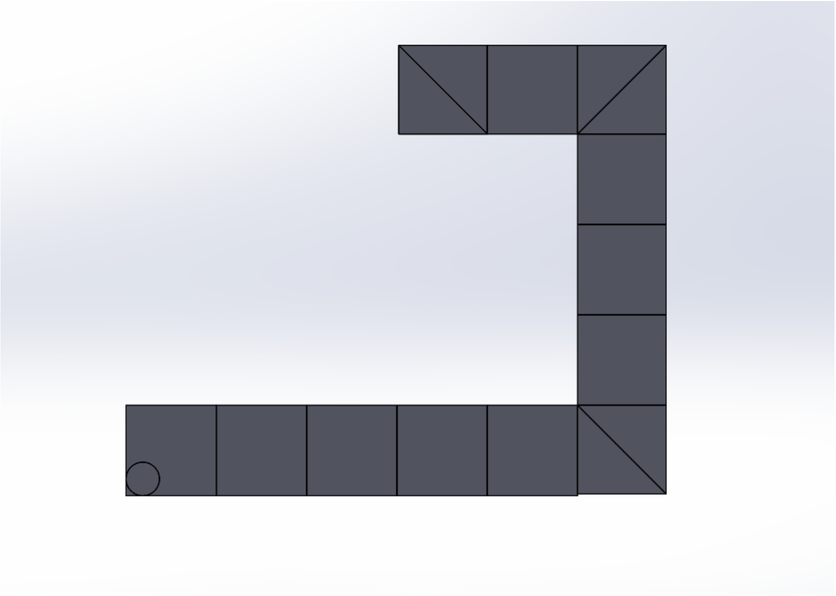

Figure 5.17: One spiral arm of the total origami structure for the following dimensions: L_{tot} = 18.900 m, l_{base} = 2.70 m and e_{pan} = 10 mm.

All the panels composing one spiral arm are linked by a rotational hinge that will be discussed in more details in chapter 6 and chapter 7. Between these spiral arms, a lockable system must be used to fix the different spiral arms once deployed.

Since it is a consequent assumption that will definitively leads to very higher misalignments and deformations for the structure, an additional simulation considering only the origami flasher part with the 60 panels connected only in the spiral arms part need to be study under a static load. At this stage, it will be assumed that the spirals are not linked directly to each other. This assumption is quite conservative as in a future design a system to connect automatically the the spiral arm when deployed could be designed. The assumption made will definitively lead to higher misalignments and deformations for the structure.

The following figures show the model considered for this section for the structure dimensions proposed in Tab. 5.5. One can see that due to the gap between the spiral arms, the structure is way more deformed than for the simplified model. The numerical results will help to better understand all the displacement and the real impact of this division of the structure. The largest magnitude for the deformation arrows $disp_{\text{max}}$ and the maximum misalignment between the telescopes are shown at Tab. 5.6.

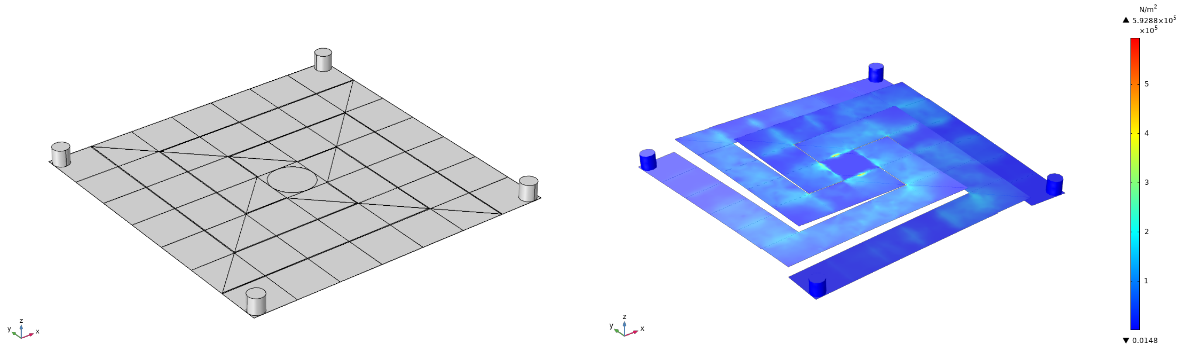

(a) Model of the origami system.

(b) Deformation of the origami system.

Figure 5.18: L_{tot} = 18.90 m, l_{base} = 2.70 m and e_{pan} = 10 mm.

	δ_{max} [arcsec]	**disp**$_{\text{max}}$ [mm]
Model	37.7467	0.0788

Table 5.6: Maximum misalignment between the telescopes for the origami system and maximum displacement magnitude of the deformation arrows for the following structure dimensions L_{tot} = 18.90 m, l_{base} = 2.70 m and e_{pan} = 10 mm.

The misalignment values are larger than for the simplified model which is what was expected. Moreover, the required misalignment of 30 arcsec is no longer met. The addition of the mechanical arms that are supposed to drive the deployment, will also increase the stiffness of the structure after deployment. This could lead back to the target misalignment if well dimensioned. That is what will be checked in the next section.

To check this out, four mechanical arms will be added to the model and be tested in the same conditions than the previous steps, i.e. submitted to a gravitational acceleration of 0.0062 $\frac{m}{s^2}$ uniformly distributed all over the structure.

5.4. More realistic model

The first static study performed on a model made up of just one large homogeneous panel, the four telescopes and a central square base provided an initial estimate of the deformations and misalignment of the telescopes. Thanks to this, the material for the panels making up the main part of the system was first determined, then the main dimensions of the deployable system have been found. However, the assumption of a large homogeneous panel with no hinges or joints is highly simplistic and impractical. This is why an additional static study on the real origami system has been made. This second model showed that even with a division of the large homogeneous platform initially considered, the misalignment between the different telescopes was relatively small even if the requirement of 30 arcsec was not met anymore. The final step of this static simulation is thus to introduce in the model the four mechanical arms which will add stiffness to the structure, reinforce the sensitive parts of it and aim to drive the whole structure's components during the deployment. These mechanical arms are essential to link the different spiral arms to form a structure that can be assimilated to the homogeneous case in order the decrease even more the misalignment.

This is why in this section, a more realistic model than the ones considered in section 5.2 and 5.3 will be used, subjected to the same static load representative of the acceleration undergone in Lagrange L2 orbit, and analysed in order to obtain results closer to reality than those previously provided.

However, this final model is not yet perfectly realistic neither, and many more studies and analyses will be needed to obtain theoretical results as close as possible to reality. Indeed, the hinges between the panels, the hinges between the different components of each mechanical arms, and the system to link firmly the mechanical arms to the spiral arms were not included in this model. These studies and analyses are proposed and introduced in chapter 7. Therefore, many assumptions are still made for this more realistic case and are the following ones:

- The structure is considered in its fully deployed state.
- The mechanical arms are composed of just one body in the model, as the nodes making up these mechanical arms, see chapter 6, are assumed to be totally fixed in the deployed state of the system. Moreover, the mechanical arms are also assumed to be firmly fixed to the panels they overhang by means of a locking mechanism, which will be part of the propositions for future studies in chapter 7.
- The choice of material for the mechanical arms has been made with the same material that for the panels and for the same reasons (mechanical properties, thermal properties and weight).
- As for the simplified model, the mesh selection is achieved by separating the telescopes from the other components of the structure in order to obtain deformation results that are as similar as possible between the different telescopes. This mesh is shown in Fig. 5.19.

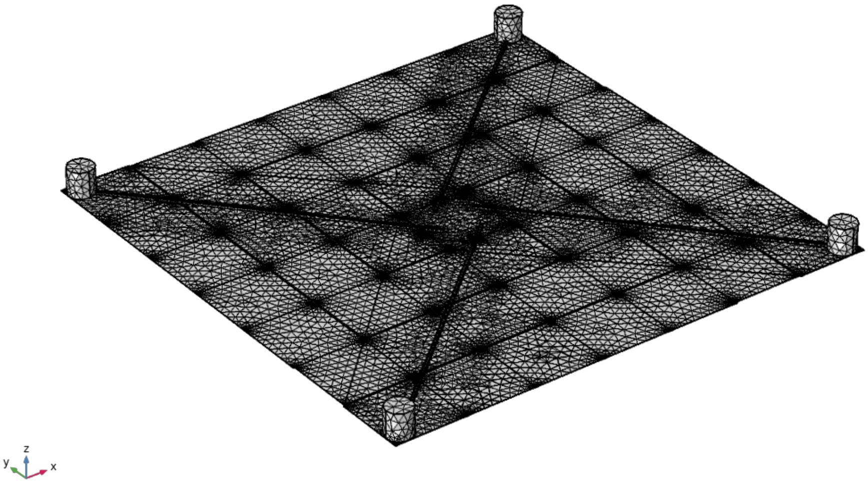

Figure 5.19: Mesh used for all the simulations carried out on the model.

5.4.1. Deformations

The model shown in Fig. 5.16 is therefore considered for the structure dimensions given in Tab. 5.5. The same process as in section 5.2 is carried out. The model created on the **SolidWorks** software is sent to the **COMSOL Multiphysics** software using the *Livelink* option from **COMSOL Multiphysics**. Subsequently, it is subject to the same static load, uniformly distributed throughout the system and corresponding to the acceleration experienced on the L2 Lagrange orbit. A first simulation is made with a solid section for the mechanical arms of 656.79×656.79 [mm] and the stress and deformations for this model are shown in Fig. 5.20.

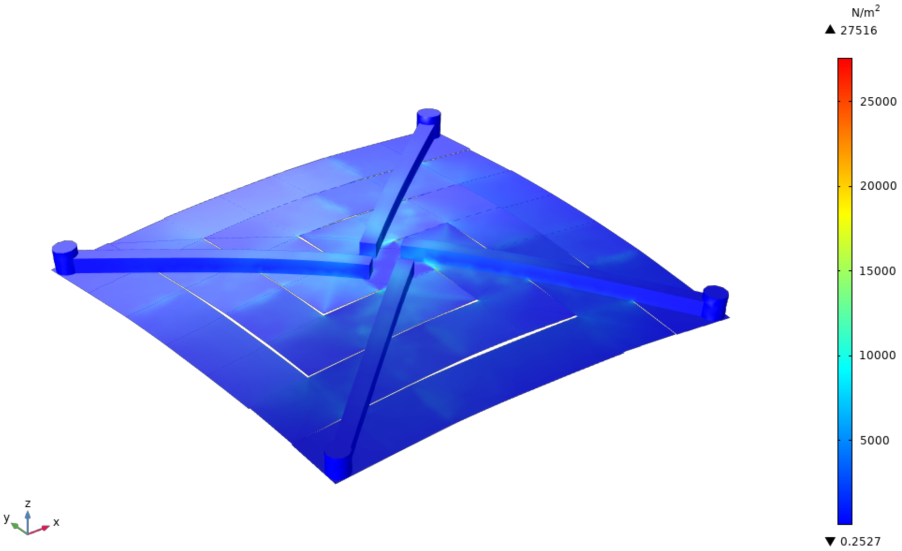

Figure 5.20: Deformation of the system for the structure dimensions: L_{tot} = 18.90 m, l_{base} = 2.70 m and e_{pan} = 10 mm.

Spatial deformations here no longer have entirely the same appearance as in the simplified model considered in section 5.2. Indeed, the addition of the division into panels and the addition of the mechanical arms lead to a slightly different deformation shape.

Thanks to the code **MatLab** real_misalignment.m available in App. A.6, it is possible to obtain the maximum misalignment between the telescopes and the maximum displacement magnitude of the deformation arrows for this model, available in Tab. 5.7.

	δ_{max} [arcsec]	$\textbf{disp}_{\text{max}}$ [mm]
Model	0.1580	0.0035

Table 5.7: Maximum misalignment between the telescopes the maximum displacement magnitude of the deformation arrows for the structure dimensions: L_{tot} = 18.90 m, l_{base} = 2.70 m and e_{pan} = 10 mm.

These results show immediately the usefulness to use the mechanical arms not only as drivers for the entire structure (see chapter 6), but also as stiffeners once the system is fully deployed. With the arms, not only the deformation is greatly reduced but also the Von Mises constraint concentrations that appeared with the simplified model at the centre of the structure.

A better look at the section of the arms needs to be done in order to reduce it while keeping the right misalignment.

5.4.2. Dimensions of the mechanical arms' cross-section

The reason why the first section of the arms was taken at 656.79×656.79 [mm] is that this is the maximum square section for the arms coming from the geometry of the origami flasher. Here under, the details about these dimensions is given before starting the optimisation and so the reduction of the section of the arm as this initial section is obviously too big and the mass linked the the arms very high.

It is important to note that the height and the width of the cross-section should respect some geometry constraints. Indeed, the square base of the whole structure is more complex in the more realistic case than for the homogeneous one. This is because on it, a rotational engine takes place. A top view of this more realistic square base is shown in Fig. 5.21a. In this figure, one can see different parts of this basis and their main dimensions. The large square part is the previously defined square base of length l_{base} (here 2700 mm). The circle represents the rotational platform that will be activated by the engine to turn on itself in order to deploy the structure. Its maximum radius is equal to $r_{\text{engine}} = l_{\text{base}} - 1$ [mm]. The reduction of 1 mm is there to create a cylindrical joint between the square base and the rotational engine. Then, the four external squares represent the four different telescopes (1000 × 1000 [mm]). Finally, the small rectangles on the outside each represent 15 panels folding on top of each other.

Fig. 5.21a depicted the top view of the folded state centre system. But looking closer to this scheme can leads to geometrical constraints on $h_{\text{arm, max}}$ and $w_{\text{arm, max}}$, shown in Fig. 5.21b right. In this last figure, the largest $h_{\text{arm, max}}$ and $w_{\text{arm, max}}$ are denoted by the two different following lengths: 1047.52 mm for $h_{\text{arm, max}}$ and 998 mm for $w_{\text{arm, max}}$. It is to note that if w_{arm} is set at its maximum value, i.e. 998 mm, h_{arm} will be set at 0 mm which is not possible. Thus the two values are evolving in an inversely proportional way while respecting the following constraints:

$$h_{\text{arm}} \in \,]0,\ h_{\text{arm, max}} \,(=\ 1047.52)[\text{ [mm]}, \tag{5.11}$$

$$w_{\text{arm max}} \in \,]0,\ h_{\text{arm, max}} \,(=\ 998)[\text{ [mm]}. \tag{5.12}$$

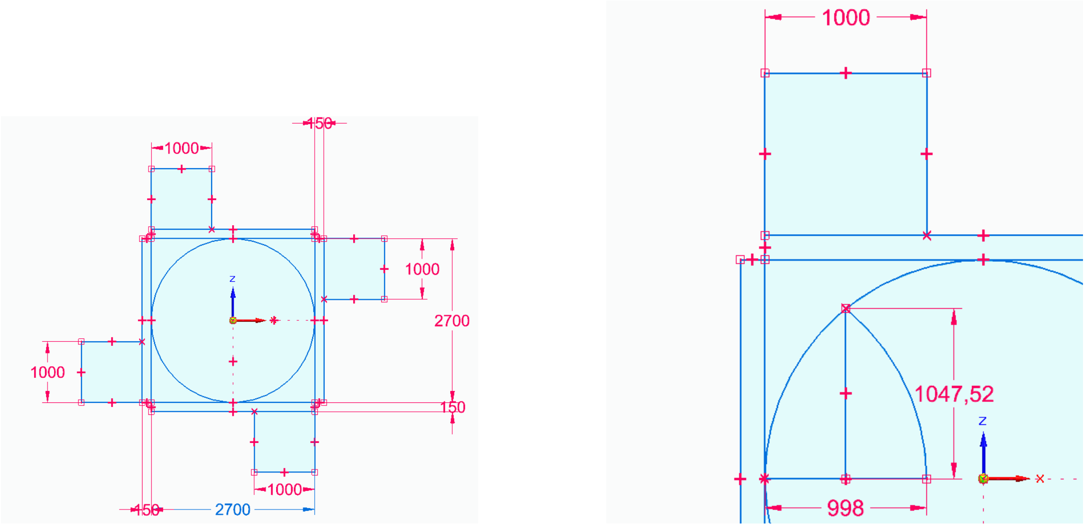

(a) Main dimensions of the square base of the structure in [mm].

(b) Cross-section dimensions in [mm].

Figure 5.21: These schemes have been realised with the software **SolidEdges**.

Fig. 5.22 shows the evolution of h_{arm} regarding the evolution of w_{arm} for the structure dimensions considered in this section. This figure has been realised with the **MatLab** code dim_evo_arm.m.

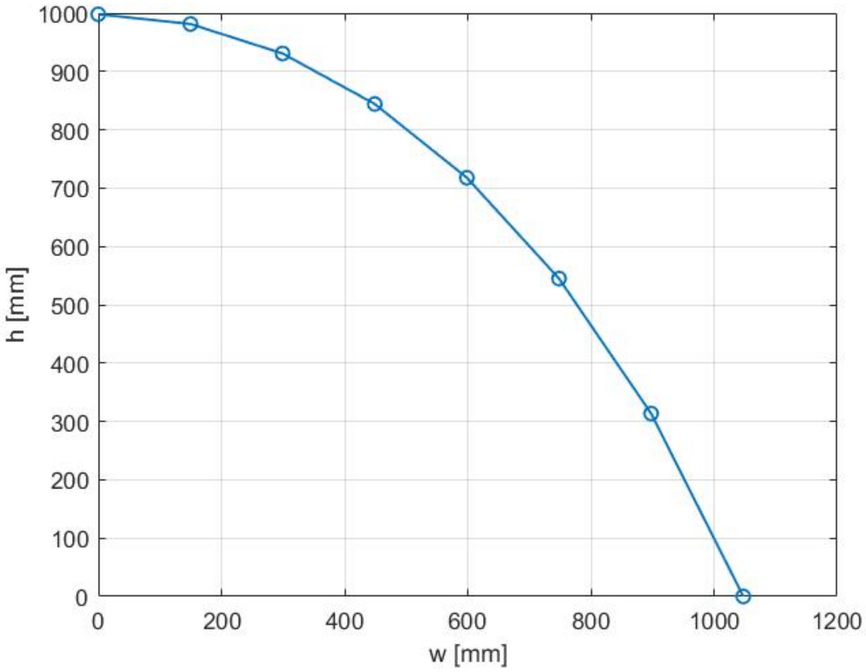

Figure 5.22: Variation of h_{arm} regarding the evolution of w_{arm} for the structure dimensions considered.

The dimensions of a rectangular beam cross-section are important in determining its rigidity, as they influence the distribution of stresses and strains in the beam under the effect of a uniformly distributed static load. The wider and higher the cross-section, the greater the resistance of the beam to bending and torsion [68][69].

5.4.3. Mechanical arms' cross-section selection

Fig. 5.20 and Tab. 5.7 give the deformation shape and values for mechanical arms with a cross-section of 656.79×656.79 [mm]. With this cross-section dimensions, the requirement of 30 arcsec is largely achieved. Knowing that in space application, the weight must be taken into consideration very carefully, especially for the launch phase, the cross section can be improved in order to reduce the weight. Indeed, the mechanical arms being set to be in CFRE of density $\rho = 1600\,\frac{\text{kg}}{\text{m}^3}$, the total mass of the four mechanical arms is equal to 32406 kg which is huge.

Thus, even if there is no requirement on the weight, this configuration is totally to be excluded. This is why hollow cross-section are considered. As well as reducing weight, the hollow cross-section could allow to transmit instruments or other items needed for the mission via a protected area. This type of cross-section is shown in Fig. 5.23.

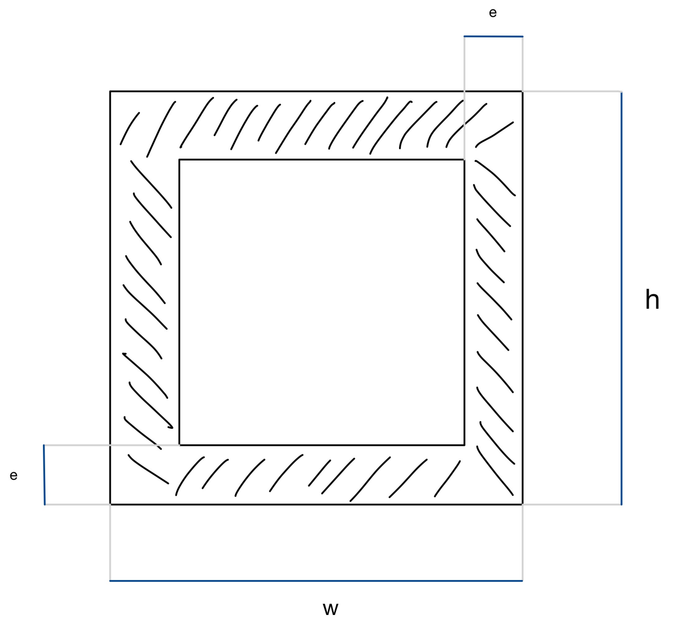

Figure 5.23: Dimension notation of a hollow cross-section. The dimension are considered in mm. This figure has been made by hand by Sacha Iannello

Tab. 5.8 gives the different cross-section dimensions of the mechanical arms that have been tested and the misalignment between the telescopes that they induce. In it, h_{arm} is the height in mm, w_{arm} is the width, and e_{arm} is the thickness of the cross-section.

$\mathbf{h}_{\text{arm}}$ [mm]	$\mathbf{w}_{\text{arm}}$ [mm]	$\mathbf{e}_{\text{arm}}$ [mm]	δ_{max} [arcsec]	**Mass** [kg]
656.79	656.79	0	0.1580	32406.13
656.79	656.79	10	0.1919	1943.56
656.79	328.395	10	0.2569	1450.16
328.395	328.95	10	0.3169	956.75
100	100	10	1.0033	270.44

Table 5.8: Different cross-section dimensions and corresponding misalignments and weights.

All the cross-section dimensions lead to small misalignment between the telescopes that are way below the requirement of 30 arcsec. The final dimension are thus made to optimise the weight while respecting the misalignment requirement. The 100×100 [mm] hollow cross-section with a thickness of 10 mm is thus selected. This value could be optimised in the future when more precise information on the requirements will be known.

5.4.4. Final design

All the main dimensions of the structure are known and given in Tab. 5.9. The final model considered is the one will be studied in a kinematic analysis is shown in Fig. 5.24. The deformations when submitted to the gravitational acceleration are shown in Fig. 5.25.

$\mathbf{e}_{\text{pan}}$ [mm]	$\mathbf{L}_{\text{tot}}$ [mm]	$\mathbf{l}_{\text{base}}$ [mm]	**b** [mm]
10	18900	2700	25314.42
$\mathbf{h}_{\text{arm}}$ [mm]	$\mathbf{w}_{\text{arm}}$ [mm]	$\mathbf{e}_{\text{arm}}$ [mm]	δ_{max} [arcsec]
100	100	10	1.0033

Table 5.9: Final main dimensions of the model.

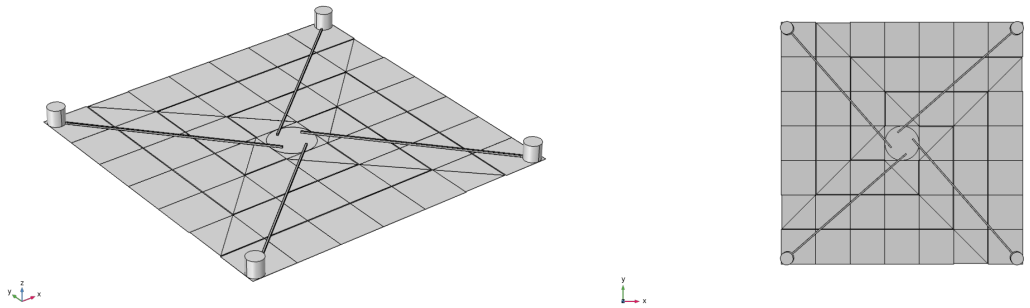

Figure 5.24: Final view of the system modelled.

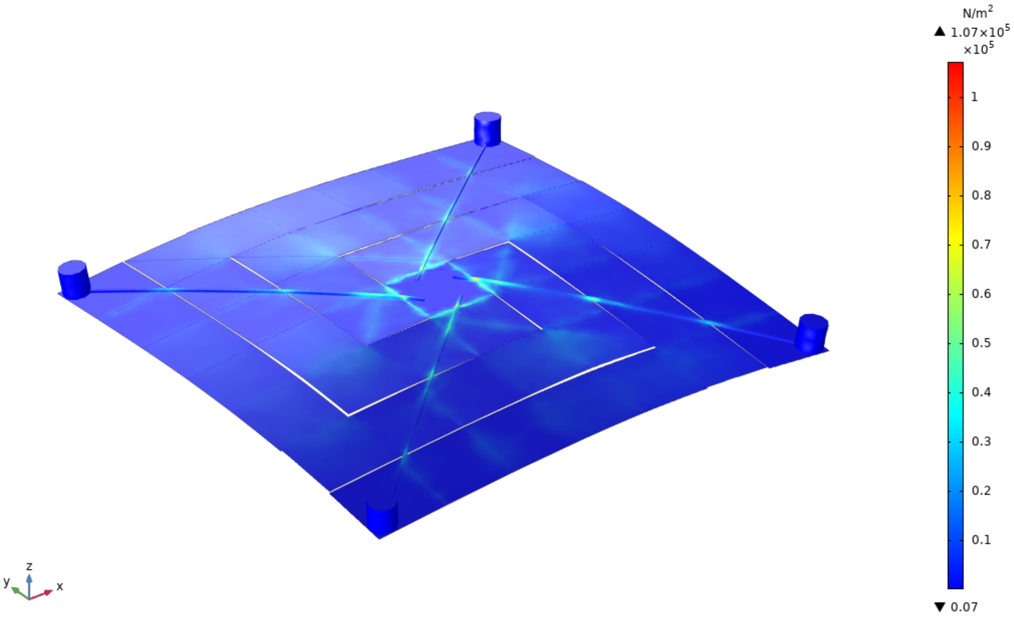

Figure 5.25: Von Mises stress and shape deformation of the final dimensioned system.

This chapter allowed to confirm that the conceptual design of the origami flasher reinforced was realistic and feasible for the specific requirements to be obtained. However, it goes without saying that an optimisation has to be done in a future design stage, when more details and other requirements will be set to determine the optimal dimensions of this system.

6

Kinematics Analysis

A kinematic analysis of a deployable system enables verification of whether the deployment under consideration is physically feasible. The aim of this chapter is therefore to determine whether a deployment of all the components of the system can take place without any collisions between different bodies or any deformation of certain elements.

To accomplish these tasks, the different parts of the system will be individually designed on the basis of the dimensions previously determined in chapter 4. The different parts of the system are the followings:

- **The four mechanical arms**: The purpose of the arms is to actuate the deployment but also to add stiffness to the structure once deployed. This is the part of the system that the engine will activate to deploy the entire structure.
- **The 60 square origami flasher panels**: They are either square or triangular. Their purpose is to support the telescopes and to make the structure as rigid as possible so that it can withstand external disturbances once deployed and in orbit.

Then, the two separate parts will be assembled together to obtain a system that is physically deployable, i.e. without collisions between the different bodies that make it up. All the models are produced on **SolidWorks** software, and the analyses are carried out on **COMSOL Multiphysics** software.

The initial and final configuration of the structure are shown in Fig. 6.1 and 6.2.

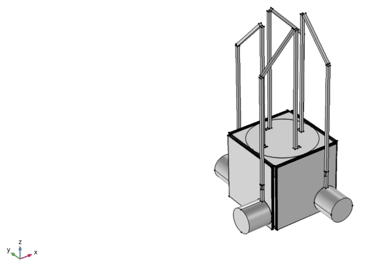

Figure 6.1: 3D of the folded state system at $t = 0$ [s].

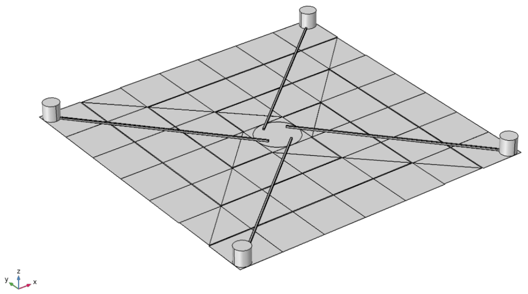

Figure 6.2: 3D of the deployed state system at $t = t_f$ [s].

6.1. Mechanical arms

The mechanical arms are an essential part of the deployment of the system studied in this research. Each of these four mechanical arms will guide one of the four telescopes and one of the spiral arms (Fig. 4.11). These must have three kinematic rotation joints, including one at the very base of the arms, to enable the telescope to be guided correctly while respecting its degrees of freedom. Each arm is therefore composed of three rigid bodies (RB), depicted in red in Fig. 6.3, and three kinematic rotation joints depicted with green dots.

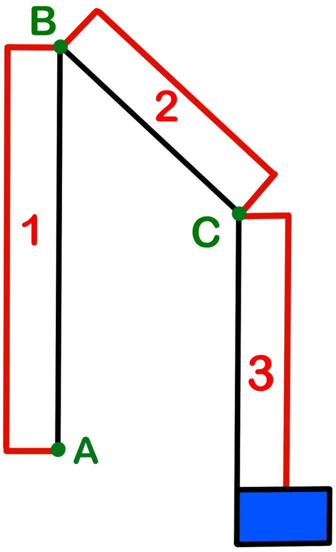

Figure 6.3: Single arm components denotation.

It is to note that a fourth RB arm (part of RB 3) will be used in order to let the last panel of the spiral arms having another degree of freedom of rotation. Indeed, during the deployment, if the last panel is not always horizontal, torsion will appear in the mechanical arms unless an additional degree of freedom is given to it to allow this panel to rotate in line with with the mechanical arms. This fourth RB will be called RB 4 and will take a part of the length of RB 3.

6.1.1. Conception

The dimensions of the different RB composing the mechanical arms are obtained while taking as assumption that the angles between RB 1 and 2 is equal to $\frac{\pi}{4}$ for simplicity. In addition, the cross-section of the mechanical arms is not a hollow section because the weight is not meant to be optimised for these simulations. Then simple trigonometry computations lead to the following values:

- $L_1 = 4869.44$ [mm],
- $L_2 = 1979.89$ [mm],
- $L_3 = 4579.43$ [mm],

- L_4 = 600 [mm]
- h_{arm} = 100 [mm],
- w_{arm} = 100 [mm],
- $\beta_1 = \frac{\pi}{2}$ [rad],
- $\beta_2 = \frac{3\pi}{4}$ [rad],
- $\beta_3 = \frac{\pi}{4}$ [rad],

where L_i is the length of the i-RB and β_i is the angle between two RB needed to align them (ex. RB 2 has to realise a rotation of $\frac{3\pi}{4}$ [rad] anti-clockwise around kinematic rotation joint B in order to align itself with RB 1 in Fig. 6.3). Moreover, since initially RB 3 and RB 4 are aligned, the hinge between them allow free rotation between $\frac{pi}{2}$ and 0 [rad]. This will let freedom to the last panel. At the end of the rotation, the four RB of the mechanical arms will be aligned with the horizontal axis.

The kinematic rotation joints have only one degree of freedom (dof) (classical hinges), blocking all the others dofs. These joints are therefore assimilated to simple hinges and are therefore not really represented on the SolidWorks model. The edges that are common between the different RB are used to represent these hinges, as can be seen in Fig. 6.4.

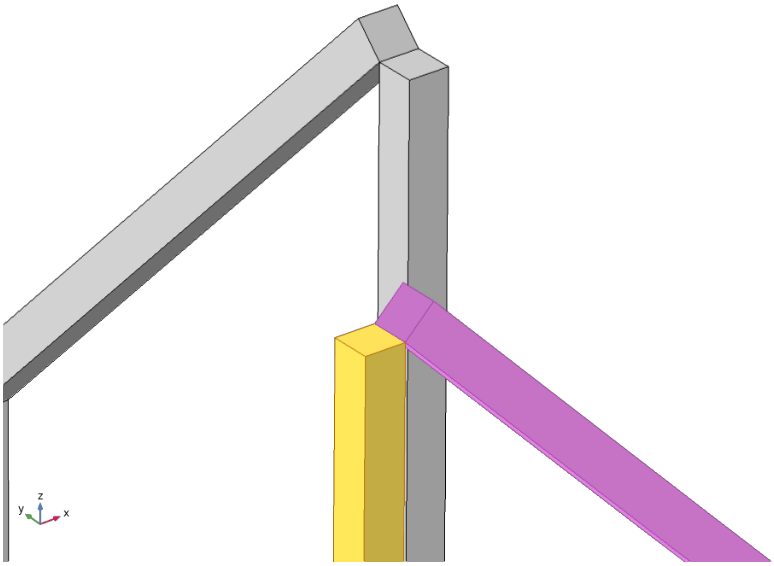

Figure 6.4: Hinges are represented by the common edge between two rigid bodies depicted in pink and yellow.

The model of the mechanical arms considered is therefore the one shown in Fig. 6.5. This figure shows the initial positions of RB 1, 2, 3 and 4 for the four different mechanical arms. The objective is to deploy them so that they end up in the disposition studied in chapter 4. The angles of rotation around the hinges therefore need to be set for the simulation. To do this, all that needs to be done is to enter into the **COMSOL Multiphysics** software the angle of rotation β_i required to ensure that each element is rotated around the hinges in order to end back to the horizontal during the same period of time.

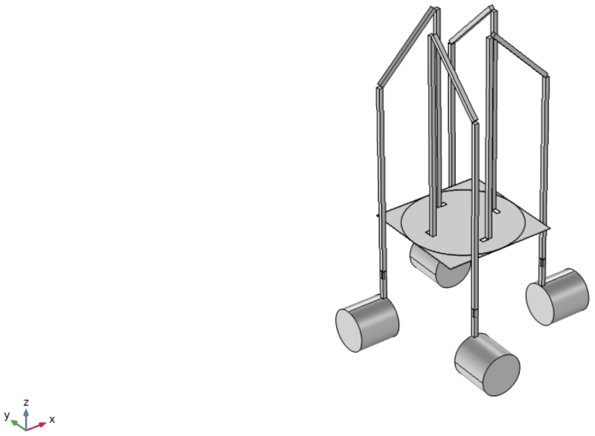

Figure 6.5: Model of the four mechanical arms.

This time lapse does not have much influence on the results, as they are mainly dependent on the time through the time step. As the structure is complex, a time step that is too high adds a huge amount of computing time to the software. This is why an arbitrary time of 10 seconds for the total deployment is chosen with a time step of 0.1 second in order to avoid having a simulation time that is too long for results which are not any more accurate. The time of 10 seconds for deployment is totally disillusioning but does not change the results of the dynamic analysis at deployment level. Indeed, taking 10 seconds or 10 hours with a proportional time step would give the same results with a different time scale.

In **COMSOL Multiphysics**, it is therefore necessary to insert the angles angles β in order to end up in a deployed state where all the RB are horizontal and lie in the (**x**, **y**) plane. For RB 1 of the arms, the angle to be made is $\beta_1 = \frac{\pi}{2}$ [rad] around rotational joint A with respect to the square base (horizontal plane). This angle is then simply multiplied by the time step so that the speed of rotation of RB 1 respects the speed of rotation of the other bodies. RB 2 must make an angle of $\beta_2 = -\frac{3\pi}{4}$ [rad] around rotational joint B with respect to RB 1 and RB 3 must make an angle of $\beta_3 = -\frac{\pi}{4}$ [rad] around rotational joint C with respect to RB 2. RB is not really useful when considering only the mechanical arms, thus fixed joints have been applied on them to fix them on RB 3. As all these angles are multiplied by the time step, the rotational speeds of the different RB will adapt so that at the tenth second, they are all perfectly aligned with the horizontal. It is to note that the β-angles just cited are corresponding to one mechanical arm. The sign of these angles and the axis around which they rotate change for the four mechanical arms.

6.1.2. Analysis

Fig. 6.6, 6.7, 6.8 and 6.9 show the deployment of these four mechanical arms in several stages, respectively for the following time steps: $t = 0$, 3.2, 6.4 and 10 [s].

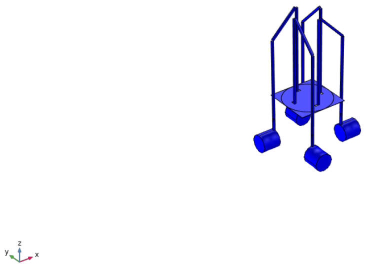

Figure 6.6: Folded state: time $t = 0$ [s].

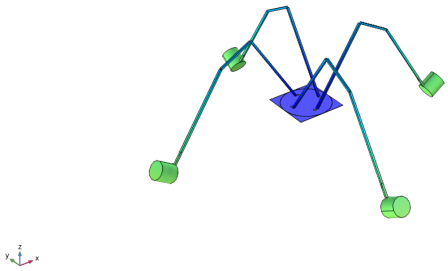

Figure 6.7: Deploying state: time $t = 3.2$ [s].

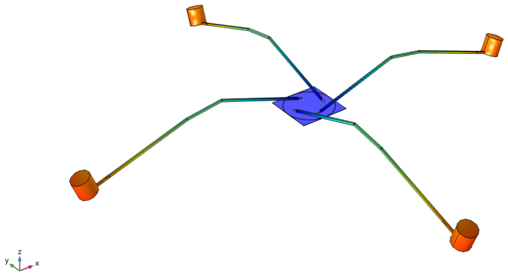

Figure 6.8: Deploying state: time $t = 6.4$ [s].

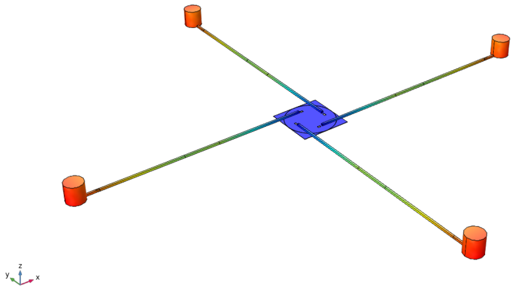

Figure 6.9: Deployed state: time $t = 10$ [s].

The first thing that emerges from these figures is that the deployment of these mechanical arms is collision-free, which was the first point to check. As the role of these mechanical arms is to guide the telescopes, one could check the motion of each of the four telescopes. However, the telescope does not simply follow a straight trajectory towards the outside of the structure, but also rotates around the centre of the structure (spiral behaviour). This rotation takes place over an angle of $\frac{5\pi}{4}$ [rad]. The four mechanical arms are therefore placed on a rotating platform, which also rotates on itself by a angle of approximately $\frac{5\pi}{4}$ [rad] over the same 10-second period. It is not exactly $\frac{5\pi}{4}$ [rad] since the mechanical arms are not centred on the square base.

Fig. 6.10, 6.11, 6.12 and 6.13 finally show the deployment of the four mechanical arms guiding the telescopes and rotating $\frac{5\pi}{4}$ [rad] around the centre of the structure along the $\mathbf{z}$ axis.

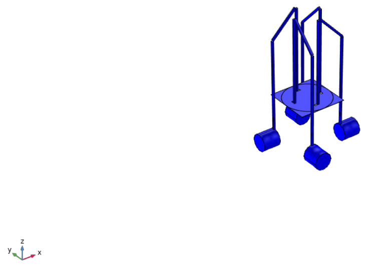

Figure 6.10: Folded state: time $t = 0$ [s].

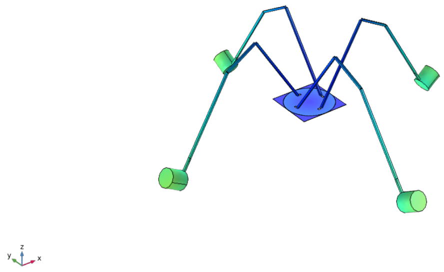

Figure 6.11: Deploying state: time $t = 3.2$ [s].

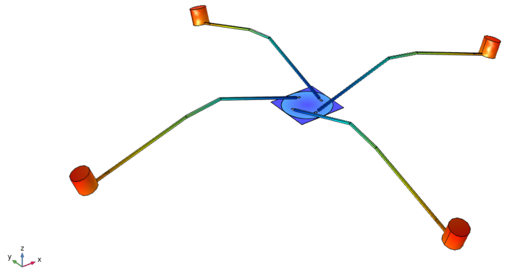

Figure 6.12: Deploying state: time $t = 6.4$ [s].

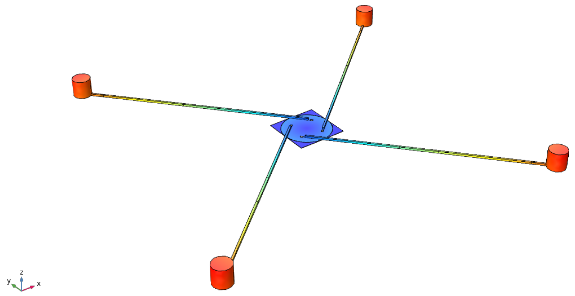

Figure 6.13: Deployed state: time $t = 10$ [s].

Fig. 6.17 shows the trajectory of the centre point of one of the bottom surface of one of the four telescopes that will be in contact with the last panel of each spiral arm. The displacement of this point is shown in Fig. 6.14, 6.15 and 6.16. This trajectory gives an idea of what will be needed to impose as displacements for the spiral arms since the telescopes will always be in contact with the last panels of each spiral arms.

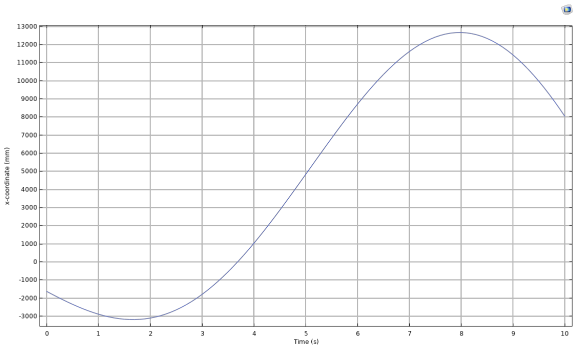

Figure 6.14: Evolution of the x-coordinates of the considered point as a function of the time.

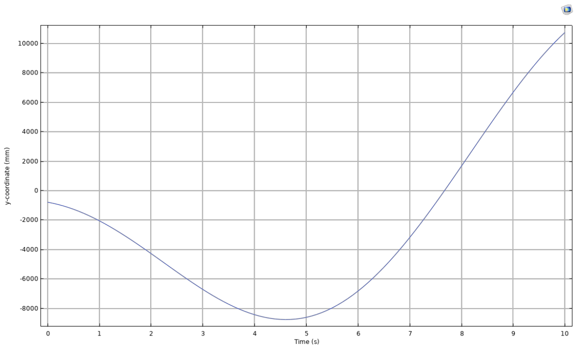

Figure 6.15: Evolution of the y-coordinates of the considered point as a function of the time.

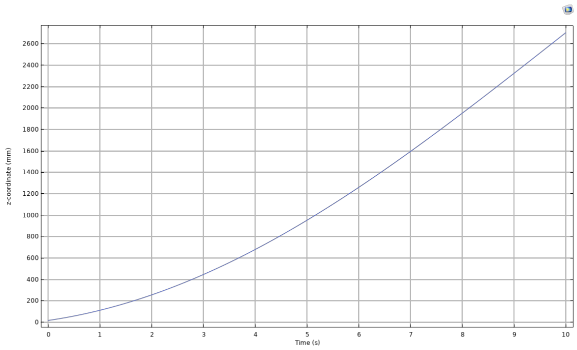

Figure 6.16: Evolution of the z-coordinates of the considered point as a function of the time.

Figure 6.17: Displacement of the centre of the bottom surface of one telescope during the deployment phase (t = 0 : 0.01 : 10 [s]).

Before starting to analyse the second mechanism, i.e. the square origami flasher, one can say that the alignment of one mechanical arm w.r.t. the last panel of the spiral arm will also change during the deployment. The telescopes, that will be fixed to the mechanical arms, will thus need to be able to rotate within a cylindrical joint between them and the last panels of the four spiral arms. Otherwise, the motion would not be possible due to a lack in free degrees of freedom of the last panels.

6.2. Final square origami flasher

The square origami flasher follows a precise pattern that can be extended ad infinitum. In the scope of this research, an origami flasher with 60 panels has studied. It is shown in Fig. 6.18.

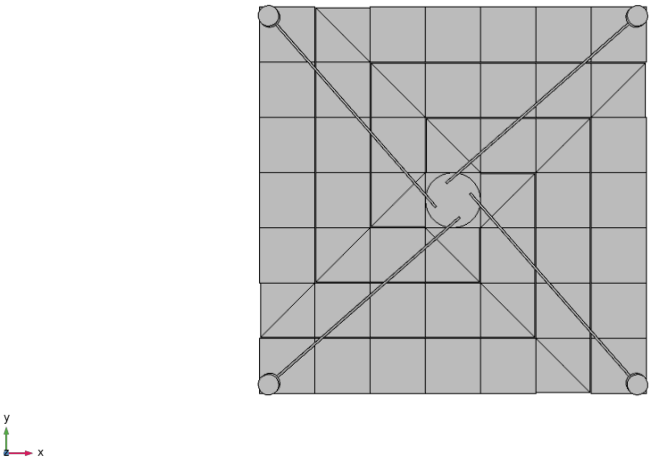

Figure 6.18: Square origami flasher pattern.

These sixty panels form four spiral arms like those shown in Fig. 4.11. These four spiral arms will therefore be made up of fifteen panels, each of which can be folded one on top of the other using simple hinges. As with the mechanical arms, the simple hinges are depicted by the common sides between the different bodies. The four spiral arms are independent of each other, but could be linked for example with elastic joints between the different spiral arms. These joints could have a certain potential energy (memory shape) that could help the deployment [70].

6.2.1. Conception

The first step is to model a single spiral arm in order to determine the relative angles of rotation that need to be added as a rotational constraint to each hinge between the panels making up this spiral arm. As these four arms are symmetrical, it is sufficient to apply the same angles to the other three spiral arms. Fig. 6.19 represents the single spiral arm in its folded state. It comes directly that each panel starts in a vertical position w.r.t. the square base and ends in a horizontal position. As a consequence, the relative angles between each pair of consecutive panels is always π [rad] except for the very first panel linked to the square base which has to perform a rotation of $\frac{\pi}{2}$ [rad] around the hinge between square base and itself.

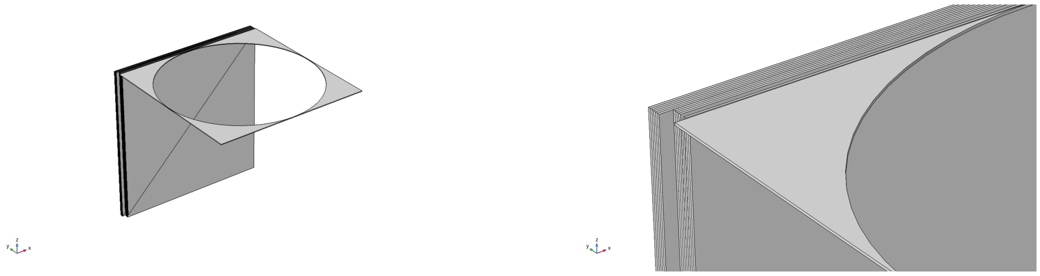

(a) Overall model of the spiral arm.

(b) Zoom on the different folded panels composing the spiral arm.

Figure 6.19: Single spiral arm linked to the square base in the folded state of the structure. These schemes have been realised with the software **COMSOL Multiphysics**.

Fig. 6.20, 6.21, 6.22 and 6.23 show the deployment of a single spiral arm in a period time of 10 seconds. It can be seen that from a very compact state, it is possible to obtain a very large surface after deployment. Moreover, no physical collision between the different panels is observed.

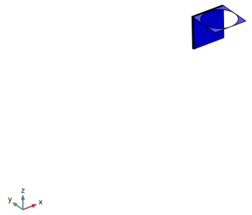

Figure 6.20: Folded state: time $t = 0$ [s].

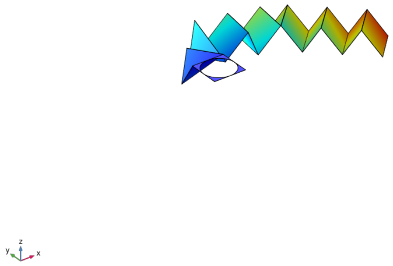

Figure 6.21: Deploying state: time $t = 3.2$ [s].

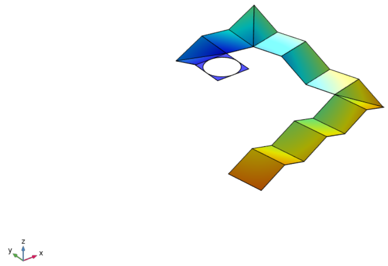

Figure 6.22: Deploying state: time $t = 6.4$ [s].

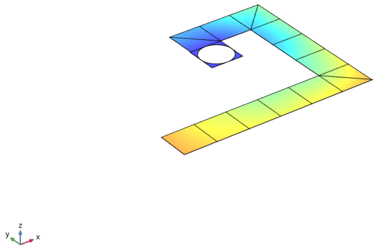

Figure 6.23: Deployed state: time $t = 10$ [s].

These figures prove that a deployment is possible for this single spiral arm, what need to be add is then a similar trajectory that the one of the point shown in Fig. 6.17 to the last panel in order to ensure the two mechanisms can work together as a single one. By applying cylindrical joints between the telescopes and the last panels and only imposing a motion to the mechanical arms, these last panels (and thus the spiral arms) can follow the deployment of the mechanical arms. It can be useful to implement in the future a system (with cables) to guide the spiral in their deployment when activated by the mechanical arms. Indeed, to allow collision-free deployment, the hinges between each panels composing a spiral arms are constraints; they can not rotate at infinity and once at their aligned position with the previous panel, they can not rotate anymore. This is done by imposing a locking option where the maximum and minimum rotational angles regarding the relative axis need to be set.

6.2.2. Analysis

The four arms in their folded state are added around the same square base than the one use for the others parts of the system. Since the mechanical arms are not yet added to the final system, the same methodology has been made than for the single spiral arm deployment. Fig. 6.24, 6.25, 6.26 and 6.27 show the deployment of the four spiral arms and confirm that there is a way to deploy this structure without any collisions.

Figure 6.24: Folded state: time $t = 0$ [s].

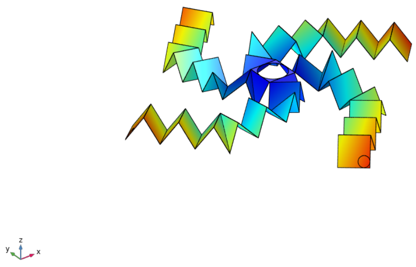

Figure 6.25: Deploying state: time $t = 3.2$ [s].

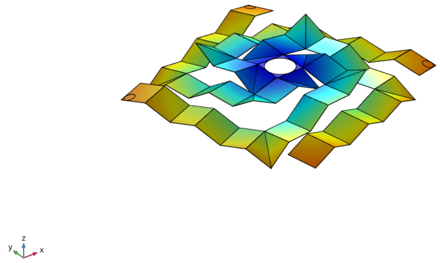

Figure 6.26: Deploying state: time $t = 6.4$[s].

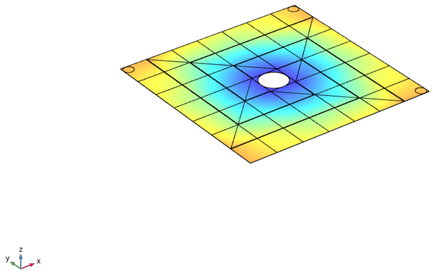

Figure 6.27: Deployed state: time $t = 10$ [s].

6.3. Complete system

Since the mechanical arms are driving the deployment, the last panels which are directly linked to the telescopes throughout a free cylindrical joint can follow the deployment. However, since the hinges in the spiral arms are not perfectly designed yet, locking constraints have been applied on all of them in order to allow them to fold and unfold freely only in the right direction. This will permit a collision-free deployment of the system.

6.3.1. Final deployment

Fig. 6.28, 6.29, 6.30 and 6.31 represent four stages of the deployment in chronological order. It is important the link these figures with the proof of the concept picture given in Fig. 4.12a, 4.12a, 4.12a and 4.12c (chapter 4) where a strong resemblance is immediately apparent.

Figure 6.28: Folded state: time $t = 0$ [s].

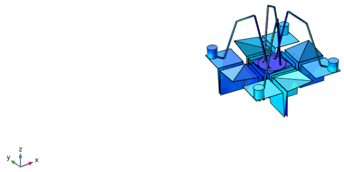

Figure 6.29: Deploying state: time $t = 3.2$ [s].

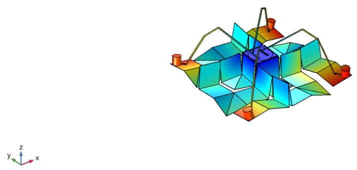

Figure 6.30: Deploying state: time $t = 6.4$ [s].

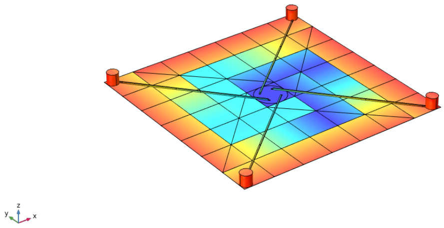

Figure 6.31: Deployed state: time $t = 10$ [s].

6.3.2. Discussion

Fig. 6.28, 6.29, 6.30 and 6.31 show the full deployment of the structure studied as part of this research, with the dimensions required to withstand a static load which represents the acceleration undergone by the satellite in the Lagrange 2 orbit determined in Chapter 4. The deployment is collision-free and therefore physically feasible for this simplified model.

Since the model is highly simplified and does not include all the components actually required for a satellite to carry out such a mission (payload, sunshield, physical hinge, compensators, more detailed optical instruments, etc.), there remains a significant amount of research ahead to achieve a final design with all the features and details. At this stage, this initial simulation looks promising and provides an excellent first approximation for, potentially, future studies on this structure.

7
Future Works

This thesis provides a preliminary design for a deployable structure designed to meet specific criteria relating to nulling interferometry. Indeed, the requirements were to obtain a structure which, when fully deployed in the Lagrange 2 orbit and subjected to a certain static load representing exclusively the acceleration on this orbit, reduces as much as possible the misalignment between the different telescopes represented by δ_{max} (maximum 30 arcsec of misalignment) while decreasing the θ angular resolution, which is inversely proportional to the size of the b baseline and therefore on the size of the deployed structure, as much as possible in order to resolve finer details.

Starting from a blank page, many simplification assumptions had to be made in order to obtain the model and the results presented in chapters 4 and 6. The model studied in this research is a highly simplified one, which could serve as a basis for more in-depth studies on the subject. This chapter will present some of the next steps required to finalise a complete design for such a mission.

7.1. Material analysis

In this research, no requirements have been imposed in terms of budget, maximum weight, etc. However, if this model is really considered, a material analysis based on many more requirements needs to be carried out. Indeed, what led to the choice of CFRE for the panels and for the mechanical arms, for example, is the fact that these materials are common in space and show a good stiffness, high resistance to deformation and good thermal behaviour. Nevertheless, the choice of the material should be made after a deep study of all the other possibilities. There are especially a lot of development on going with super light and super resistant material that could be much better than the CFRE used in this thesis.

In the scenario where more detailed material analysis is carried out and other materials are selected, as the model used in this research is available, it will be sufficient to change the material in **COMSOL Multiphysics** and combine the **COMSOL Multiphysics** data with the **MatLab** codes provided in the App. A to obtain the new misalignment values.

7.2. Space environment consideration

To carry out the simulations presented in chapter 4, a certain static load was applied in a totally uniform configuration to the structure in its deployed state. The load taken into consideration in the model corresponds to the maximum gravitational force felt by the satellite when it is in the orbit of L2. Although the acceleration is maximum (closest alignment with all the celestial bodies), it remains very low because of the large distances separating the satellite from the celestial bodies around which it orbits (Earth, Sun and Moon).

In future research, it will also be necessary to consider other factors present in the space environment, such as potential collisions with debris or micro-meteorites, solar pressures (the satellite is not exactly on the L2 point in line with the Sun and the Earth, but revolves around it. As a result, solar pressures find their way to the satellite), propulsion loads (if the satellite uses a thruster to redirect itself momentarily, this will induce stresses on the structure), random vibrations (which can come from the thruster, for example), and so on [71].

7.3. Vibration and modal analysis

A study with the eigenmodes and eigenfrequencies could be made to check the optical instruments at the critical stages when the entire structure is subject to vibrations for example during the launch stage or during the deployment of the structure or during the use of the thruster.

7.4. Kinematic joints study

Arms: One of the main assumptions made in Chapter 6 was to consider the kinematic joints of the mechanical arms as being simple hinges and therefore not to model them in reality (they were represented by the junction of the edges of the different rigid bodies making up the mechanical arms). The objective was simply to see if the deployment could be carried out without collision of the various elements of the structure. A more detailed study of these hinges needs to be carried out in order to have more exact dimensions of the rigid bodies making up the mechanical arms. Many possibilities are possible for example using classical rigid hinges or more innovative polymer composites for bending actuators [72].

Between spiral arms: There are possibilities either to add between the spirals an elastomer designed to return some energy during the deployment (spring type) or to design the spiral in order that when deployed they fit all together to make a more rigid platform. This also could be evaluated in detail during the next stage of the design.

7.5. Lockable system

Another assumption made in chapter 4 was that the mechanical arms, once the structure completely deployed, were fixed to the panels composing the origami flasher part of the structure. This can be done by designing a lockable system that would connect the mechanical arms to the panels after deployment. Since the mechanical arms proved to be really useful to increase the resistance to deformation by assuming this connection, it could be interesting to design such a system.

7.6. Thermal analysis

The mission on which this thesis is based is supposed to operate in low temperature conditions, i.e. 40 Kelvin [6]. For the purposes of this research, temperature was not a consideration, although the CTE (coefficient of thermal expansion) of the various materials was specified. A thermal analysis is essential when designing a satellite for a space mission. This involves determining all the maximum sources of thermal energy, whether internal (engine or other) or external (solar radiation, albedo, etc.) to the structure, and then analysing the temperatures observed on the structure (still considering the orbital conditions used for all this research). Depending on the results, and with a view to obtaining a temperature of 40 K, an active or passive thermal protection system should be considered. This could be a complex sunshield system such as that used on the JWST [35], or simply a special paint [71] if the temperatures obtained are moderate.

7.7. Payload consideration

The model used in this research consists of just a few components:

- The structural part composed of panels, kinematic joints, mechanical arms and a rotating platform.
- The telescopes, modelled simply as high-density optical glass cylinders to simulate heavy loads representative of optical instruments.

Initially, this model enables the reaction of a system subjected to a uniformly distributed load to be roughly observed. The model is therefore totally symmetrical and the deformations are the same for each telescope. In reality, all the instruments on the structure necessary for the mission must be considered. The simulations must therefore take into account the different mass distribution due to the many instruments being placed in a way that is not necessarily symmetrical.

A more complete design considering all the instruments necessary for such a mission must be carried out. Smart elements can also be studied with the aim of further reinforcing the stability of the structure, for example.

7.8. Discussion

Such a project requires a considerable amount of resources (people, time, finance) with a team having broad and interdisciplinary knowledge. It is a huge project.

Every aspects being interconnected, any new detail or result could affect a choice previously made or a dimensioning calculated. So, it will be crucial to tackle the project for the design of the structure with a good teamwork and to share and communicate continuously about the results of each one in the team in order to manage properly the project and then to reach a perfect final solution.

8

Conclusion

The research topic concerns the design of a structure as part of a nulling interferometry project in space to study and learn about the exoplanets.

The design of the structure has to take into account both the constraints of limited space for transporting the structure in the Ariane 6 launcher and the need for maximum measurement accuracy.

In order to optimise the accuracy of the measurements, it was therefore necessary to to maximise the length of the baseline and at the same time to minimise the deformation of the structure, i.e. to ensure sufficient rigidity of the structure despite maximising its size.

A design with a clever, deployable structure could be a good solution to all these requirements and constraints. requirements and constraints associated with the problem.

The problem can therefore be defined as a preliminary study of a suitable design for a deployable structure such as this:

- The folded structure is adapted to the dimensions of the launcher.
- Once unfolded, the length of the base line is maximised.
- The unfolded structure has sufficient rigidity to minimise telescope misalignment.

The question raised at the start of this thesis was therefore the following:

What could be a deployable spatial nulling interferometer design that meets the requirements, i.e. $b \geq 15$ m and $\delta_{\text{max}} \leq 30$ arcsec?

The aim of this year-long project was to come up with a design that met these requirements as well as possible.

As a result of the literature review in chapter 3 and the design ideas cited in chapter 4, a 3D model was produced to be tested in more detail. Figs. 8.1 and 8.2 show the folded and unfolded states of the system studied, respectively.

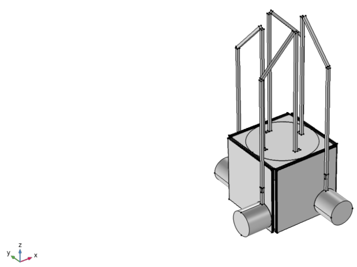

Figure 8.1: 3D of the folded state system at $t = 0$ [s].

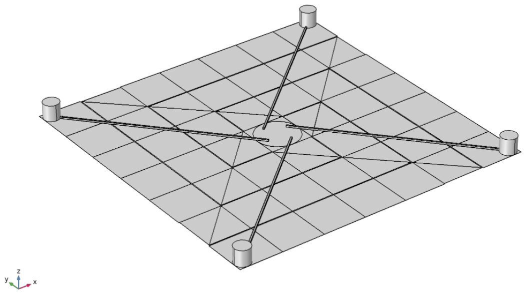

Figure 8.2: 3D of the deployed state system at $t = t_f$ [s].

In chapter 5, from the static analysis based on a 3D finite element model for material strength and deformation calculations, it was possible to check that the proposed design would meet the requirements and the preliminary dimensions of the structure were defined.

The materials making up the origami panels and the mechanical arms were first obtained: carbon fibre reinforced epoxy. The dimensions of the fully deployed structure are shown in Tab.8.1.

b [m]	$\mathbf{L}_{\text{tot}}$ [m]	$\mathbf{l}_{\text{base}}$ [m]	$\mathbf{e}_{\text{pan}}$ [mm]	$\mathbf{h}_{\text{arm}}$ [mm]	$\mathbf{w}_{\text{arm}}$ [mm]	$\mathbf{e}_{\text{arm}}$ [mm]
26.73	18.90	2.70	10	100	100	10

Table 8.1: Optimal dimensions of the model considered.

With a baseline of 26.73 m for the model studied, the baseline requirement is largely respected ($b \geq 15$ m maximum). The angular resolution θ corresponding to the wavelength range for MIR observation λ $[3,\ 20]$ $[\mu m]$, decreases thus from:

$$\theta = \frac{\lambda}{2b} \in [0.0206,\ 0.1375] \text{ [arcsec]}, \tag{8.1}$$

to the more precise values of angular resolution:

$$\theta = \frac{\lambda}{2b} \in [0.0116,\ 0.0772] \text{ [arcsec]}, \tag{8.2}$$

In addition, this model, when subjected to a uniformly distributed static load representing the gravitational acceleration in $\left[\frac{\text{m}}{\text{s}^2}\right]$ experienced by a satellite in the orbit of the Lagrange 2 point, showed excellent resistance to deformation. The maximum misalignment requirement is largely met by having the misalignment of the telescopes for this optimised model $\delta_{\text{max}} = 1.0033$ [arcsec], which is well below the 30 arcsec initially requested.

In chapter 6, a 3D model using **COMSOL Multiphysics** was used for a kinematic study of the deployment of the structure and showed collision free deployment from the folded to the unfolded positions. Fig. 8.3, 8.4, 8.5 and 8.6 represent thus the four explicit stages of the deployment in chronological order.

Figure 8.3: Folded state: time $t = 0$ [s].

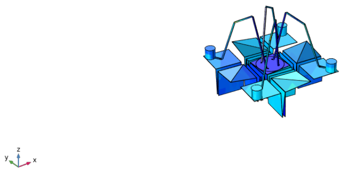

Figure 8.4: Deploying state: time $t = 3.2$ [s].

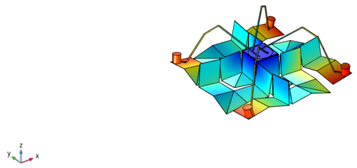

Figure 8.5: Deploying state: time $t = 6.4$ [s].

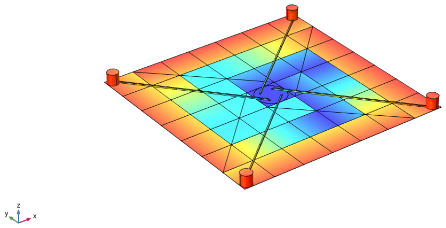

Figure 8.6: Deployed state: time $t = 10$ [s].

As this is a preliminary design phase, Chapter 7 summarised some of the additional issues to be addressed in the future. There are still many details, studies and optimisations that need to be done to achieve a final design of a deployable, high performance structure. Nevertheless, this research has opened a door for a new design that could suit very well the requirements of the space nulling interferometry technology in the future.

This research could therefore be seen as a promising first step in a long and exciting journey that may one day contribute to the mission of better understanding the universe and searching for life beyond our solar system.

References

[1] *An Ambitious Mission Employing a Formation-Fliying Nulling Interferometer in Space working at Mid-Infrared Wavelengths*. LIFE. May 3, 2023. url: `https://life-space-mission.com/mission/`.

[2] *James Webb Space Telescope*. NASA. Aug. 15, 2023. url: `https://www.nasa.gov/mission_pages/webb/main/index.html`.

[3] *Hubble Space Telescope*. NASA. Aug. 15, 2023. url: `https://www.nasa.gov/mission_pages/hubble/main/index.html`.

[4] Pascal Hallibert. “Technologies for future large optical missions: an ESA perspective”. In: *Space Telescopes and Instrumentation 2022: Optical, Infrared, and Millimeter Wave*. Vol. 12180. SPIE. 2022, pp. 20–43.

[5] *NULLING INTERFEROMETRY TECHNIQUES WITH SINGLE TELESCOPE - EXPRO+*. ESA. June 12, 2023. url: `https://esastar-publication-ext.sso.esa.int/ESATenderActions/details/42923`.

[6] J. Loicq. “Nulling Interferometry Techniques with Single Telescope”. In: (2022).

[7] Colin Dandumont et al. “Exoplanet detection yield of a space-based Bracewell interferometer from small to medium satellites”. In: *Journal of Astronomical Telescopes, Instruments, and Systems* 6.3 (2020), pp. 035004–035004.

[8] *How nulling interferometry works*. ESA. Aug. 15, 2023. url: `https://www.esa.int/ESA_Multimedia/Images/2002/03/How_nulling_interferometry_works`.

[9] D Defrère and J Loicq. *Space Optics - Chapter 4: Space Interferometry*. 2022.

[10] Luca Schifano et al. “Développement d’un interféromètre spatial pour la détection et la caractérisation d’exoplanètes”. In: (2018).

[11] *Ariane 6*. Arianespace. May 3, 2023. url: `https://www.arianespace.com/vehicle/ariane-6/`.

[12] M Sun, WJ Staszewski, RN Swamy, et al. “Smart sensing technologies for structural health monitoring of civil engineering structures”. In: *Advances in civil engineering* 2010 (2010).

[13] Kazuhiro Otsuka and Tomoyuki Kakeshita. “Science and technology of shape-memory alloys: new developments”. In: *mrs bulletin* 27.2 (2002), pp. 91–100.

[14] MJ Willis. “Proportional-integral-derivative control”. In: *Dept. of Chemical and Process Engineering University of Newcastle* 6 (1999).

[15] Hai Nguyen, Wael Zatar, and Hiroshi Mutsuyoshi. *Hybrid polymer composites for structural applications*. Elsevier, 2017, pp. 35–51.

[16] B Culshaw. “Smart structures—a concept or a reality?” In: *Proceedings of the Institution of Mechanical Engineers, Part I: Journal of Systems and Control Engineering* 206.1 (1992), pp. 1–8.

[17] Abeer Samy Yousef Mohamed. “Smart materials innovative technologies in architecture; towards innovative design paradigm”. In: *Energy Procedia* 115 (2017), pp. 139–154.

[18] Michelle Addington and Daniel Schodek. *Smart materials and technologies in architecture*. Routledge, 2012.

[19] Inderjit Chopra and Jayant Sirohi. *Smart structures theory*. Vol. 35. Cambridge University Press, 2013.

[20] V Shankar et al. “Design and Development of Instrumentation for Active Vibration Control of Smart Aerospace Structures”. In: (1999), pp. 430–436.

[21] Jian Sun et al. “Morphing aircraft based on smart materials and structures: A state-of-the-art review”. In: *Journal of Intelligent material systems and structures* 27.17 (2016), pp. 2289–2312.

[22] Amitabha Datta et al. “Damage detection in composite aircraft wing-like test-box using distributed fiber optic sensors”. In: *Optical Fiber Technology* 66 (2021), p. 102651.

[23] Ruven Spannagel et al. “Characterizing lightweight and dimensionally ultra stable structures for space applications”. In: (2013).

[24] Lee Feinberg et al. “Ultra-stable segmented telescope sensing and control architecture”. In: *UV/Optical/IR Space Telescopes and Instruments: Innovative Technologies and Concepts VIII*. Vol. 10398. SPIE. 2017, pp. 157–165.

[25] M Salvo et al. “Study of joining of carbon/carbon composites for ultra stable structures”. In: *Journal of the European Ceramic Society* 30.7 (2010), pp. 1751–1759.

[26] *Les matériaux composites*. MAE. Aug. 10, 2023. url: `https://perso.crans.org/epalle/M2/MHP/Composites_MAE_2015.pdf`.

[27] *La première mission spatiale d’imagerie d’exoplanètes sera lancée en 2027*. National Geographic. Aug. 10, 2023. url: `https://www.nationalgeographic.fr/espace/la-premiere-mission-spatiale-dimagerie-dexoplanetes-sera-lancee-en-2027`.

[28] *Nancy Grace Roman Space Telescope*. NASA. Aug. 10, 2023. url: `https://www.nasa.gov/content/goddard/nancy-grace-roman-space-telescope`.

[29] Laura E Coyle et al. “Large ultra-stable telescope system study”. In: 11115 (2019), pp. 196–208.

[30] *Gaia Spacecraft Overview*. NASA. May 9, 2023. url: `https://spaceflight101.com/gaia/gaia-spacecraft-overview/`.

[31] *L’origami*. Japan Experience. Aug. 10, 2023. url: `https://www.japan-experience.com/fr/preparer-voyage/savoir/comprendre-le-japon/origami-art-pliage-papier`.

[32] Andrea Enrico Del Grosso and Paolo Basso. “Adaptive building skin structures”. In: *Smart Materials and Structures* 19.12 (2010), p. 124011.

[33] Alexander E Marras et al. “Programmable motion of DNA origami mechanisms”. In: *Proceedings of the National Academy of Sciences* 112.3 (2015), pp. 713–718.

[34] *GAIA'S LAUNCH*. ESA. July 11, 2023. url: `https://www.cosmos.esa.int/web/gaia/news_20131206`.

[35] *The sunshield*. NASA. May 4, 2023. url: `https://webb.nasa.gov/content/observatory/sunshield.html`.

[36] *Webb and Ariane 5: a fit made perfect*. ESA. May 4, 2023. url: `https://www.esa.int/ESA_Multimedia/Images/2021/06/Webb_and_Ariane_5_a_fit_made_perfect`.

[37] Phanisri P Pratapa and Abhilash Bellamkonda. "Thick panel origami for load-bearing deployable structures". In: *Mechanics Research Communications* 124 (2022), p. 103937.

[38] Zirui Zhai, Yong Wang, and Hanqing Jiang. "Origami-inspired, on-demand deployable and collapsible mechanical metamaterials with tunable stiffness". In: *Proceedings of the National Academy of Sciences* 115.9 (2018), pp. 2032–2037.

[39] Shannon A Zirbel et al. "Accommodating thickness in origami-based deployable arrays". In: *Journal of Mechanical Design* 135.11 (2013), p. 111005.

[40] Nathan A Pehrson et al. "Self-deployable, self-stiffening, and retractable origami-based arrays for spacecraft". In: *AIAA Journal* 58.7 (2020), pp. 3221–3228.

[41] Nathan A Pehrson, Spencer P Magleby, and Larry L Howell. "An origami-based thickness-accommodating bistable mechanism in monolithic thick-sheet materials". In: (2018), pp. 1–7.

[42] Fulya Gürcü, Koray Korkmaz, and Gökhan Kiper. "Design of a reconfigurable deployable structure". In: (2014).

[43] Ke Bai et al. "Geometrically reconfigurable 3D mesostructures and electromagnetic devices through a rational bottom-up design strategy". In: *Science advances* 6.30 (2020), eabb7417.

[44] Ran Liu, Ruiming Li, and Yan-An Yao. "Reconfigurable deployable Bricard-like mechanism with angulated elements". In: *Mechanism and Machine Theory* 152 (2020), p. 103917.

[45] Longhai Zhao et al. "Sequentially assembled reconfigurable extended joints: self-lockable deployable structure". In: *Journal of Aerospace Engineering* 31.6 (2018), p. 04018103.

[46] Yong Zhang et al. "Design and characterization of multi-stable mechanical metastructures with level and tilted stable configurations". In: *Extreme Mechanics Letters* 34 (2020), p. 100593.

[47] Jingze Wang et al. "Designing multi-stable structures with enhanced designability and deformability by introducing transition elements". In: *Composite Structures* 233 (2020), p. 111580.

[48] A Litteken Douglas. "Inflatable technology: using flexible materials to make large structures". In: *Electroactive Polymer Actuators and Devices (EAPAD) XXI* 10966 (), p. 1096603.

[49] RE Freeland et al. "Large inflatable deployable antenna flight experiment results". In: *Acta Astronautica* 41.4-10 (1997), pp. 267–277.

[50] *Bracket — Structural Mechanics Tutorials*. COMSOL Multiphysics. Feb. 13, 2023. url: `https://www.comsol.com/model/bracket-8212-structural-mechanics-tutorials-10314`.

[51] *Double-Pendulum Dynamics*. May 3, 2023. url: `https://www.comsol.com/model/double-pendulum-dynamics-14021`.

[52] PM Liyanage and HMYC Mallikarachchi. “Origami based folding patterns for compact deployable structures”. In: (2013).

[53] Eric W Weisstein. “Logarithmic spiral”. In: *https://mathworld. wolfram. com/* (2002).

[54] Douglas Dunham. “Hyperbolic spirals and spiral patterns”. In: *Meeting Alhambra, ISAMA-BRIDGES Conference Proceedings*. 2003, pp. 521–528.

[55] Wl Lewickyj. *La spirale logarithmique et sa développante*. 2015.

[56] *Spirale d’Archimède*. mathcurves. Apr. 15, 2023. url: `https://mathcurve.com/courbes2d/archimede/archimede.shtml`.

[57] Daoud Berkani, Ali Chékima, and Jean-Pierre Adoul. *La Spirale Discrète*.

[58] Mike Ashby. “Material property data for engineering materials”. In: *Engineering Department and Granta Design* 27 (2016).

[59] Ph Lequeu, KP Smith, and A Daniélou. “Aluminum-copper-lithium alloy 2050 developed for medium to thick plate”. In: *Journal of materials engineering and performance* 19 (2010), pp. 841–847.

[60] *Aluminum 7050-T7451*. ASM. May 18, 2023. url: `https://asm.matweb.com/search/SpecificMaterial.asp?bassnum=ma7050t745`.

[61] *Titanium Ti-6Al-4V (Grade 5), Annealed*. ASM. Aug. 10, 2023. url: `https://asm.matweb.com/search/SpecificMaterial.asp?bassnum=MTP641`.

[62] Celestino Veiga, J Paulo Davim, and AJR Loureiro. “Properties and applications of titanium alloys: a brief review”. In: *Rev. Adv. Mater. Sci* 32.2 (2012), pp. 133–148.

[63] *Les points de Lagrange*. Astronomes. Aug. 10, 2023. url: `https://astronomes.com/histoire-astronomie/les-points-de-lagrange/#:~:text=Le%20point%20de%20Lagrange%20L2%20se%20trouve%20%C3%A9galement%20sur%20la,d'un%20corps%20plus%20%C3%A9loign%C3%A9.`.

[64] *What is a Lagrange Point?* NASA. Aug. 10, 2023. url: `https://solarsystem.nasa.gov/resources/754/what-is-a-lagrange-point/#:~:text=Lagrange%20points%20are%20positions%20in,object%20to%20move%20with%20them.`.

[65] Matthieu Simeoni Nathan Scheinmann, Matthieu Simeoni, and Anton Ivanov. “Détermination d’une orbite autour de L2 pour la mission CHEOPS”. In: (2012).

[66] *Properties of fused silica*. Heraeus. Aug. 10, 2023. url: `https://www.heraeus.com/en/hca/fused_silica_quartz_knowledge_base_1/properties_1/properties_hca.html#tabs-608478-6`.

[67] *Properties of various mirror substrate materials*. TOT. Aug. 10, 2023. url: `https://www.fpi-protostar.com/bgreer/properties.htm`.

[68] Jean-Michel Génevaux. “Théorie des poutres, résistance des matériaux”. In: (2012).

[69] *Résistance des matériaux*. eurocodes. July 18, 2023. url: `https://www.calculs-eurocodes.com/rdm`.

[70] Sébastien Morterolle. "Étude de structures légères déployables pour applications spatiales". PhD thesis. Université Montpellier II-Sciences et Techniques du Languedoc, 2011.

[71] D Grodent and J Loicq. *Space experiment development*. 2021.

[72] *New cost-effective and sustainable polyethylene based carbon fibres for volume market applications*. CORDIS. Aug. 15, 2023. url: `https://cordis.europa.eu/article/id/238597-better-performing-carbon-fibres-at-reduced-cost-to-profit-and-planet/fr`.

A

Appendix A

A.1. Spiral research

The **MatLab** code name is Spitype.m.

```
%% Different types of spiral
%
% Author : Sacha Iannello, s170875
% Context : Master thesis done at the TU-Delft 2022-2023
%
% Problem : Comparison of the different types of spiral to determine the
%           spiral used for a square origami flasher.
close all;
clear all;
%% Data
n_elements = 6; % Number of element composing the spiral
n_revolutions = 0.5; % Number of revolution in a spiral
theta = linspace(0, 2*pi*n_revolutions, n_elements); % Angles between elements

%% Code
% Logarithmic spiral
r_log = exp(0.2*theta);
x_log = r_log .* cos(theta);
y_log = r_log .* sin(theta);
% Archimed spiral
r_arch = 0.1 * theta;
x_arch = 7*r_arch .* cos(theta)+0.5;
y_arch = 7*r_arch .* sin(theta);
% Fibonacci spiral
r_fibonacci = sqrt(theta);
x_fibonacci = r_fibonacci .* cos(theta);
y_fibonacci = r_fibonacci .* sin(theta);
% Hyperbolic spiral
r_hyper = 10 ./ theta;
x_hyper = 0.2*r_hyper .* cos(theta)-1;
y_hyper = 0.2*r_hyper .* sin(theta);

%% Results
figure;
subplot(2,2,1);
```

```
plot(x_log, y_log);
title('Logarithmic Spiral');
xlabel('x-coordinates [m]');
ylabel('y-coordinates [m]');
xlim([-2 1]);
subplot(2,2,2);
plot(x_arch, y_arch);
title('Archimedean Spiral');
xlabel('x-coordinates [m]');
ylabel('y-coordinates [m]');
xlim([-2 1]);
subplot(2,2,3);
plot(x_fibonacci, y_fibonacci);
title('Fibonacci Spiral');
xlabel('x-coordinates [m]');
ylabel('y-coordinates [m]');
xlim([-2 1]);
subplot(2,2,4);
plot(x_hyper, y_hyper);
title('Hyperbolic Spiral');
xlabel('x-coordinates [m]');
ylabel('y-coordinates [m]');
xlim([-2 1]);
```

A.2. Acceleration on L2

The **MatLab** code name is acceleration.m.

```
%% Gravitational acceleration felt by the structure on L2
%
% Author : Sacha Iannello, s170875
% Context : Master thesis done at the TU-Delft 2022-2023
%
% Problem : In order to measure the deformation of the structure due to
%             external loads on the L2 Lagrange orbit, we need to calculate
%             the gravitational acceleration exerted on the structure.
%
% Inconnues :
%   1) a = gravitational acceleration [m/s^2]
%
% Assumptions :
%   1) We only consider the impact of the Sun's, Earth's and Moon's
%      attractions (not debris, solar pressure, etc.).
%   2) We consider that we are sufficiently far from the celestial bodies
%      for the calculated acceleration to be distributed uniformly over the
%      entire structure (we therefore consider a material point of a
%      certain mass).
%
% Purpose of this function :
% To determine the maximum acceleration undergone by the structure when the
% Earth is as close as possible to the Sun and when the Moon is aligned
% between the Earth and the satellite.
close all;
clear;
```

```
%% Data
% Masses
M_sun = 1.989 * 10^30; % [kg]
M_earth = 5.972 * 10^24;  % [kg]
M_moon = 7.342 * 10^22;   % [kg]
% Distances
D_earth_sat = 1.5 * 10^9;                    % [m]
D_earth_sun = 147 * 10^9;                    % [m] perihelia
D_moon_sat = D_earth_sat - 405696 * 10^3 ; % [m] Moon aligned between Earth and sat
% Universal gravitational constant
G = 6.674*10^(-11); % [N*m^2/kg^2]

%% Code
a = G * (M_sun/(D_earth_sun + D_earth_sat)^2 + M_earth/D_earth_sat^2 + M_moon/(D_moon_sat)^2); % [m/s^2]

%% Results
fprintf('L accélération maximale ressentie par le satellite est de %.4f [m/s^2]\n', a);
```

A.3. Misalignment for material selection

The **MatLab** code name is deformation_mat.m.

```
%% Misalignment for the different materials
%
% Author : Sacha Iannello, s170875
% Context : Master thesis done at the TU-Delft 2022-2023
%
% Problem : To check that the acceleration undergone by the satellite does
%           not adversely affect the data, we need to check that the
%           misalignment between the telescope normal after deformation and
%           the z axis does not exceed 30 arcsec.
close all;
clear
%% Data
n_pt = 1 : 1 : 12; % [-] nbr of arrows
Z = [0, 0, 1]; % z-axis coordinates

%% Code
%% CFRE
% Determination of the most deformed telescope
M_CE = [-10957.142354481983       -11002.803663454397       21790.999999999985       -0.009969454490456622    -0.009998746327487687    -0.08117104057737647
-11810.468372387952       -11077.505395557415       21790.99999999999        -0.009969458915263336    -0.009998734645486371    -0.09042034541997669
-11311.178526999369       -11776.817497279295       21790.99999999999        -0.009969522715133614    -0.009998745333889534    -0.09243401411194875];
% New positions of the 3 arrows corresponding to the most deformed
% telescope
New_pos_CE = zeros(3, 3);
```

```
for i = 1:size(M_CE, 1)
    pos_ini = M_CE(i, 1:3);
    disp = M_CE(i, 4:6);
    New_pos_CE(i, :) = pos_ini - disp;
end
% Normal to the surface after deformation determination
vec1_CE = New_pos_CE(2, :) - New_pos_CE(1, :);
vec2_CE = New_pos_CE(3, :) - New_pos_CE(1, :);
normal_CE = cross(vec1_CE, vec2_CE);
% Misalignment computation
produit_scalaire_CE = dot(normal_CE, Z);
magnitude_n_CE = norm(normal_CE);
angle_degre_CE = acosd(produit_scalaire_CE / magnitude_n_CE); % [°]
delta_max_CE = angle_degre_CE*60*60; % [arcsec]

%% Aluminium
% Determination of the most deformed telescope
M_AL = [-10957.142354481983       -11002.803663454397
   21790.999999999985       -0.022061388533200676    -0.02212304065404198
       -0.18126625881509884
-11810.468372387952       -11077.505395557415      21790.99999999999
          -0.022061393409347214    -0.022123023772035667
   -0.2017338786965231
-11311.178526999369       -11776.817497279295      21790.99999999999
          -0.02206146195393322     -0.022123037529716734
   -0.20618764661978825];
% New positions of the 3 arrows corresponding to the most deformed
% telescope
New_pos_AL = zeros(3, 3);
for i = 1:size(M_AL, 1)
    pos_ini = M_AL(i, 1:3);
    disp = M_AL(i, 4:6);
    New_pos_AL(i, :) = pos_ini - disp;
end
% Normal to the surface after deformation determination
vec1_AL = New_pos_AL(2, :) - New_pos_AL(1, :);
vec2_AL = New_pos_AL(3, :) - New_pos_AL(1, :);
normal_AL = cross(vec1_AL, vec2_AL);
% Misalignment computation
produit_scalaire_AL = dot(normal_AL, Z);
magnitude_n_AL = norm(normal_AL);
angle_degre_AL = acosd(produit_scalaire_AL / magnitude_n_AL); % [°]
delta_max_AL = angle_degre_AL*60*60; % [arcsec]

%% Titanium
% Determination of the most deformed telescope
M_TT = [-10957.142354481983       -11002.803663454397
   21790.999999999985       -0.01435437444700952     -0.014393558197790887
       -0.11922395201137047
-11810.468372387952       -11077.505395557415      21790.99999999999
          -0.014354378110069075    -0.014393554926798842
   -0.1325412342545216
-11311.178526999369       -11776.817497279295      21790.99999999999
          -0.014354435189121929    -0.014393560711469092
   -0.1354384809854681];
% New positions of the 3 arrows corresponding to the most deformed
```

```
% telescope
New_pos_TT = zeros(3, 3);
for i = 1:size(M_TT, 1)
    pos_ini = M_TT(i, 1:3);
    disp = M_TT(i, 4:6);
    New_pos_TT(i, :) = pos_ini - disp;
end
% Normal to the surface after deformation determination
vec1_TT = New_pos_TT(2, :) - New_pos_TT(1, :);
vec2_TT = New_pos_TT(3, :) - New_pos_TT(1, :);
normal_TT = cross(vec1_TT, vec2_TT);
% Misalignment computation
produit_scalaire_TT = dot(normal_TT, Z);
magnitude_n_TT = norm(normal_TT);
angle_degre_TT = acosd(produit_scalaire_TT / magnitude_n_TT); % [°]
delta_max_TT = angle_degre_TT*60*60; % [arcsec]

%% Silicone Carbide E = 450GPa, mu = 0.14 and rho = 3210kg/m^3
% Determination of the most deformed telescope
M_SIC = [-10957.142354481983       -11002.803663454397
   21790.999999999985       -0.003033727410002383    -0.003043161544228383
       -0.02495984429155541
-11810.468372387952       -11077.505395557415      21790.99999999999
          -0.003033731607724784    -0.0030431515094919426
   -0.02777441188362104
-11311.178526999369       -11776.817497279295      21790.99999999999
          -0.0030337918450727614   -0.0030431611058113653
   -0.02838756890879515];
% New positions of the 3 arrows corresponding to the most deformed
% telescope
New_pos_SIC = zeros(3, 3);
for i = 1:size(M_SIC, 1)
    pos_ini = M_SIC(i, 1:3);
    disp = M_SIC(i, 4:6);
    New_pos_SIC(i, :) = pos_ini - disp;
end
% Normal to the surface after deformation determination
vec1_SIC = New_pos_SIC(2, :) - New_pos_SIC(1, :);
vec2_SIC = New_pos_SIC(3, :) - New_pos_SIC(1, :);
normal_SIC = cross(vec1_SIC, vec2_SIC);
% Misalignment computation
produit_scalaire_SIC = dot(normal_SIC, Z);
magnitude_n_SIC = norm(normal_SIC);
angle_degre_SIC = acosd(produit_scalaire_SIC / magnitude_n_SIC); % [°]
delta_max_SIC = angle_degre_SIC*60*60; % [arcsec]

%% Results
fprintf('<strong> MAX MISALIGNMENT </strong> \n\n')
fprintf('|------------------------------------------|\n')
fprintf('|   Material      |    Max misalignment    |\n')
fprintf('|------------------------------------------|\n')
fprintf('|Carbon epoxy     |       %.2f arcsec      |\n', 2*delta_max_CE)
fprintf('|Aluminium        |       %.2f arcsec     |\n', 2*delta_max_AL)
fprintf('|Titanium         |       %.2f arcsec      |\n', 2*delta_max_TT)
fprintf('|SiC              |       %.2f arcsec      |\n', 2*delta_max_SIC)
fprintf('|------------------------------------------|\n\n')
```

A.4. Evolution of the dimensions

The **MatLab** code name is dim_evo.m.

```
%% Dimensions of the structure for different thicknesses
%
% Author : Sacha Iannello, s170875
% Context : Master thesis done at the TU-Delft 2022-2023
%
% Problème : We want L_tot, l_base as a function of the thickness e_pan
close all;
clear;
%% Data
e = 0.001:0.001:0.05; % [m] Homogeneous panel's thicknesses
L_tot_folded = 5; % [m] Total length of the structure once folded
l_tel = 1; % [m] Telescopes height
% Initialisation
l_base = zeros(1, length(e)); % [m] length of one side of the square base
L_tot = zeros(1, length(e)); % [m] Total length of the structure once deployed

%% Code
for i = 1 : length(e)
    l_base(i) = L_tot_folded - 2*l_tel - 30*e(i); % [m] length of one side of the square base
    L_tot(i) = 7*l_base(i); % [m] Total length of the structure once deployed
    if sqrt(2)*L_tot(i) < 15
        break;
    end
end

%% Results
fprintf('<strong> MAIN DIMENSIONS </strong> \n\n')
fprintf('|------------------------------------|\n')
fprintf('|   L_tot   |     l_base     | e_pan |\n')
fprintf('|------------------------------------|\n')
for i = 1 : length(e)
    fprintf('|%.2f m    |     %.2f m     | %.f mm |\n', L_tot(i), l_base(i), i)
end
fprintf('|------------------------------------|\n')
```

A.5. Evolution of the misalignment

The **MatLab** code name is iterative.m.

```
%% Iterative thickness determination
%
% Author : Sacha Iannello, s170875
% Context : Master thesis done at the TU-Delft 2022-2023
%
% Problème : In order to minimise misalignment, the thickness of the
%            homogeneous panel will be increased by 1mm at each iteration
%            in order to stiffen the structure. The aim is always to find
%            the dimensions that will give a maximum misalignment of 30
%            arcsec while being as large as possible.
```

```
close all;
clear;
%% Data
% misalgnement vector
misalign_it = [5.82 3.06388187 2.11635029 1.58924266 1.30122687 1.13343218
     0.98400817 0.85875770 0.81179894 0.74401079 0.63447017 0.60220310
    0.54626869 0.49932280 0.46867890 0.39652822 0.34352728 0.29913422
    0.24588681];
% thickness
t = [1 2 3 4 5 6 7 8 9 10 12 14 16 18 20 25 30 40 50]; % [mm]

%% Results
% Total convergence:
figure
plot(t, misalign_it, 'o-', 'LineWidth', 1.1);
hold on
red_indices = 10;
plot(t(red_indices), misalign_it(red_indices), 'ro', 'MarkerFaceColor', 'r
    ', 'MarkerSize', 6);
xlabel('Thickness [mm]', 'FontSize', 12);
ylabel('Misalignment [arcsec]', 'FontSize', 12);
grid on;
set(gcf, 'Color', 'w');
set(gca, 'FontSize', 10);
xlim([1, 50]);
ylim([0, 6]);
% Zoom
figure
plot(t, misalign_it, 'o-', 'LineWidth', 1.1);
hold on;
plot(t(red_indices), misalign_it(red_indices), 'ro', 'MarkerFaceColor', 'r
    ', 'MarkerSize', 6);
xlabel('Thickness [mm]', 'FontSize', 12);
ylabel('Misalignment [arcsec]', 'FontSize', 12);
grid on;
set(gcf, 'Color', 'w');
set(gca, 'FontSize', 10);
xlim([10, 50]);
ylim([0, 2]);
```

A.6. Misalignment for the more realistic case

The **MatLab** code name is real_misalignment.m.

```
%% Misalignment
%
% Author : Sacha Iannello, s170875
% Context : Master thesis done at the TU-Delft 2022-2023
%
% Problème : L_tot, l_base and e_pan are now determined. The aim is to
%            determine the maximum misalignment corresponding more
    precisely.
%
close all;
clear;
%% Data
```

```
n_pt = 1 : 1 : 12;
Z = [0, 0, 1];

%% Code
% L_tot = 18.90m, l_base = 2.70m, e_pan = 10mm
M_tot_1 = [-9082.078109773569         -9535.324425749608
    3709.9999999999955        -0.0014596329152652963    -0.00194619693595254
        -0.021010401481224784
-8736.586606961042         -9059.79616760203         3709.9999999999955
          -0.0014592683737742133    -0.0019464576504464556
    -0.019581247736851992
-9641.095104148513         -8765.903541455791        3709.9999999999955
          -0.0014590503633985044    -0.0019457682962993577
    -0.02034904918888937];
% New positions
New_pos_1 = zeros(3, 3);
for i = 1:size(M_tot_1, 1)
    pos_ini = M_tot_1(i, 1:3);
    disp = M_tot_1(i, 4:6);
    New_pos_1(i, :) = pos_ini - disp;
end
% Normal determination
vec1_1 = New_pos_1(2, :) - New_pos_1(1, :);
vec2_1 = New_pos_1(3, :) - New_pos_1(1, :);
normal_1 = cross(vec1_1, vec2_1);
% Misalignment computation
produit_scalaire_1 = dot(normal_1, Z);
magnitude_n_1 = norm(normal_1);
angle_degre_1 = acosd(produit_scalaire_1 / magnitude_n_1); % [°]
delta_max_1 = 2*angle_degre_1*60*60; % [arcsec]

%% Results
fprintf('<strong> GROUPS MISALIGNMENTS </strong> \n\n')
fprintf('|------------------------|\n')
fprintf('|    Max misalignment    |\n')
fprintf('|------------------------|\n')
fprintf('|      %.4f arcsec     |\n', delta_max_1)
fprintf('|------------------------|\n')
```

A.7. Evolution of section dimensions for mechanical arms

The **MatLab** code name is dim_evo_arm.m .

```
%% Iterative section dimensions
%
% Author : Sacha Iannello, s170875
% Context : Master thesis done at the TU-Delft 2022-2023
%
% Problem : In order to reduce the offset as much as possible, the
%           cross-section of the mechanical arms will be incremented
%           according to h or w at each iteration in order to stiffen the
%           structure. The aim is always to find the dimensions that will
%           give a maximum misalignment of 30 arcsec while being as large
%           as possible.
close all;
clear;
```

```
%% Data
pair = 1 : 1 : 3; % [-]
h_1_max = 1047.52; % [mm] max value for the height of the section
w_1_max = 998; % [mm] max value for the width of the section

%% Code
% 1) Evolution of h w.r.t. w
% Group1
h_1 = 0 : h_1_max/7 : h_1_max; % [mm]
w_1 = [w_1_max 981.35 930.76 844.21 717.83 544.93 313.53 0]; % [mm]

%% Results
% 1) Evolution of h w.r.t. w
figure
plot(h_1, w_1, 'o-', 'LineWidth', 1.1);
xlabel('w [mm]', 'FontSize', 12);
ylabel('h [mm]', 'FontSize', 12);
grid on;
set(gcf, 'Color', 'w');
set(gca, 'FontSize', 10);
hold off;
```